WASHINGTON UNIVERSITY IN ST. LOUIS

Department of Physics

Dissertation Examination Committee:
Lee Sobotka, Chair
Mark Alford
Robert Charity
Wim Dickhoff
Martin Israel
Demetrios Sarantites

ASYMMETRY DEPENDENCE OF CORRELATIONS IN EXOTIC NUCLEI

by

Rebecca Sue Shane

A dissertation presented to the
Graduate School of Arts and Sciences
of Washington University in
partial fulfillment of the
requirements for the degree
of Doctor of Philosophy

May 2011

Saint Louis, Missouri

ABSTRACT OF THE DISSERTATION

Asymmetry dependence of correlations in exotic nuclei

by

Rebecca Shane

Doctor of Philosophy in Physics

Washington University in St. Louis, 2011

Professor Lee Sobotka, Chairperson

This work will discuss two experiments which seek to elucidate the asymmetry dependence of correlations in exotic nuclei. In the first experiment, a digital-signal-processing technique was developed to measure the neutron total cross section of the rare (but stable) isotope ^{48}Ca using a sample that is an order of magnitude smaller than would be required for the conventional technique. The isotopic and energy dependence of neutron total cross sections (e.g. the difference in neutron total cross section between symmetric ^{40}Ca and neutron-rich ^{48}Ca, as a function of energy) is sensitive to the asymmetry dependence of the surface imaginary potential in an optical-model analysis. Exploiting this sensitivity in a Dispersive Optical Model (DOM) allows one to study spectroscopic strength as a function of asymmetry. In the second experiment, the cross sections for hadron-induced single-nucleon knockout from ^{36}Ca were measured. The reduction in spectroscopic strength relative to standard shell-model calculations was obtained for the valence neutron and proton

orbitals in ^{36}Ca, by comparison of the experimental cross sections to theoretical cross sections calculated in an eikonal reaction theory. These values were compared to systematics based on previous knockout studies on nuclei with similar N/Z ratios, as well as to predictions for this nucleus based on DOM fits to data including the above-mentioned neutron total cross sections for calcium isotopes. A discrepancy between the trends in spectroscopic strength deduced from these two methods was confirmed - the trend extracted from knockout experiments is much stronger than that suggested by the present state-of-the-art DOM analysis.

Acknowledgements

The aid of Matt Devlin, Nik Fotiades, and John O'Donnell during the neutron total cross section measurement at the Los Alamos Neutron Science Center (LANSCE) is greatly appreciated. Additionally, I would like to thank the National Superconducting Cyclotron Laboratory (NSCL) for the loan of the ^{48}Ca sample, and John Yurkon for help preparing the target.

The knockout experiment could not have been undertaken without the assistance of Alexandra Gade and Dirk Wiesshaar at the NSCL. I also thank B. A. Brown for his shell-model calculations, J. A. Tostevin for the use of his knockout-reaction code, and Angela Bonaccorso and Alexandre Obertelli for additional cross-section calculations.

Many thanks as well to Bob Charity, with whom I have had many fruitful discussions. Finally, I am very grateful for the guidance and encouragement of my advisor Lee Sobotka.

This work was supported by the U.S. Department of Energy, Division of Nuclear Physics under Grant No. DE-FG02-87ER-40316 and has benefited from the use of LANSCE (operated by Los Alamos National Security LLC under DOE Contract No. DE-AC52-06NA25396) and the NSCL (under NSF Grant No. Phy-06007).

Contents

List of Figures

List of Tables

Chapter 1

Introduction

1.1 Studying exotic nuclei

The chart of nuclides (shown in Figure 1.1) is a map of all nuclei, plotted according to the number of protons (p) and neutrons (n) they contain, with proton number (Z) increasing along the vertical axis, and neutron number (N) increasing along the horizontal axis. Beta-stable nuclei, shown as black squares in Figure 1.1, exist in a band determined by a compromise between an asymmetry term (for which an energy penalty is paid for being N/Z asymmetric) and a Coulomb term (for which a penalty is paid for the like-charged protons being packed into the small nuclear volume). The tension between these terms leads to nuclei along the stability band having approximately equal numbers of protons and neutrons at low mass, but having only 35-40% protons at the upper limits of stability.

Slightly away from stability are radioactive nuclei that can be accessed experimentally, either by fragmentation or fission of heavier isotopes, or by transfer or fusion reactions.

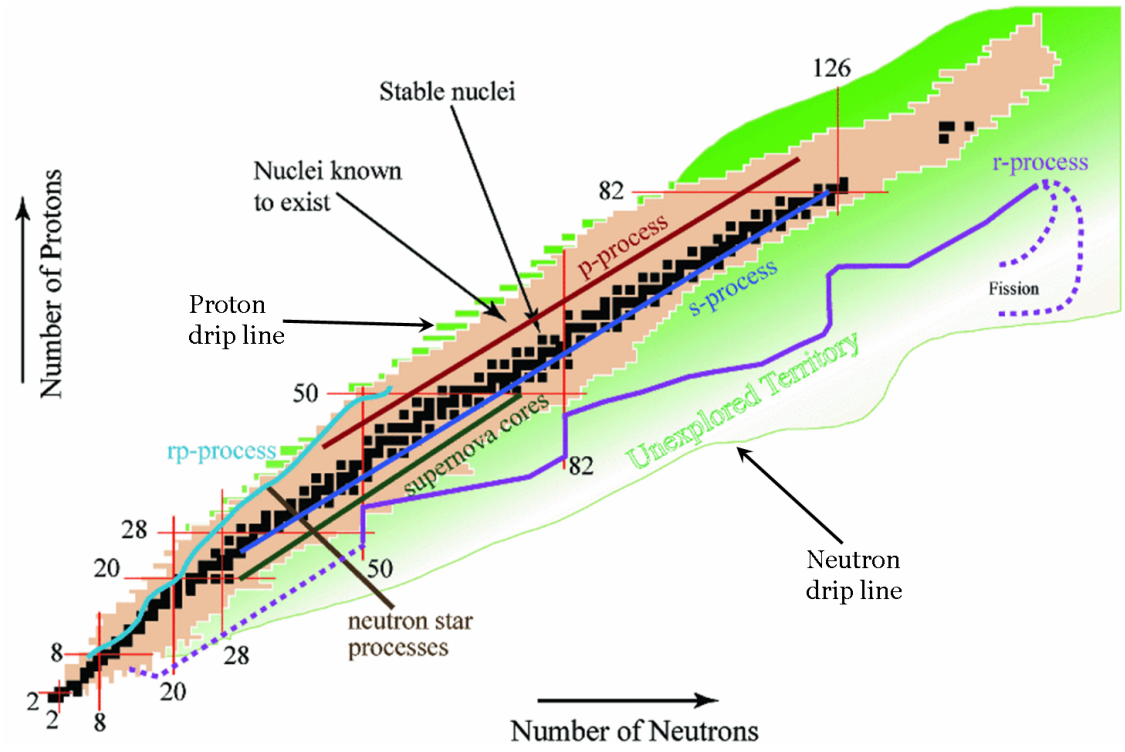

Figure 1.1: Chart of nuclides. Proton number increases towards the top of the figure, and neutron number increases towards the right. Beta-stable nuclei are shown as black squares and the shaded area around the beta-stable nuclei are those nuclei which are known to exist and have been made in the laboratory. The larger area labeled "Unexplored Territory" indicates nuclei that are believed to be bound to nucleon emission, but have not yet been observed - the drip lines form the boundaries of this region. Shell-model magic numbers are indicated for protons (neutrons) by horizontal (vertical) lines. The paths for several nucleosynthetic processes are also indicated.

The curvature of the line of stability tends to limit the product nuclei of fusion and fission processes to neutron-deficient and neutron-rich species, respectively. Further still from stability are nuclei that have not been observed experimentally, but are believed to be bound to nucleon emission. The boundaries of this "unexplored territory" are called drip lines, defined by the condition that the final p or n in a nucleus is no longer bound (i.e. the separation energy goes to zero).

Nuclei far from stability are not easily made, and many are completely inaccessible experimentally. The term "exotic nuclei" is used to describe these nuclei that are far from stability and have an extreme neutron to proton ratio (or n/p asymmetry). Studying exotic nuclei helps us to understand the properties of nuclei that are important in processes of nucleosynthesis such as the r-process (rapid neutron capture), which proceeds by a path largely in the unexplored territory approaching the n-drip line, and the rp-process, which occurs along the p-drip line.

1.2 Nuclear structure

1.2.1 Independent-particle model and shell model

The independent-particle model (IPM) is a mean-field theory whose defining approximation is to consider each nucleon (proton or neutron) in a nucleus to be moving independently in an average potential well created by all the nucleons. This simplifies the N-body problem into N one-body problems. The set of single-particle (sp) levels that result from this approach are analogous to the electronic shells in atoms.

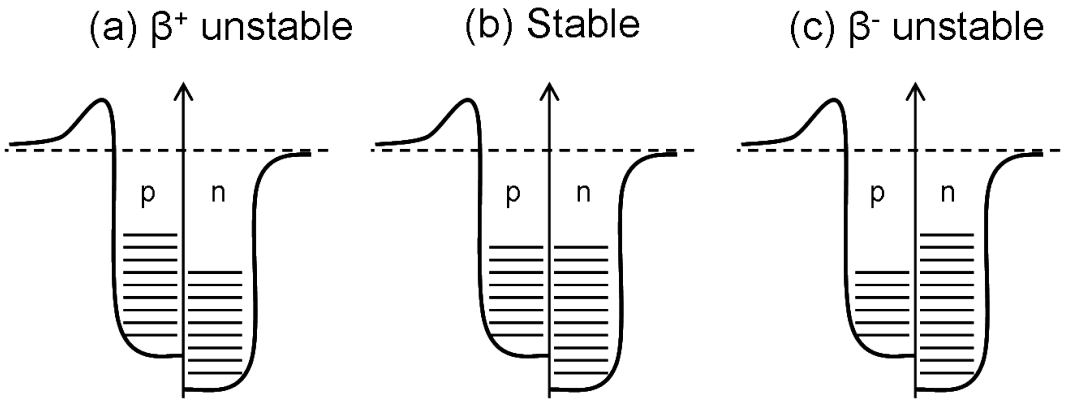

Figure 1.2: Schematics of potential wells and occupied levels for (a) β^+ unstable, (a) stable, and (c) β^- unstable nuclei. Curves are potential wells for protons (left side of each diagram) and neutrons (right side). Horizontal lines indicate filled levels.

A schematic of energy levels in nuclei is shown in Figure 1.2 for beta-unstable and stable nuclei. The potential well for protons includes a contribution from the Coulomb force, in addition to the average central potential felt by all nucleons. The Fermi level, or valence level, is the highest occupied energy level. Stable nuclei are those for which the Fermi levels for protons and neutrons are very close in energy, as in Figure 1.2b. When the Fermi level for protons is much higher in energy, as in Figure 1.2a, the nucleus is unstable and will beta decay to a lower energy configuration by converting a proton into a neutron, positron (β^+), and electron neutrino. Similarly, a nucleus for which the neutron Fermi level is at a higher energy, as in Figure 1.2c, will beta decay converting a neutron into a proton, electron (β^-), and electron antineutrino.

Calculated sp levels for the calcium isotopes that are of interest in this work ($A =$

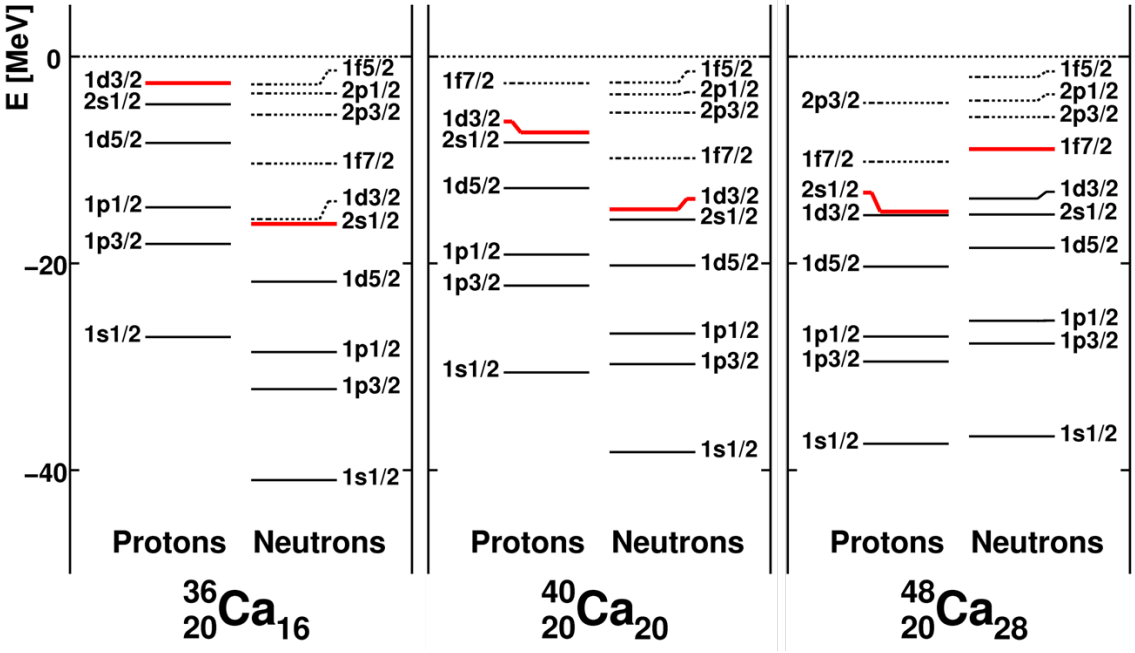

Figure 1.3: Calculated single-particle levels for calcium isotopes discussed in this work ($A = 36, 40,$ and 48). Filled levels are shown as solid lines, and unoccupied levels are shown as dotted lines. The Fermi level (highest occupied level) is shown as a thick red line. Energies are given in MeV.

36, 40, and 48) are shown in Figure 1.3. Filled levels are shown as solid lines, and unoccupied levels are shown as dotted lines. The Fermi levels are shown as thick red lines. The stable nucleus ^{40}Ca is both symmetric ($N = Z$) and closed-shell for both protons and neutrons. The neutron-rich isotope ^{48}Ca is also closed-shell and stable. The proton-rich isotope ^{36}Ca, however, is open-shell for neutrons and is unstable with a half-life of 102 ms. Its experimental proton and neutron separation energies are $S_p = 2.56\,MeV$ and $S_n = 19.1\,MeV$, respectively.

The term correlations, as used in this work, refers to interactions between nucleons that go beyond the mean field considered in an IPM approach. The nuclear shell model (SM) can account for some of these correlations by including mixing between sp states (within a finite basis set). The picture that results from this model is of a completely filled "core" (deeply bound states), with gradually decreasing occupancies near the Fermi energy due to configuration mixing. Due to the finite model space, the presence of the hard-core of the N-N interaction, and the tensor interaction (which further reduce the occupancies by shifting strength to high-momentum states), SM calculations overestimate the occupancies of bound states.

1.2.2 Spectroscopic strength and correlations

In real nuclei, the spectroscopic strength of a sp orbital is fragmented over energy. The spectroscopic factor (SF) quantifies the strength found at a discrete energy, and is defined as the norm of the one-body overlap functions (the integral over the square of the removal amplitude) [1, 2],

$$S \equiv \int d^3r |\langle \Psi^{A-1} \mid a_{\vec{r}} \mid \Psi^A \rangle|^2, \tag{1.2.1}$$

where $a_{\vec{r}}$ is the one-body nucleon removal operator, and $\mid \Psi^A \rangle$ and $\mid \Psi^{A-1} \rangle$ are eigenstates of the nuclear Hamiltonian for A and $A-1$ nuclei. In an IPM description, S is either 1 or 0. The quantity $C^2S = (2j+1)S$ is used when one wishes to take into account the angular-momentum degeneracy of a sp state. The sum of spectroscopic strength over all energies below the Fermi energy E_F gives the occupation of the orbital. Correlations reduce the occupation of a sp state relative to its IPM value, since some of the fragmented spectroscopic

strength is shifted above E_F.

Figure 1.4 shows the SF for valence protons in several closed-shell nuclei near beta stability, deduced from $(e,e'p)$ reactions. Near beta-stability, the experimental results from all investigations are consistent and indicate a roughly 35% reduction in spectroscopic strength for valence protons in these nuclei [1]. These experimental results are reproduced by many-body calculations that include correlations beyond the SM [3].

This means that while about 65% of intranuclear nucleon dynamics seems to be well described by independent-particle quantum mechanics (treating a particle as moving in an average mean-field potential formed by the other nucleons), the remainder must be interpreted as beyond the IPM. This correlated component can be divided into two roughly equal parts: a) long-range, near Fermi-surface nucleon correlations (which occur over distances of several fm) and b) a short-range part which engages nucleon pairs with high relative momentum [1].

The latter component is dominated by proton-neutron (pn) pairs with low total momentum (p_{tot}). High-energy electron-induced knockout studies show that pn pairs in ^{12}C predominate over pp pairs by 20:1 at low p_{tot} [4]. Recent results for ^{3}He are consistent with this pn pair dominance at low p_{tot} (<0.1GeV) [5]. The authors further observed that at higher p_{tot} (0.2-0.5 GeV) this dominance disappears and the abundance of pn and pp pairs becomes approximately equal. However, large p_{tot} pairs are much rarer and contribute little to the short-range correlations.

To learn about correlations away from beta-stability, one often needs to do experiments with short-lived radioactive nuclei. Since one cannot make a target from short-lived nuclei,

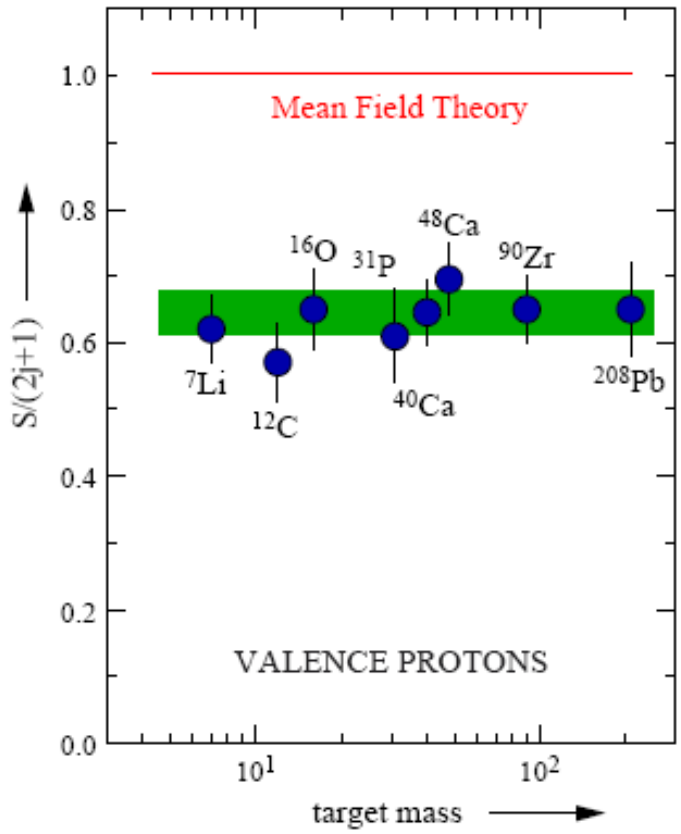

Figure 1.4: Spectroscopic factors (SF) for valence protons in beta-stable nuclei. There is a universal 30-40% reduction relative to IPM values, independent of nuclide mass. Taken from Reference [1].

these experiments are done in inverse kinematics - this means that rather than a beam of e.g. electrons being shot at a stationary target to knock out a nucleon from it, the beam itself contains the nucleus of interest and is shot at a hadronic target (usually a light nucleus such as ^{9}Be or ^{12}C) which induces the knockout. These radioactive nuclei are produced in-flight by fragmentation of a stable primary beam, and since filtering does not remove all unwanted fragmentation products, this secondary beam typically contains several nuclei (usually isotones).

Spectroscopic strength for exotic nuclei can be deduced from these hadron-induced knockout reactions in inverse kinematics with the aid of an appropriate reaction model. The results of these experiments are often presented as a reduction of the SF deduced from the experiment relative to the shell-model value, and quantified by the reduction factor

$$R_s = \frac{S_{deduced}}{S_{SM}}. \tag{1.2.2}$$

R_s is intended to be viewed as a number that evaluates the ability of a SM to reproduce the localized spectroscopic strength of orbitals near the Fermi surface. Values of R_s near 1 indicate that the nucleus is well-described by the correlations captured in a SM calculation. Small values of R_s could indicate that the spectroscopic strength has been displaced far from the energy region spanned by the intra-shell mixing of a SM. However, for this interpretation to be valid, the reaction model employed must be accurate, so that the deviation of the experimental value from the shell model value is due only to inadequacies of the SM calculation, and not to errors in extracting the SF from the experimental data.

Results of hadron-induced knockout reactions indicate that away from beta stability,

the picture of a universal 35% reduction in spectroscopic strength changes dramatically. A summary of these knockout results compiled by A. Gade (from Reference [6]) is shown in Figure 1.5 for p-knockout (red circles) and n-knockout (blue circles). R_s is plotted against ΔS (the difference in separation energy between the knocked out nucleon and the other type of nucleon).

There is consistency with the results of $(e, e'p)$ reactions (black dots) near beta stability, for which there are data available for comparison. Away from beta stability, there is a strong trend in R_s with ΔS, such that R_s is very near 1 for weakly-bound nucleons (large negative ΔS), and much smaller than 1 for strongly-bound nucleons (large positive ΔS).

This spectroscopic information can also be extracted from the analysis of transfer reactions. Not presented in this thesis is a project led by long-time collaborators at MSU to study transfer reactions with the aim of extracting SF for nuclei away from beta stability. The variation in R_s (and thus the implied change in the strength of correlations) inferred from these studies is significantly less than that suggested by the knockout results. Figure 1.6 is a plot from Reference [7] which shows the values of R_s for argon isotopes, as deduced from transfer reactions (red circles). The open and filled symbols represent values obtained using the different optical potentials indicated in parentheses. These values differ in absolute magnitude, but the trend for either potential is similar and fairly flat. This relatively small variation in R_s across the isotope chain is compared in the figure to the stronger trend in the values determined from hadron-induced knockout reactions (shown as triangles). However, the statistical significance of the difference between these trends has been questioned in a recent reanalysis of the transfer data, which finds larger uncertainties

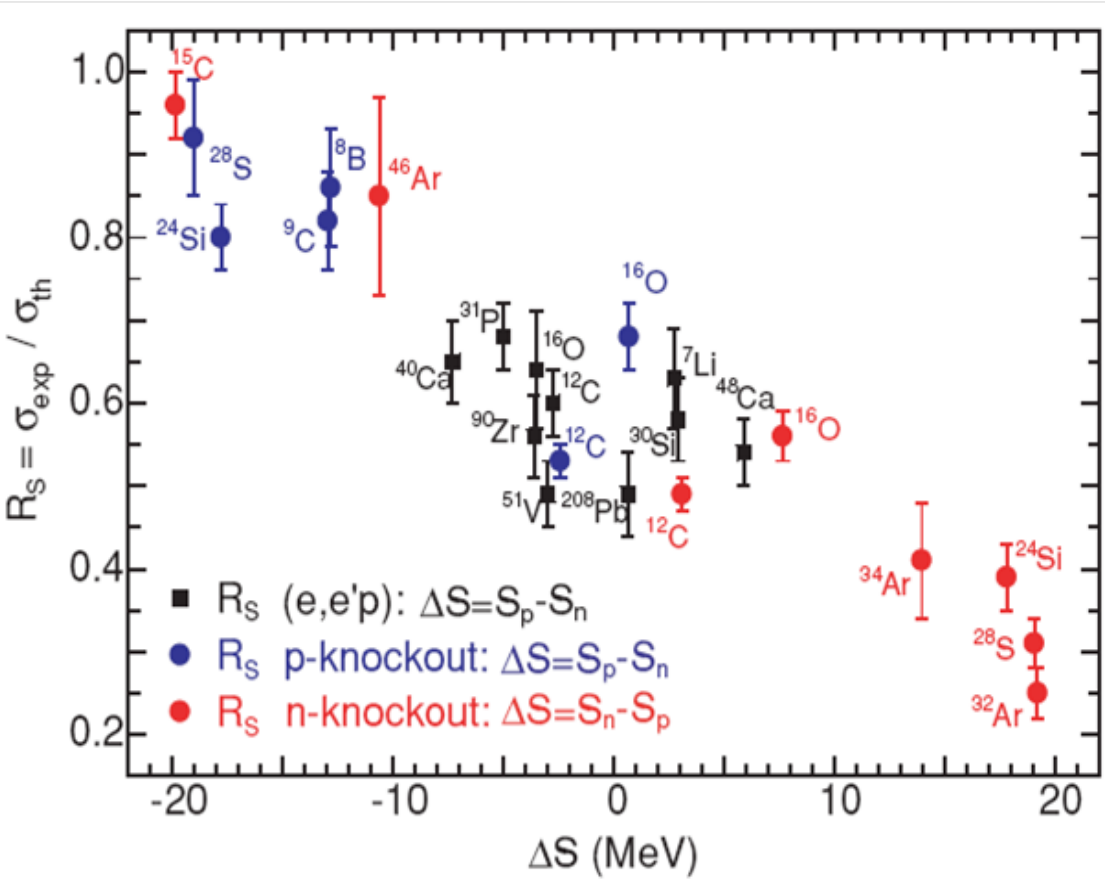

Figure 1.5: Reduction factors R_s determined from hadron-induced neutron and proton knockout are plotted as a function of ΔS, the difference in separation energy between the knocked out nucleon and the other type of nucleon. R_s is near 1 for weakly bound nucleons (negative ΔS), and very small (as low as 0.2) for deeply bound nucleons (positive ΔS). Also plotted are R_s values determined from electron-induced proton knockout (black squares) for stable nuclei. Taken from Reference [6].

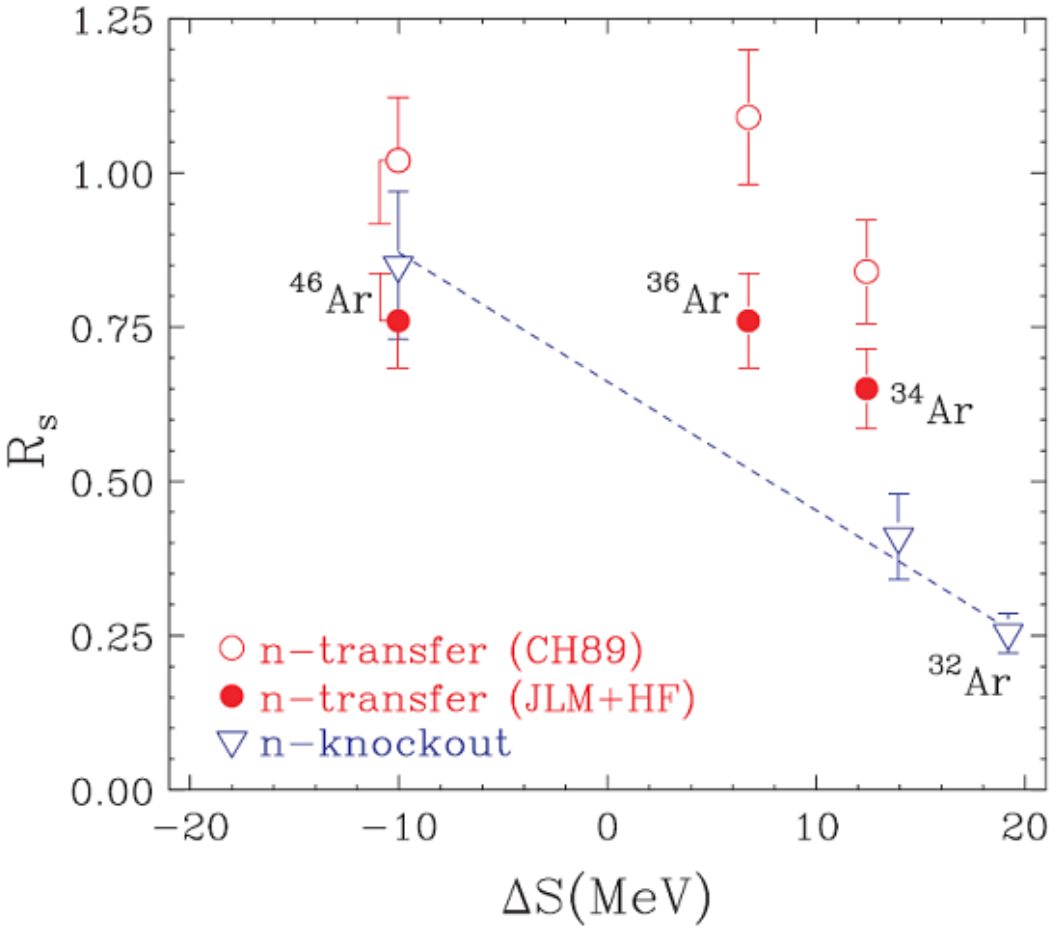

Figure 1.6: Reduction factors R_s for argon isotopes are plotted as a function of ΔS, the difference in separation energy between the transferred nucleon and the other type of nucleon. Red circles indicate R_s determined from transfer reactions (open and filled symbols are values extracted using the potentials indicated in parentheses). The relatively small variation in R_s across the isotope chain, as deduced from transfer reactions, is compared to the stronger trend in the values determined from hadron-induced knockout reactions (plotted as triangles, with a dotted line to emphasize the trend). Taken from Reference [7].

in the extracted values of R_s [8].

Another way to study these exotic nuclei is using the Dispersive Optical Model, which is described in the next section. This approach, led by other members of our research group, gives results that are consistent with those from transfer reaction studies - namely, that the strength of correlations varies with n/p asymmetry, but not as strongly as suggested by hadron-induced knockout results. Thus the spectroscopic factors even for deeply bound nucleons are expected to remain close to 0.6, rather than drop as low as the $0.2-0.3$ implied by the hadron-induced knockout studies.

1.3 Dispersive optical model

1.3.1 Optical-model potential

An optical model replaces a target nucleus by a potential well with a real part V (which is responsible for elastic processes) and an imaginary part W (which is responsible for inelastic processes). Thus it describes the interaction between an incident nucleon (the projectile) and a target not by considering the interactions between all the individual nucleons, but by an interaction between the projectile and a potential. In this work, the optical potential U, will be written

$$U = V_c + V + iW + (l \cdot s)\left[V_{so} + iW_{so}\right], \tag{1.3.1}$$

where V_c is the Coulomb potential (only needed for proton reactions), V and W are the real and imaginary parts of the central interaction (each of which can be broken down into

volume and surface parts), and V_{so} and W_{so} are the real and imaginary parts of the spin-orbit term.

This complex optical-model potential is a compact representation of the physics required to explain both the elastic-scattering observables (differential cross sections, analyzing powers and spin rotation parameters) and the inelastic contributions. The interplay between the refracting real potential (which is responsible for the bulk of the elastic scattering), and the absorbing imaginary potential (accounting for all the inelastic processes) generates the angular-dependent observables as well as the evolution of cross sections with incident energy.

By enforcing causality, a dispersive version of the optical model (DOM) can be generated [9]. The real part of the potential, which is energy-dependent and non-local in space, is written as the sum of its value at the Fermi energy (V_{HF}) and a local dispersive correction ($\Delta\mathscr{V}$),

$$V\left(E,\overrightarrow{r},\overrightarrow{r}'\right)=V_{HF}\left(\overrightarrow{r},\overrightarrow{r}'\right)+\Delta\mathscr{V}\left(E,\overrightarrow{r}\right). \tag{1.3.2}$$

Rather than work with a non-local potential, the former term is approximated by an energy-dependent, local form

$$V\left(E,\overrightarrow{r},\overrightarrow{r}'\right)\approx V_{HF}\left(E,\overrightarrow{r}\right)+\Delta\mathscr{V}\left(E,\overrightarrow{r}\right). \tag{1.3.3}$$

Analogously to the situation in optics, the dispersive correction is linked to the imaginary potential by a dispersion relation, which (dropping the spatial dependence for clarity) is written

$$\Delta\mathscr{V}(E) = \frac{1}{\pi}\mathscr{P}\int W(E)\left(\frac{1}{E'-E} - \frac{1}{E'-E_F}\right)dE', \tag{1.3.4}$$

where $\mathscr{P}$ stands for the principle value of the integral.

The functional form of the optical potential is suggested by both theoretical expectations and analysis of previous experimental observations [10]. The parameters of the potential are then extracted by fitting large data sets [11]. From this potential, one can calculate level properties of the nucleus, such as the energy, width, and spectroscopic factors of bound and quasi-bound states.

The energy dependence in the DOM is of two types - a fundamental energy dependence from the dispersive correction, and an artificial energy dependence that is the result of approximating V_{HF} by a local potential. The energy dependence of the real potential reports on the effective mass, a device which embodies the nucleon-nucleon (N-N) correlation effects. (It is this effective mass that captures the non-localities of the interaction, which lead, in part, to the understanding that the N-N interaction is momentum dependent.) On the other hand, it is the energy dependence of the imaginary potential that reports on the spectroscopic strength or (via integration over energy) the single-particle occupation probabilities. The latter differ from the expectations of an extreme single-particle model, due to the fact that nuclei are correlated many-body systems. They are also less than SM values due to intershell physics only captured in a SM by rescaling of operators (effective operators).

1.3.2 Incorporating asymmetry dependence

Since nuclei near the driplines are difficult to access experimentally, one approach to understanding the properties of these exotic nuclei is to extrapolate towards the dripline using data on nuclei near beta-stability. As is typical for extrapolations, the more robust the physical "scaffold" on which the extrapolation is built, and the greater the quantity and quality of data that is fit, the better the extrapolation. To facilitate an extrapolation, work is being done by Charity, et al. to incorporate isospin into the DOM [12]. Initially, this was done by adding a term to the surface imaginary potentials that was proportional to the neutron to proton asymmetry $\delta = \pm\frac{N-Z}{A}$ (+ for protons, - for neutrons). As will be discussed later, this simple approach was not entirely successful and was abandoned in a more recent analysis [10]. However it provides a starting point to understand the asymmetry dependence.

To motivate the placement of this asymmetry dependence into the surface imaginary part of the potential, one can compare the reaction cross section σ_{react} for protons on Sn and Ca isotopes (plotted in Figures 1.7b and 1.8b) to the corresponding integrated imaginary potential J_W, as determined from elastic scattering data (plotted in Figures 1.7a and 1.8a). One can see that J_W and σ_{react} roughly track each other across the isotope chains. At these experimental energies ($\sim 20-25\,MeV$), the imaginary potential is dominated by the surface part W^{sur}, making it the logical place to incorporate an asymmetry dependence.

Reference [12] describes the results of this first attempt at incorporating an asymmetry dependence into the DOM, using data for $N > Z$ nuclei. Briefly, the simple $\pm\frac{N-Z}{A}$ scaled form described the data successfully for protons, but not very well for neutrons. In the

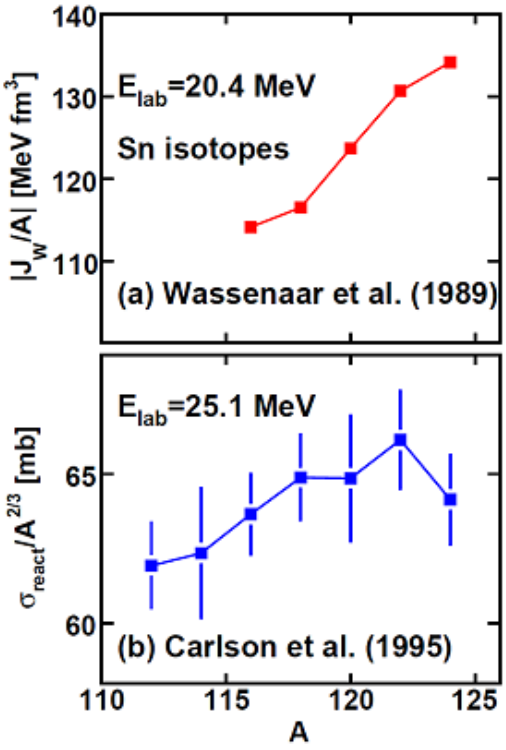

Figure 1.7: Top pane shows the integrated imaginary potential J_W, deduced from proton elastic scattering, for tin isotopes as a function of mass A. The bottom pane shows the corresponding proton reaction cross sections. To account for differences arising solely from increasing isotope mass the values of J_W and σ_{react} are scaled by A and $A^{2/3}$, respectively. Taken from Reference [10].

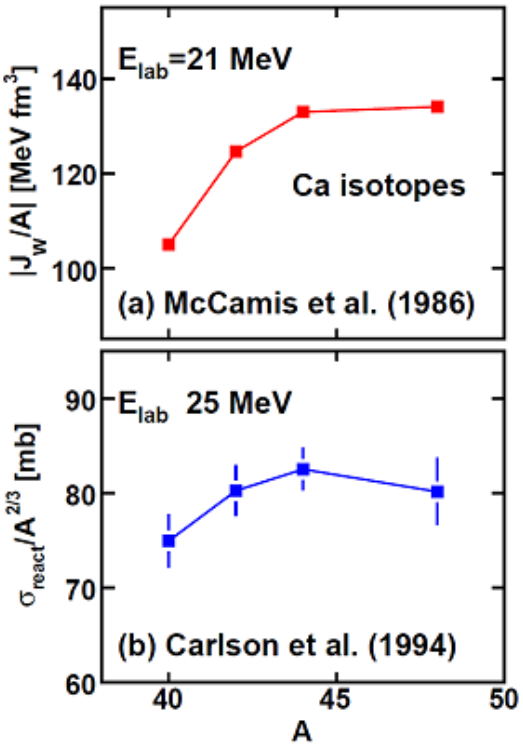

Figure 1.8: Same as Figure 1.7, but for calcium isotopes. Taken from Reference [10].

latter case, it resulted in some unphysical neutron potentials. The authors did a second analysis with the asymmetry term for neutrons set to zero. This approach was more successful, however the available data for neutrons did not strongly constrain this dependence. They noted that predictions for ^{48}Ca elastic-scattering cross sections (using different forms for the asymmetry dependence) showed a sensitivity to the asymmetry dependence and suggested that measurements for asymmetric nuclei could improve the understanding of neutron correlations. The ^{48}Ca elastic-scattering measurements have now been done by our group, in a project in which I participated, but which is not discussed in detail here because others were responsible for the analysis. These data were incorporated into the updated DOM analysis [10] along with the $\sigma_{tot}(n)$ measurements described in this work. The results of this updated analysis will be referenced in Chapter 2.

1.4 Cross-section calculations

1.4.1 Elastic and reaction cross sections from DOM

One can calculate many nuclear properties from the optical potential, including the proton and neutron elastic-scattering and reaction cross sections. These cross sections are given by [13]

$$\sigma_{el} = \frac{\pi}{k^2}\sum_{l=0}^{\infty}\left\{(l+1)\,|1-S_{l^+}|^2 + l|1-S_{l^-}|^2\right\} \tag{1.4.1}$$

$$\sigma_{react} = \frac{\pi}{k^2}\sum_{l=0}^{\infty}\left\{(l+1)\left(1-|S_{l^+}|^2\right) + l\left(1-|S_{l^-}|^2\right)\right\}, \tag{1.4.2}$$

where the complex function S is the so called scattering matrix (S-matrix), l is the orbital angular momentum, and $k\ \left[fm^{-1}\right]$ is the wavenumber ($k = \frac{1}{\lambda\!\!\!^{-}}$, where $\lambda\!\!\!^{-}\ [fm]$ is the reduced deBroglie wavelength). Spin-orbit splitting leads to the two terms, one for $j = l + 1/2$ and the other for $j = l - 1/2$, indicated by subscripts l^+ and l^-, respectively. The total cross section (finite for neutrons) is the sum of these, i.e.

$$\sigma_{tot} = \sigma_{el} + \sigma_{react}. \tag{1.4.3}$$

The S-matrix partitions the incoming flux amongst reacting and non-reacting channels, as indicated by the equations above, and it can be extracted from a complex optical potential (see Section 3.3). The reaction cross section can be understood in an intuitive sense by identifying the quantity $1 - |S|^2$ as the transmission coefficient, which represents flux that is removed from the elastic channel and is transmitted through the potential barrier (and is therefore allowed to react, e.g. to be captured).

The believability of these calculated cross sections obviously depends on that of the S-matrix, which in turn depends on the trustworthiness of the optical potential from which it is calculated. The quality of the DOM optical potential is displayed by the fact that it reproduces a wide range of data. For example, a global fit to calcium and nickel isotopes and $N = 28$ isotones included over 200 data sets, encompassing elastic scattering measurements, proton and neutron reaction and neutron total cross sections, spectroscopic factors and rms radii from $(e, e'p)$ measurements, and sp level energies. Thus the DOM is highly constrained by experimental reality, giving one confidence in the results obtained with it.

1.4.2 Hadron-induced knockout cross sections from eikonal theory

Spectroscopic information is deduced from hadron-induced knockout reactions by comparing the experimental cross sections to those calculated using some reaction theory. In the case of an eikonal reaction theory, the calculations (discussed in Chapter 3) have been shown to describe well the momentum distributions of the mass $A-1$ knockout residue. And, as mentioned above, there is consistency with the results of $(e,e'p)$ reactions near beta stability.

However, unlike the case for the elastic scattering and total cross sections as calculated from optical models, the theory used to analyze hadron-induced knockout experiments is not required to reproduce a wide array of experimental data. Additionally, these theories of heavy-ion induced knockout contain the inherent complexity of needing to model the interaction of two extended bodies - one group of nucleons (in the target) interacting with a second group of nucleons (the nucleus of interest). In contrast, the reactions considered in the DOM analysis are much simpler, and one needs only consider the reaction of a single nucleon with the nucleus of interest.

1.5 Learning about correlations from experiment

This work will discuss two experiments which were undertaken to investigate how nuclear correlations change with n/p asymmetry - measurement of the neutron total cross section of ^{48}Ca and the hadron-induced single-nucleon knockout cross sections for ^{36}Ca. Although a full introduction to each experiment is presented in their respective chapters, a brief com-

ment about these experiments and why they were undertaken is included here.

1.5.1 Neutron total cross section measurements

Dietrich and co-workers report the neutron total cross sections of two tungsten isotopes (with $A = 182, 186$), along with several calculations for the energy dependence of the difference in cross section between the two isotopes [14]. As will be discussed in Section 2.1, they note that a calculation which sets the isospin term in the potential to zero actually better reproduces the measured isotopic differences. This points to the fact that $\sigma_{tot}(n)$ measurements on chains of isotopes (or isotones) can supply information on the isospin dependence of the potential. From this potential, one can calculate spectroscopic factors, and then infer information about correlations.

The calcium isotopes ^{40}Ca and ^{48}Ca differ by 8 neutrons. This large range in asymmetry makes the pair an excellent starting case to examine asymmetry dependences. There were no previous $\sigma_{tot}(n)$ data for ^{48}Ca above 15 MeV, and the low-energy data had large uncertainties. This is characteristic of the available isotopically separated data for neutron reactions, which are typically limited in both the energy range covered and the precision of the measurements (see discussion in Chapter 2). This work developed a digital-signal-processing technique for measuring $\sigma_{tot}(n)$ on small samples, and used it to extend the data for ^{48}Ca up to 300 MeV with uncertainties of only a few percent. Thus, in addition to yielding these new data, this project generated a technique suitable for $\sigma_{tot}(n)$ studies on rare (and therefore expensive) stable isotopes. The contents of Chapter 2 have been expanded from a previously published article [15].

1.5.2 Hadron-induced single-nucleon knockout reactions

Although the reduction in occupancy of a sp state due to correlations is not a direct experimental observable, it can be inferred from particle-removal reactions by comparing the experimental cross section to an expected cross section which has been calculated using some reaction theory. As described above, previous studies of hadron-induced knockout have indicated a strong trend in the strength of correlations with neutron-proton asymmetry [6]. This trend is inferred from small experimental cross sections for knockout of deeply bound nucleons, as compared to the cross sections calculated in an eikonal reaction theory. This reaction model is discussed in Section 3.3.

The previous DOM results and the transfer reaction results were in conflict with this strong trend observed for the knockout reactions mentioned above. As an example, the DOM extrapolation for the SF of the valence neutron in ^{36}Ca was 0.6, while the trend inferred from knockout experiments would place this number at close to 0.2. The measurement of neutron and proton knockout from ^{36}Ca was undertaken to confirm the small experimental cross section for knockout of the deeply-bound neutron, and further analysis was done in an attempt to understand the discrepancy between the knockout results on one hand, and the DOM and transfer results on the other hand.

Chapter 2

Neutron correlations in calcium isotopes

2.1 Background

The evolution of the in-medium (N-N) correlations with n/p asymmetry has attracted considerable attention in recent years [16]. It has been argued that n/p asymmetry effects are strong [16] or weak [7, 12, 17] functions of the binding energy of the nucleon. Results from hadron-induced nucleon-knockout reactions, with radioactive beams, make the case that the more strongly bound the nucleon, the greater the suppression of single-particle strength [16]. The DOM results are more subtle but indicate a weaker trend, which likely depends on the relative importance of the various low-lying collective excitations and the parity of the particles and holes that can be generated near the Fermi surface. Nucleon-transfer reactions suggest that, for neutrons, the suppression of single-particle strength has little to no dependence on the binding energy [7].

While there are certainly notable gaps in the isotopically resolved data for proton reac-

Table 2.1: Status of $\sigma_{tot}(n)$ for Ni and Sn isotopes, and $N = 28, 50$ isotones.

Ni (%)	E (MeV)	**Sn (%)**	E (MeV)	$N = 28$ **(%)**	E (MeV)	$N = 50$ **(%)**	E (MeV)
Nat	<550	**Nat**	<1000	^{48}**Ca (0.2)**	<300	^{87}**Rb (27.8)**	<10
58 (68.3)	<30,<65*	**112 (0.97)**	<12	^{50}**Ti (5.4)**	14	^{88}**Sr (82.6)**	14
59 (-)	<1	**114 (0.65)**	<2	^{51}**V (99.8)**	<15,<20*	^{89}**Y (100)**	<550
60 (26.1)	<30	**116 (14.53)**	<2,14	^{52}**Cr (83.8)**	<15,<30*	^{90}**Zr (51.5)**	<600
61 (1.1)	<10*	**117 (7.68)**	<14	^{54}**Fe (5.9)**	<7,<200	^{92}**Mo (14.8)**	<6*
62 (3.6)	<1,4,14	**118 (24.22)**	<26**				
64 (0.91)	<1,14	**119 (8.58)**	14				
		120 (32.59)	<26**				
		122 (4.63)	<26**				
		124 (5.79)	<26**				

* Large uncertainty, ** Few data

tion cross sections, the database for total neutron cross sections of separated isotopes is far from complete. For example, the NNDC database (the Brookhaven maintained database for nuclear structure and reaction data) does not contain total neutron cross sections $\sigma_{tot}(n)$, covering a broad energy range, for the $N = 28$ isotones (i.e. ^{48}Ca, ^{50}Ti, ^{52}Cr or ^{54}Fe), the Ni isotopes, the Sn isotopes, the $N = 50$ or $N = 82$ isotones. A summary of the existing data for these are presented in Table 2.1. As has been shown in standard optical-model analyses (as well as DOM work) such data, often presented as isotopic differences to reduce systematic errors [14, 18, 19, 20], provide sensitivity to the isovector components of the potential. This can be seen in Figure 2.1, which shows such results for $\sigma_{tot}(n)$ measurements on tungsten isotopes from Reference [14]. The solid curve shows an optical-model-like (Ramsauer model) calculation including isospin, while the dotted curve shows a calculation with the

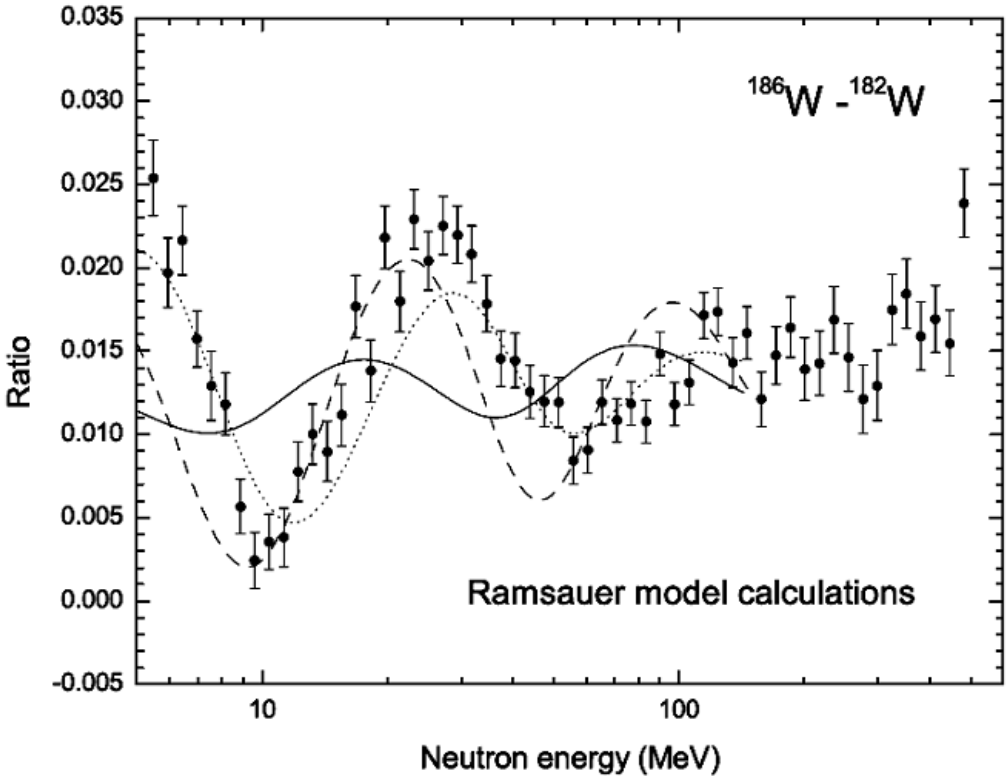

Figure 2.1: Data points show isotopic differences in $\sigma_{tot}(n)$ for tungsten isotopes as a function of neutron energy. The solid curve shows a full Ramsauer model calculation (including isospin), while the dotted curve shows a calculation with the isospin term in the potential set to zero. (The dashed curve is unimportant for the discussion here.) Taken from Reference [14].

isospin term in the potential set to zero. (The dashed curve is unimportant for this discussion.) The authors note that neglecting isospin actually reproduces the magnitude and energy dependence of the data better, which points to the fact that $\sigma_{tot}(n)$ measurements on chains of isotopes (or isotones) can supply information on the isospin dependence of the potential. One can view the collection of such data as an effort complementary to the collection of nucleon-knockout cross sections and transfer-reaction data using radioactive beams.

The main problem with measuring $\sigma_{tot}(n)$ for separated isotopes is the need for substantial amounts of target material (large fractions of a mole) that must be of high isotopic purity. Presented here is a technique (based on digital-signal processing) that significantly lowers the amount of target material needed.

The case study for this work is ^{48}Ca (perhaps the most interesting of the cases mentioned above). Our sample was only 0.056 of a mole, with an inverse areal density of 35 $b/atom$ (2400 g/cm^2). This areal density is about 10 times less than conventionally used. Furthermore, we show that the technique we developed would be better suited to even smaller samples than we used in this initial study. This allows for a program of measuring $\sigma_{tot}(n)$ for rare (stable) isotopes throughout the periodic table.

Figure 2.2: The proton-beam pulse structure at LANSCE WNR. The micropulses are repeated at 1.8 μs intervals for 625 or 725 μs (macropulse). The macropulse was repeated at 60 Hz, or every 16.7 *ms*. One in three macropulses (shown in gray) was delivered to another facility.

2.2 Experimental details

2.2.1 Beam and sample characteristics

Our source of neutrons was the Los Alamos Neutron Science Center (LANSCE) WNR facility [21, 22]. The LANSCE beam structure is shown in Figure 2.2. A proton beam of 800 MeV with an average intensity of 2 μA bombarded a tungsten target producing a white (i.e., continuous energy) source of neutrons. The proton pulses (referred to as micropulses) are less than 1 *ns* in width and were repeated at 1.8 μs intervals for a period for 625 or 725 μs (referred to as a macropulse). The macropulse was repeated at 60 Hz, or every 16.7 *ms*. One in three macropulses (shown in gray in Figure 2.2) was delivered

to another facility. This time structure of the beam results in large dead times in standard measurements of neutron cross sections, as discussed in Section 2.6.2.

The beam-line layout is shown schematically in Figure 2.3. Neutrons exiting the production target room at 15° from the proton-beam axis were collimated using 2 feet of 4"-diameter steel with a 3/8"-diameter opening. The samples were located in a 5-position sample changer located approximately 20 *m* from the neutron source. Transmitted neutrons were detected in two fast-plastic scintillator paddles (1/4" and 2" thick) at mean distances of 42.56 and 42.65 *m* from the source. A thin (1/16" thick) monitor paddle, placed upstream of the samples, was used to correct for variations in beam intensity between samples.

All samples were right cylinders with 1/2" diameters, sheathed in open-ended cylindrical shells of high-density closed-cell Styrofoam. The outer diameter of these shells matched the diameter of the 5 cradles of the sample changer. To limit oxidation, the two calcium samples were enclosed by gluing 870 $\mu g/cm^2$ (1/4 mil) Mylar over the ends of the Styrofoam while in an argon environment. The physical parameters of each of the targets (a ^{nat}Ca, in addition to the ^{48}Ca, and two ^{nat}C samples of different lengths) are provided in Table 2.2. The fifth position in the sample changer contained an empty Styrofoam shell for the "sample-out" measurement. In the course of the 15-day experiment, each sample was exposed to approximately 10^7 macropulses. The exact *n*-source-to-detector distance was determined by matching to known carbon resonances near 16.5 and 20 *MeV* [20], as described in Section 2.3.1.2.

The samples were cycled through the beam using a linear-stage translation table, with the adjustable wait time set to 150 seconds. In order to keep oxidation of the Ca samples

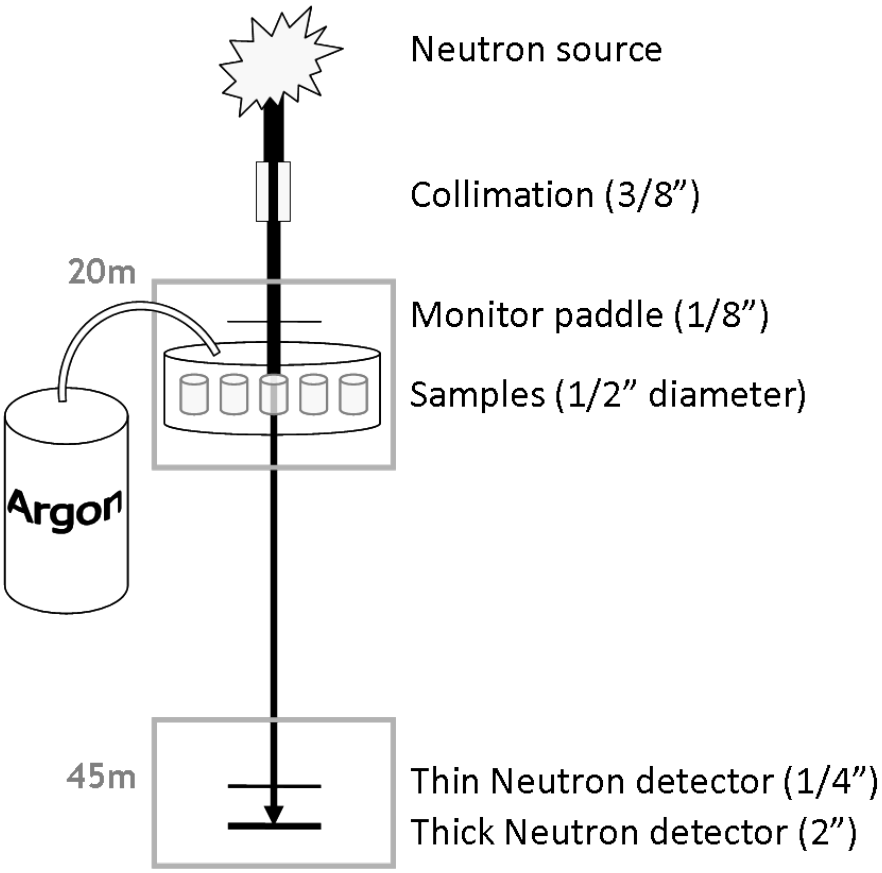

Figure 2.3: The layout of the beam line (WNR 15 L). An 800-*MeV* beam of protons hit a tungsten target producing neutrons. Five samples (including a blank) were held in a sample changer which cycled at set intervals, typically waiting 150 seconds on each sample. Transmitted neutrons were detected 45 *m* downstream of the production target in either a thin or a thick fast-plastic scintillator. A very thin scintillator was placed upstream of the samples and data from this monitor were used to correct for any variations in the beam intensity. To minimize oxidation of the calcium, the sealed samples and sample changer were placed in a chamber through which argon flowed for the duration of the experiment.

Table 2.2: Sample characteristics.

Sample Name	Mass [g]	Diameter [mm]	Length [mm]	$1/nl$ [$b/atom$]	nl [g/cm^2]	Isotopic composition
^{48}Ca	2.7170	12.7	11.94	34.8	2402	^{40}Ca: 7%, ^{48}Ca: 92.3%, other: <1%
^{40}Ca	2.742	12.7	14.46	30.7	2424	Natural - ^{40}Ca: 96.9%, ^{44}Ca: 2.1%, other: <1%
^{12}C (1/2")	2.6697	12.70	12.71	9.46	2361	Natural - ^{12}C: 98.9%, ^{13}C: 1.1%
^{12}C (1")	5.3407	12.69	25.42	4.72	4722	Natural - ^{12}C: 98.9%, ^{13}C: 1.1%

to a minimum, the translation stage was housed near the bottom of a cylindrical chamber, approximately 12" tall and 12" diameter (axis vertical), through which high-purity argon flowed continuously. The beam entered and exited this chamber through thin Mylar windows. (This Mylar is present for both sample-in and sample-out measurements.) In order to facilitate loading and unloading the sample chamber, a small nut was glued onto the exterior top of each Styrofoam shell. A long rod was threaded into this nut to lower the samples onto the translation table. A DC output from the cycling controller proportional to sample number indicated which sample was in the beam. This voltage was zero when the sample changer was in motion.

2.2.2 Detectors and data acquisition

Thin (1/4") and thick (2") fast-plastic scintillators (BC-408) served as the *stop* detectors. The thin detector had a single photomultiplier tube (PMT) while for the thick one, shown in Figure 2.4, two 2"-diameter PMT's (RCA 8575) were connected on opposite ends of the scintillator. The two PMT signals were added together after gain and time matching. A slight day/night variation (less than 1 *ns*) in the time matching was noted. This was presumed to arise from slightly different thermal profiles of the two cables running from the detectors (sited in an open field in a small weatherized housing) to the data trailer which housed the pulse processing and acquisition hardware.

Signal digitization was performed using 8-bit Acqiris model DC265 cPCI-based digitizer boards with 2Mb or 256kb on-board memory [23]. The signals from all the detectors (downstream *n* detectors and monitor) and the cycling controller were digitized and ana-

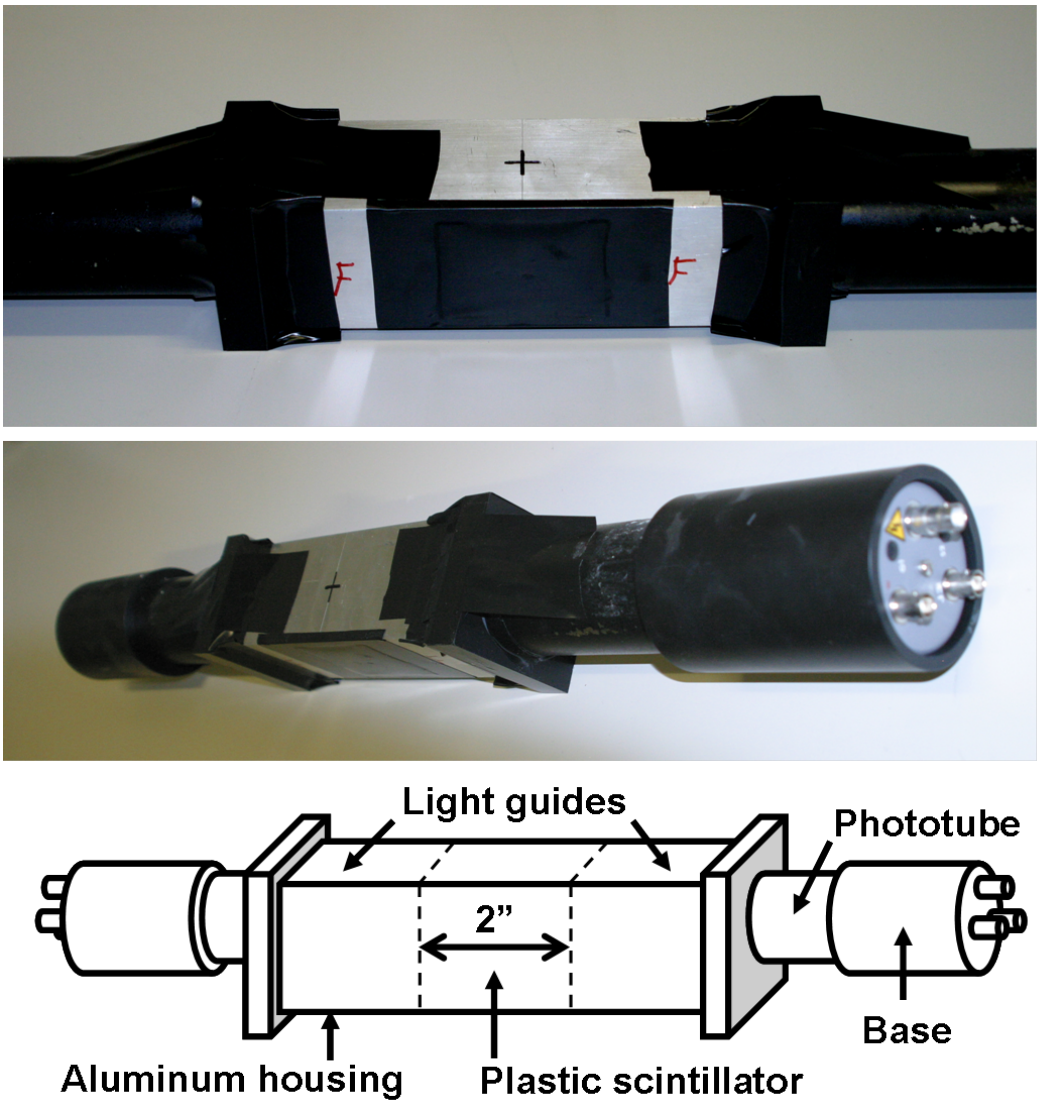

Figure 2.4: Photos and schematic of 2” stopping detector. The plastic scintillator detector is sensitive to photons and neutrons. This detector provided the *stop* for the time-of-flight measurement, and the *start* was provided for each macropulse as described in the text (Section 2.3.1.2).

lyzed between macropulses. This task could not be completed if each PMT output was digitized separately, which necessitated the merging of the signals from the two ends of the thick detector. The DC output signal from the cycling controller was sampled every 500 *ns* and the resulting waveform was recorded in the data stream for offline analysis. The PMT output signals were sampled every 50 *ns* (monitor) or 5 *ns* (downstream neutron detectors). An example of the digitized neutron-detector voltage for one macropulse (referred to as a waveform) is shown in Figure 2.5. Each peak in the waveform corresponds to a detected particle, of which there are, depending on target, about 600 per macropulse, corresponding to about 1 per μs. (This rate of useful *stops* exceeds that of the standard event-by-event stop-start technique by more than an order of magnitude. In the standard event-by-event logic, the event rate is limited by the event-acquisition dead time, a time of the order of 10's of μs.) The 8-bit resolution of the digitization boards limited the dynamic range of the system, resulting in some saturation of the pulses from very high-energy neutrons.

Between macropulses, the waveforms were analyzed using a simple algorithm to look for peaks. When the signal magnitude exceeded the hardware threshold of 30 mV, it was counted as a single peak until the signal magnitude falls below the threshold again. The threshold-crossing time was recorded in the data stream, as well as 15 voltage samples around the peak (to allow for offline peak fitting, Figure 2.6). In addition to storing each 15-sample "peaklet", we stored 1% of the macropulse waveforms (125,000 samples per 625 μs pulse). These waveforms allowed for the determination of the full functional form of the time response of the scintillator, i.e. including the extended tail. These full waveforms were also essential for determining the energy-dependent dead-time losses resulting from

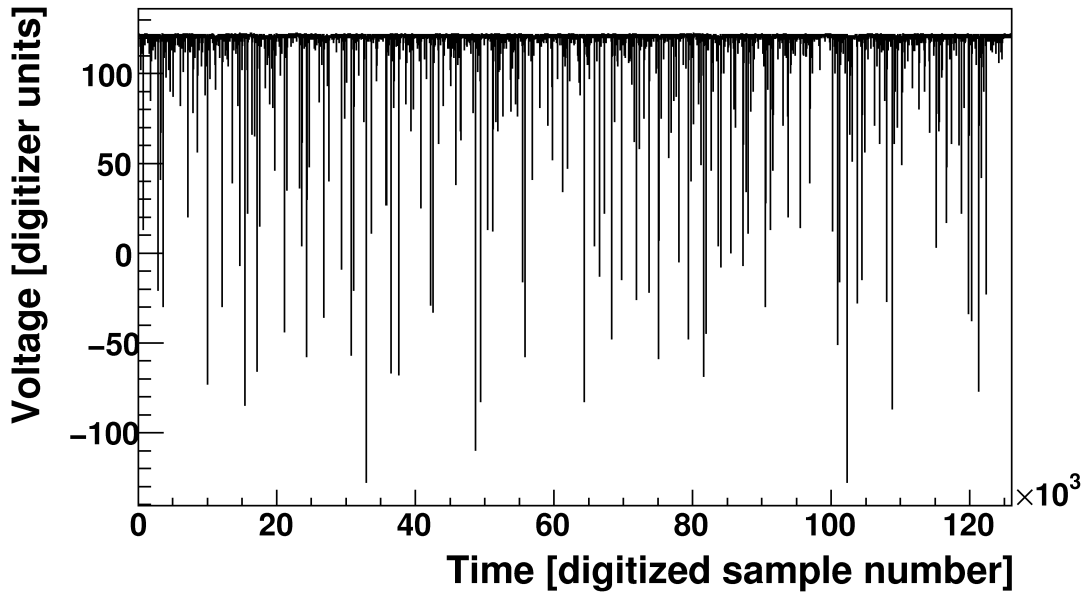

Figure 2.5: Detector signal (digitized PMT output) for one macropulse. The PMT outputs were sampled every 5 *ns*. This waveform (shown above) was stored in the buffer and then analyzed between macropulses to find peaks exceeding a certain threshold. A typical macropulse had around 600 such peaks, each one corresponding to a detected neutron or γ-ray. For each peak, the threshold crossing time was recorded in the data stream, as well as 15 voltage samples around the peak (to allow for offline peak fitting). In addition, 1% of the full waveforms were recorded in the data stream.

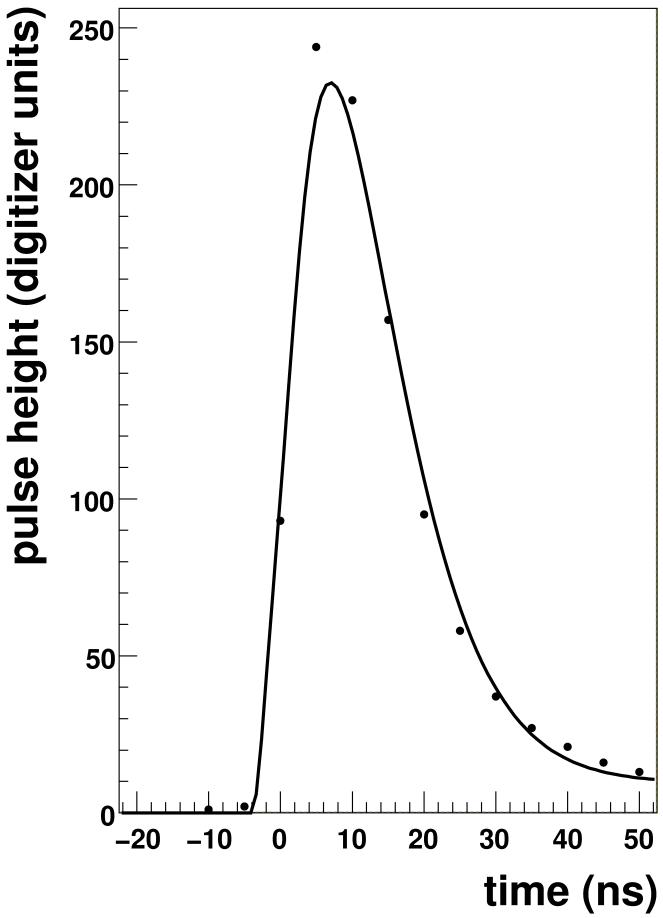

Figure 2.6: Example fit of 15 recorded voltage samples around a peak. Using the line shape determined by fitting the whole pulses, and the area calculated by a Riemann sum of the pulse heights (multiplied by a factor to account for the fraction of the pulse beyond the recording window, about 20%), the only free parameter left was the time offset (relative to threshold crossing). A one-dimensional χ^2 minimization was used to determine this time offset to the nearest 0.25 *ns*.

our storing of only "peaklets" by the procedure described above.

Because the waveforms were collected in the digitizer-board buffer during the macropulse and not transferred to the computer to be processed until the macropulse ended, there were no dead-time losses associated with transfer and processing as long as this transfer was completed before the next macropulse arrived (about 16 *ms* later). This made it possible to obtain high statistics for both sample-in and sample-out measurements, thus allowing cross sections with small statistical uncertainties to be determined using samples much smaller than are required for traditional signal processing. For example, the samples used in a previous set of total cross-section measurements at LANSCE [20, 14] were on the order of a mole or larger. (The previous study of Ca used 326 g of CaF_2. The Ca cross sections were extracted via a difference.) Event-by-event studies typically used samples with areal densities roughly 5-15 times larger than our calcium samples.

There was an energy-dependent dead time due to the simplicity of the peak searching algorithm yielding the peaklets. Pulses from particles that arrived before a previous signal had fallen below the threshold were not counted. This led to sample- and energy-dependent dead-time losses. The time-of-flight spectra for both the sample and blank needed to be corrected for this loss before calculating the cross section. The 1% of the full waveforms recorded were used to determine the smooth energy-dependent correction for these dead-time losses. These corrections were less than 2% below 25 MeV but increased to as much as 18% at 250 MeV. While this correction is substantial (at high energy) it is smaller in magnitude than those typically needed for the standard event-by-event analog technique [24]. The only assumption in the correction scheme we employ is that the dead-time correction

is a smooth function of energy (see below).

2.3 Analysis

2.3.1 Cross-section calculation

2.3.1.1 Definition of cross-section

The total neutron cross-section σ relates the incident neutron flux I_0 to the transmitted neutron flux I by the equation

$$I = I_0 e^{-nl\sigma}, \tag{2.3.1}$$

where nl is the areal density, n is the number density of nuclei in the sample (nuclei per unit volume) and l is the length of the sample. In place of neutron fluxes (measured in neutrons per unit time) we can instead use the number of neutrons N and N_0, in effect, multiplying both sides of the equation by the time of the measurement (N is the number of detector counts when a sample is in the beam, N_0 is the number of detector counts when the blank is in the beam, and both are normalized by the number of counts in a monitor). Then the experimental cross section is

$$\sigma = \frac{1}{nl} \ln \left[\frac{N_0}{N} \right]. \tag{2.3.2}$$

2.3.1.2 Time-of-flight and energy determination

The cross section was calculated as a function of incident neutron energy. The energy of each detected neutron was determined relativistically from its time of flight (TOF) between

the neutron source and stopping detector. Relativistic corrections were around 50% at the upper end of the energy range ($E_n = 300 MeV$) and about 1% near the lower end ($E_n = 10 MeV$).

Each recorded event in the data stream includes a list of times associated with all the detected neutrons in one macropulse. These are not TOF values, which would be measured relative to the start of a *micropulse*, but rather the time between the start of the *macropulse* (provided by a logic signal from the machine RF) and the particle detection. Furthermore, these times are shifted relative to the logic signal, due to differing cable lengths. The amount of this shift can be calculated using the TOF of the photons, which requires knowing the exact flight distance. The exact flight distance (from neutron source to detector) was determined by matching to known resonances in ^{12}C, shown in Figure 2.7, while at the same time constraining the position of the gamma flash to match the expected TOF.

Figure 2.8 shows a portion of the macropulse time spectrum. One can see the repetition of the TOF spectrum, once for each micropulse. Since there are many micropulses in each macropulse, the event must be collapsed using the repetition frequency of the micropulses to turn the raw times (time relative to macropulse start) into TOF (time relative to micropulse start). This frequency is nominally 1.8 μs, but is determined more precisely by manually adjusting it to minimize the width of the gamma flash (since an incorrect value of this frequency will result in the micropulses not lining up well, and will cause the peak from the gamma rays to widen). The collapsed times from each event are then histogrammed to obtain a TOF spectrum, an example of which is shown in Figure 2.9. The cross section is calculated in each bin according to Equation 2.3.2, using the TOF spectra for the sample

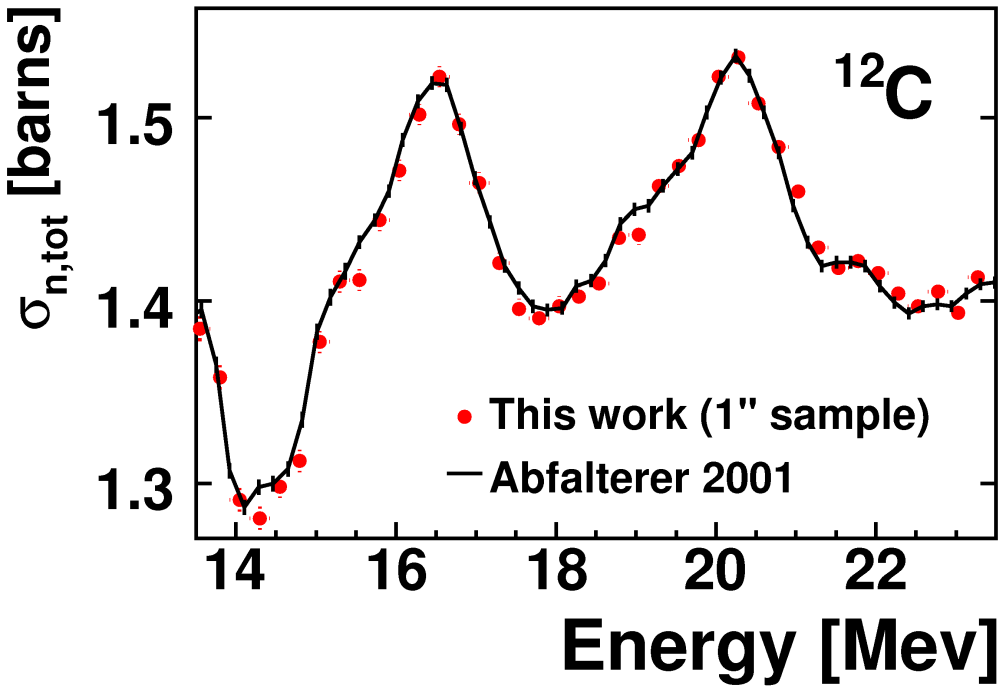

Figure 2.7: Low-energy resonances in ^{12}C that were used to calibrate the TOF spectra. The black line shows previously published data [20] and the dots show our data points. The flight distance was adjusted so that these known resonances were at the correct energy.

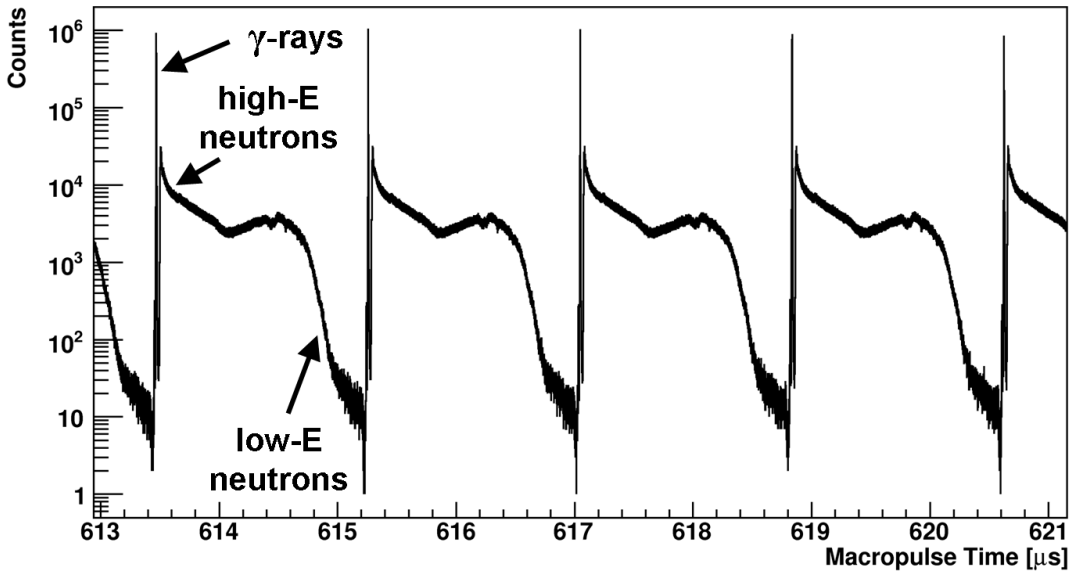

Figure 2.8: Portion of the time spectrum from the 2" neutron stopping detector. The macropulse time is the time between the beginning of the macropulse and the detection of the neutron. One can see the repetition of the TOF spectrum, once for each micropulse, and the large peak from the detection of γ-rays (gamma flash) near the beginning of each micropulse.

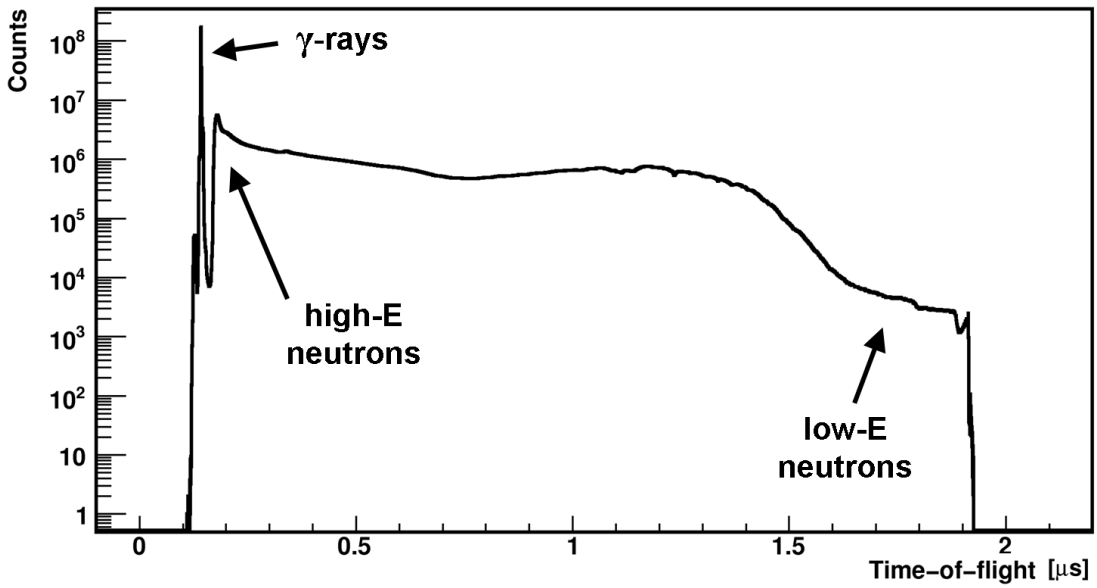

Figure 2.9: TOF spectrum of neutrons. The large peak near 145 *ns* is the gamma flash, and indicates the arrival at the detector of γ-rays produced when the proton beam hits the tungsten neutron-production target. High-energy (600 MeV) neutrons arrive at the detector at about 200 *ns*, and lower-energy neutrons arrive later (larger time-of-flight).

and the blank.

2.3.2 Time uncertainty

There are two sources of time uncertainty to consider: the precision of the time measurement of any given peak, and the offset of each macropulse relative to the digitizer clock. The former is an issue for each pulse while the latter must be determined only once for each macropulse.

Two procedures were used to improve the precision of the time of each peak. The first method employed a fit of each peak contained in a peaklet (see Figure 2.6). The fit used the convolution of a Maxwell-Boltzmann distribution with two exponential tails. The width of the distribution and the decay constants of the two tails were fixed by fitting whole pulses (Figure 2.10) from the fully recorded macropulses. The integral of the pulse was set for each pulse by a sum of the digitized samples (in the peaklet), with an additional factor to account for the part of the pulse not included in the 15 recorded samples (about 20%). The remaining free parameter, the peak time relative to the threshold crossing, was determined using a χ^2 minimization. An example of this fit for one peaklet is shown in Figure 2.6. The second method extracted the time from a running second derivative. The zero crossing of the second derivative (marking the leading-edge inflection point of the pulse) was used to define the peak time.

The macropulse offset was deduced by comparing the average TOF for photons in a macropulse with the expected photon TOF (142.2 *ns*). This was then used to shift all times in that macropulse. Figure 2.11 shows the effect of these corrections on the time resolution

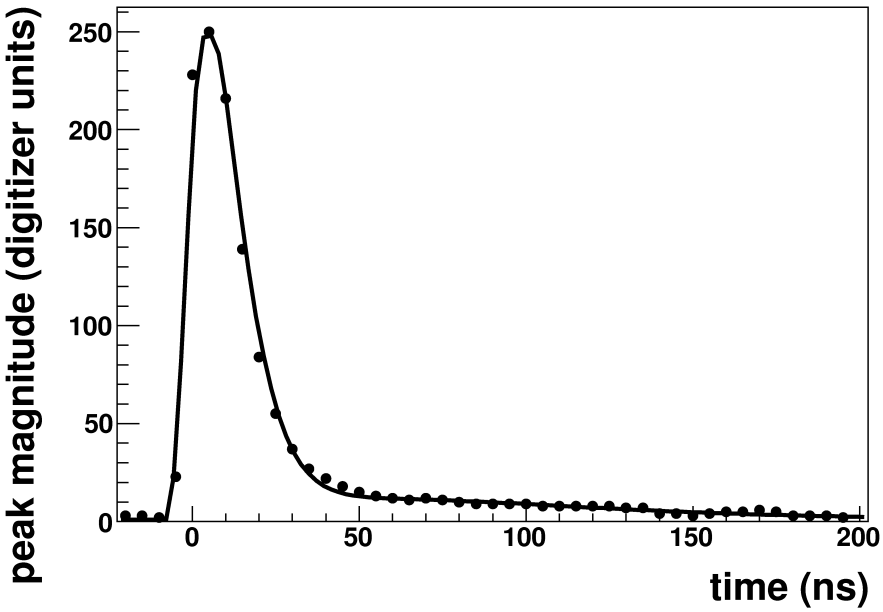

Figure 2.10: Example fit of the digitized PMT output for one whole pulse, obtained from analyzing whole waveforms. A Maxwellian distribution convoluted with two exponential tails was used as the line shape for fitting the detector pulses. The width and decay constants of the Maxwellian distribution were set using the largest pulses and including points out to very long times. The pulse rise time is slower than that of an individual PMT due both the finite sampling response of the digitizer and the fact that these signals are the result of adding two PMT signals together. This comment also applies to Figure 2.6.

of the γ-flash peak. With no correction for the offset and just using the threshold-crossing time for each peak, the time resolution was dominated by the sampling interval of 5 *ns* and resulted in a resolution (FWHM of the γ flash) of more than 5 *ns*. Fixing the macropulse offset and using the fitting procedure for each peak time improves the resolution, reducing the FWHM of the γ flash to 1.2 *ns*. Using the 2^{nd} derivative technique to fix the peak time (instead of fitting) reduces the FWHM of the γ flash to 0.89 *ns* ($\sigma = 0.38\,ns$).

Figure 2.12 shows the sensitivity of the time resolution to the number of γ-rays used to determine the offset. (This sensitivity is examined by randomly reducing the number of γ-rays used.) There were, on average, around 100 γ-rays available in each macropulse. However, much of the gain (from 5 *ns* to 1.2 *ns*) in resolution occurs with the use of just one γ-ray to determine the offset, and there is little improvement beyond about 25 γ-rays. Thus, the reduction in beam flux that would arise from using a smaller collimator would not significantly impact the time resolution. This determination is useful in evaluating how far this technique can be pushed to study smaller and smaller samples (see discussion in Section 2.7).

2.3.3 Pulse-height thresholds

The pulse height of the signals in the stopping detector is related to the energy deposited in the detector by the neutron. However, the incident neutron energy is not uniquely determined from energy deposited because there are several different reactions that can occur in the scintillator material (primarily neutron elastic scattering off hydrogen and carbon), each of which transfers differing amounts of energy to the scintillator. So, at each neutron

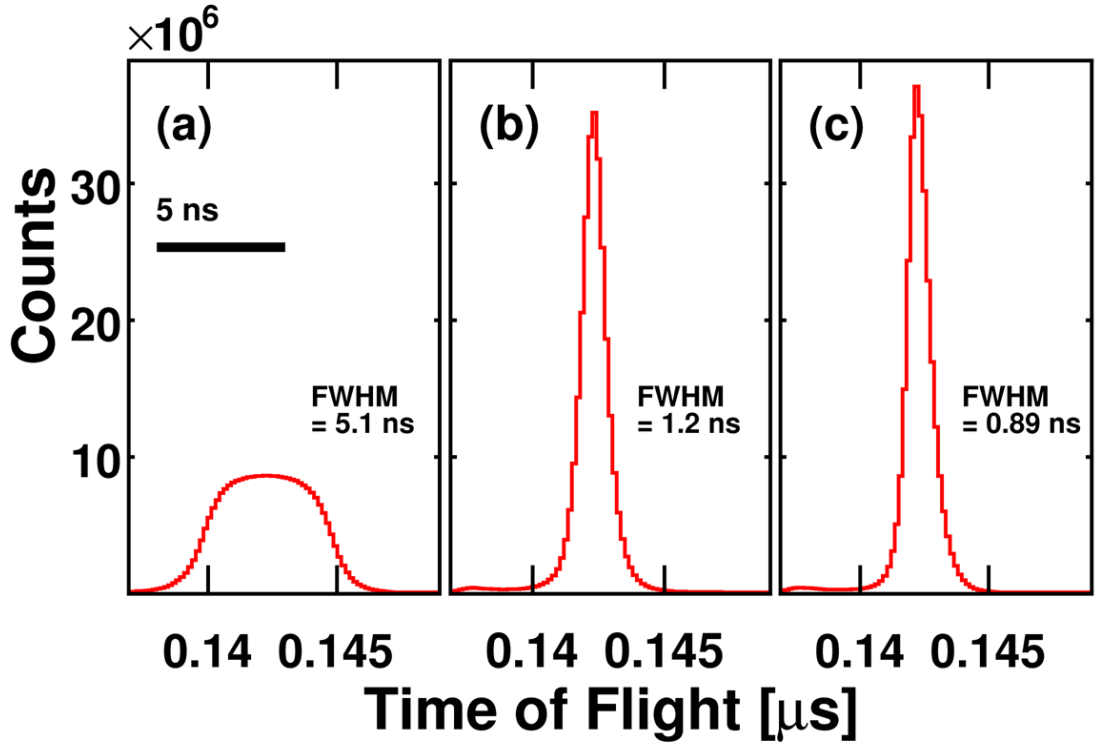

Figure 2.11: Time resolution of the γ-ray flash a) without and b) with fitting. The FWHM of the γ-ray flash was 5 *ns* before the fitting was carried out. This was reduced to 1.2 *ns* with fitting. As shown in panel c) the time resolution is improved slightly by utilizing the second derivative to determine the time of the pulses.

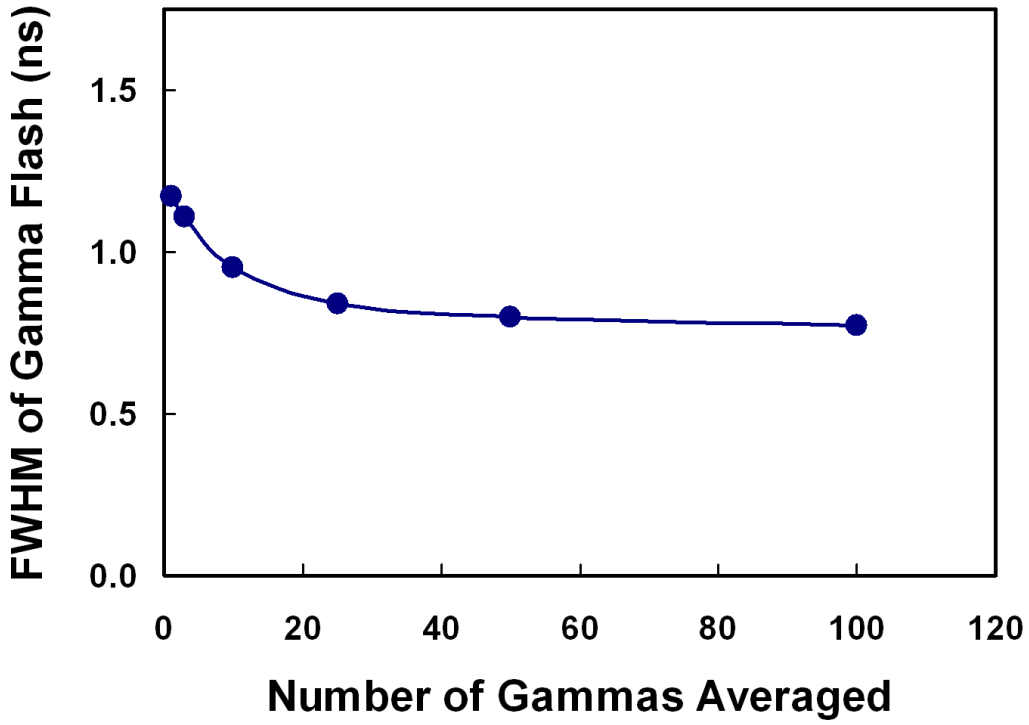

Figure 2.12: FWHM of the γ-ray flash as a function of number of γ-rays averaged for macropulse offset. The biggest gain (from 5 *ns* to 1.2 *ns*) is achieved with the first γ-ray, and the resolution of the γ-ray peak does not improve much beyond that obtained with about 25 γ rays. This analysis used the second derivative to determine peak times, as described in the text.

energy (or equivalently TOF), there is a distribution of pulse heights as shown in the plots of pulse height as a function of TOF and energy in Figures 2.13 and 2.14, respectively. Since these were negative polarity signals, increasing pulse height is toward the bottom of the figures.

Thresholds on the pulse height magnitudes were used, however, to exclude data in order to reduce the effect of noise and background. Both upper and lower software thresholds were placed on the magnitudes of the signal pulse heights. These gates were determined by examining the neutron total cross section of the samples as a function of pulse height. Since the cross section should be independent of pulse height for a given neutron energy, only the flat regions in such a plot should be included in the analysis. Thus a constant lower threshold of 150 mV was imposed on the magnitude of the pulse heights in raw data, along with an upper threshold that increased in magnitude linearly with energy. These thresholds are shown as dotted lines in Figure 2.14.

2.3.4 Dead-time correction

A Monte-Carlo (MC) simulation was written to determine dead-time corrections for neutron signals that were missed due to the simplicity of the peak-searching algorithm. The logic for the simulation was as follows. For each event, the waveform for a micropulse was constructed and then analyzed using the same algorithm and hardware threshold used in the experiment. This was done by picking the number of peaks in that micropulse using the experimental distribution for peaks per micropulse, then assigning times to each peak using the TOF spectrum. The pulse-height distribution at each time (or equivalently, energy)

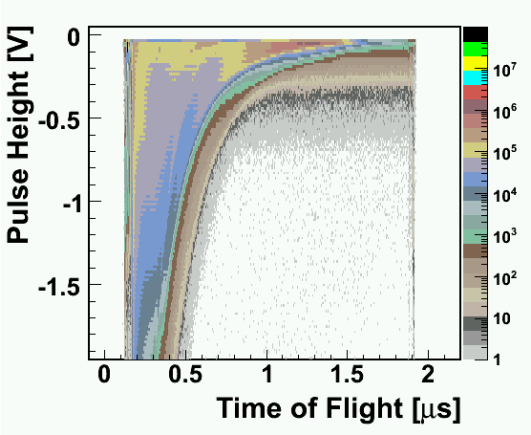

Figure 2.13: Pulse height of the signal in the stopping detector as a function of neutron TOF. For neutrons with a given TOF, there is a distribution of pulse heights (i.e. energy deposited in the detector). Since these were negative polarity signals, increasing pulse height magnitude is toward the bottom of the figures (more negative).

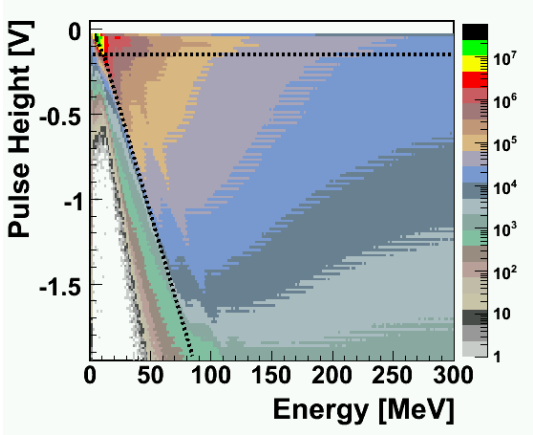

Figure 2.14: Same as Figure 2.14, except as a function of neutron energy. Dotted lines show upper and lower thresholds placed on pulse heights during data analysis, as described in the text.

and the lineshape determined from fitted experimental peaks gave the height and shape of the simulated peak. These peaks were then used to populate the waveform of a simulated micropulse.

However, rather than using this MC simulation, we realized that the dead-time corrections could more easily (and accurately) be obtained from the sample of raw waveforms. In other words, rather than simulating the waveforms, we could simply use the experimental ones.

The waveforms were analyzed using the hardware threshold set during the experiment. Each pulse that came before the signal from a previous pulse had dropped below the hardware threshold was considered "missed." Since there could be multiple overlapping pulses between threshold crossings, a fit similar to that previously used to obtain more precise timing was impractical. Instead, pulses were located using the zero crossing of the second derivative.

The fraction missed, as a function of energy, is shown in Figure 2.15 for the blank and one of the samples. There was an unexpected peak around 300 ns (about 100 MeV). The spectrum of missed pulses was projected out into pulse height, and around 300 *ns* an increase of missed pulses was seen at very low pulse heights. Examining coincidences with pulses in this region indicated that the anomalous pulses were likely reflections of the saturated signals from high-energy neutrons at the beginning of each micropulse. Since these reflections were below the software threshold placed on pulse-heights of the raw data, they would not affect the dead-time correction. When a matching pulse-height threshold was placed on the fraction-missed spectrum, the anomalous region was eliminated, as can

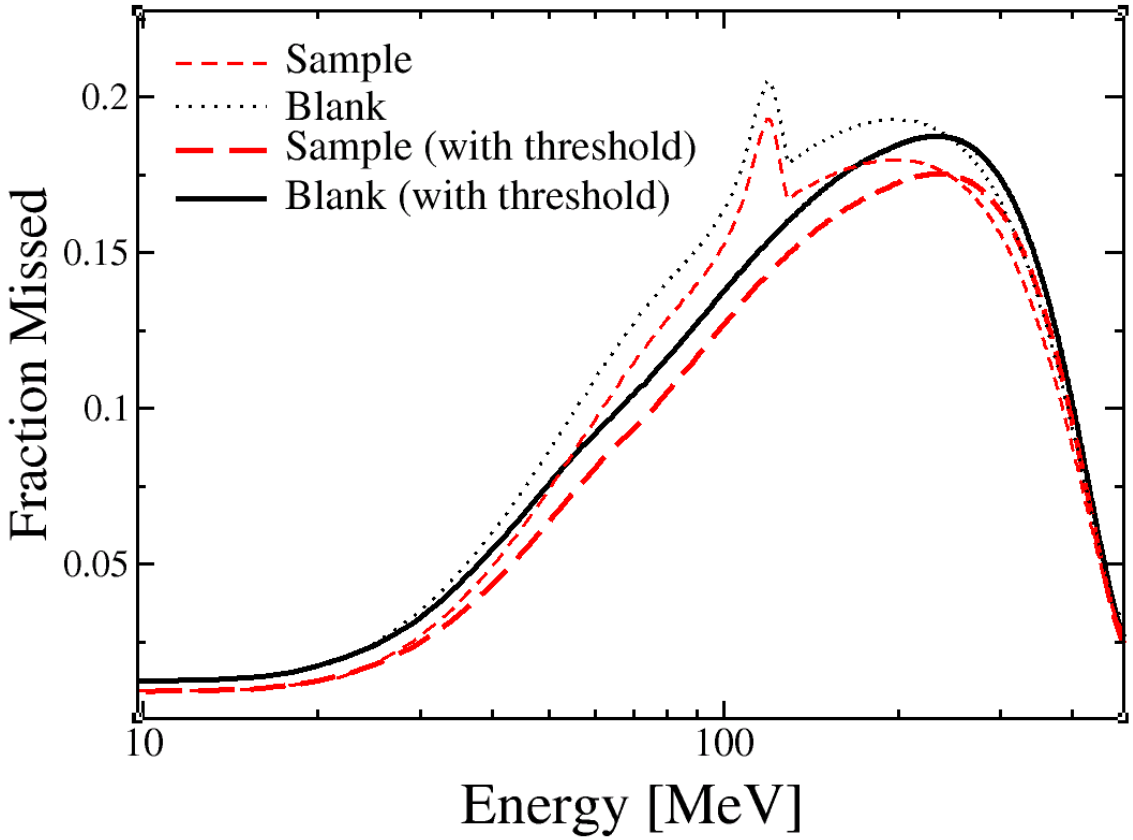

Figure 2.15: Fraction of neutrons missed by online peak-finding algorithm, as a function of energy, for the blank and one of the samples. Thicker curves labeled "with threshold" are calculated with a threshold placed on the pulse heights, as described in the text.

be seen in the curves labeled "with threshold" in Figure 2.15. A piecewise polynomial fit of this gated fraction-missed spectrum was used to correct the TOF spectra for each sample and the blank.

2.3.5 Sample oxidation

Since the ^{48}Ca sample had been prepared several months before this experiment, and used in two previous experiments in the intervening time, there was some oxide present on the sample, evident in a visual inspection. Immediately before the experiment, the mass of the sample had increased by 36 *mg* (1.3% by weight) from the initial pressing. This was assumed to be entirely due to oxidation. Since the beam was smaller than the sample diameter and parallel to the sample's cylindrical axis, any oxide present on surfaces other than the end caps of the sample would not affect our measurement. Lack of knowledge about the exact amount of oxygen seen by the beam led to a systematic uncertainty in the calcium cross section. Two extreme cases of oxide distribution were considered: an isotropic distribution of the oxide over the entire surface of the cylinder (in which case the 3/8"-diameter collimated neutron beam would see only 20% of the oxygen), and a distribution concentrated on the ends of the cylinder (in which case the beam would see 56% of the oxygen). The oxygen cross section from Reference [25] was then used to correct the observed ^{48}Ca cross section for each of these two cases. In addition, the ^{40}Ca cross section from this work was used to account for the 7% ^{40}Ca component of the ^{48}Ca sample. Oxygen contamination of the ^{nat}Ca sample was minimal, as it was prepared just before the start of the experiment.

2.4 Results

The total neutron cross section for ^{nat}C is shown in Figure 2.16a. The percent deviations from the published values of Abfalterer [20] are shown in Figure 2.16b for the dead-time corrected and the uncorrected data. Also included in this figure is a projection showing the variance in the difference between data sets. The solid line corresponds to the difference between our corrected data and the Abfalterer data, and the dotted line corresponds to the difference between the data for the two lengths of carbon measured in this work. There is good agreement between our (dead-time-corrected) data and the Abfalterer values, with a root-mean-squared (rms) deviation of 2.7%, however this deviation is largely systematic (see discussion in Section 2.7). There is excellent agreement between the cross sections for the two lengths of carbon measured in this work, with an rms deviation of only 0.85%, indicating the outstanding internal consistency, or precision, of the measurement.

The dead-time-corrected and uncorrected neutron total cross sections for ^{40}Ca are shown in Figure 2.17, along with the percent deviations from the values of Reference [20]. Figure 2.18 shows dead-time-corrected cross sections for both calcium samples along with the available literature data, which are scarce and limited to low energies for ^{48}Ca [20, 26, 27].

The relative cross-section difference between the two calcium isotopes ($R = \frac{\sigma_{48}-\sigma_{40}}{\sigma_{48}+\sigma_{40}}$) is shown in Figure 2.19 for the two extreme cases of oxide distribution discussed above. The uncertainty in oxide distribution has the effect of shifting the curve vertically, but not changing the shape. This systematic uncertainty is larger than the statistical uncertainties of the data.

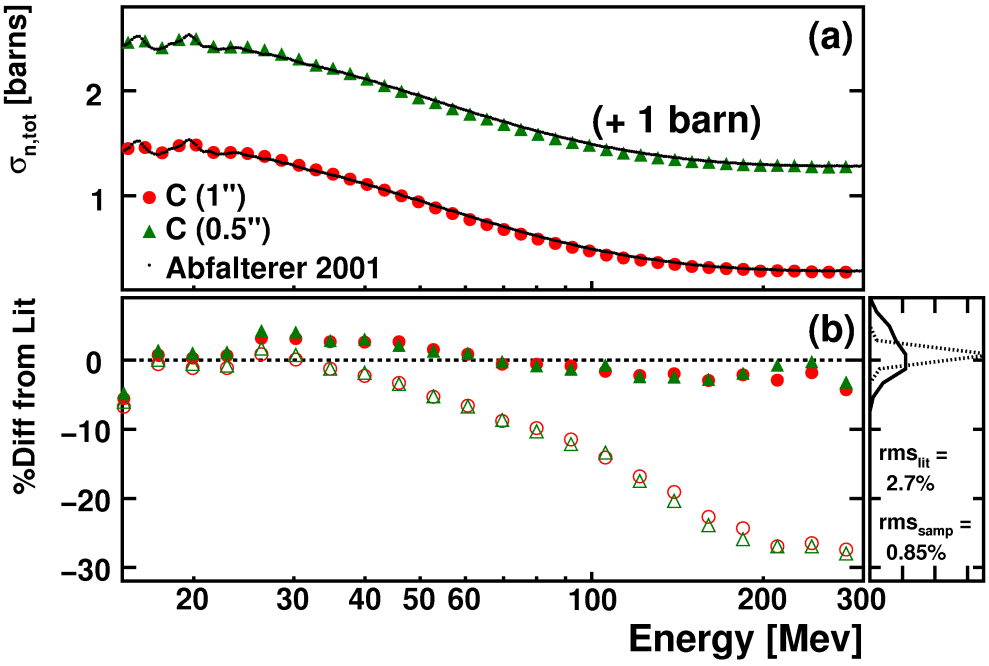

Figure 2.16: a) Total neutron cross section ($\sigma_{n,tot}$) for natural carbon. Red circles (1"-long sample) and green triangles (0.5"-long sample) show results of this work. Small black dots are literature data from Abfalterer et al. [20]. Statistical errors are smaller than the symbol size. For clarity, data for the 0.5"-long sample have been shifted up 1 *b*. b) Percent difference in cross sections between this work and the data of Abfalterer et al. Filled symbols include the dead-time correction extracted from the raw data (same symbols as above), and the corresponding open symbols are uncorrected. The plot on the right shows the variance in the difference between data sets - solid line corresponds to the difference between our corrected data and the Abfalterer data (root-mean-squared (rms) value of $rms_{lit} = 2.7\%$); dotted line corresponds to the difference between the data for the two lengths of carbon measured in this work ($rms_{samp} = 0.85\%$).

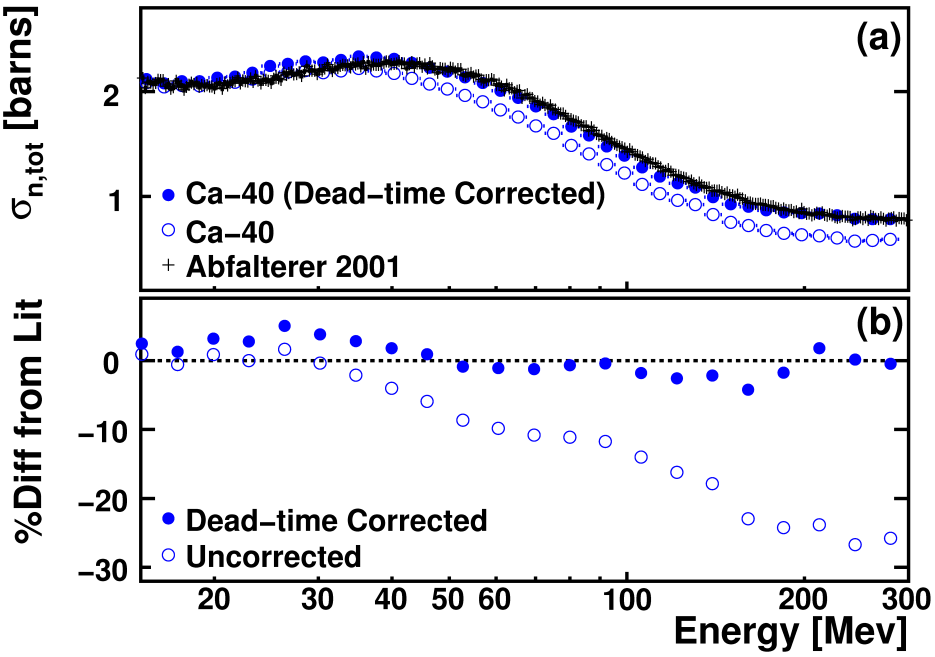

Figure 2.17: a) Total neutron cross section ($\sigma_{n,tot}$) for natural calcium. The results of this work are shown by the blue circles. Filled circles include simulated dead-time correction and open circles are uncorrected. Black crosses are data from Abfalterer et al. [20]. Statistical errors for this work are smaller than the symbol size. b) Percent difference in cross sections from this work as compared to Abfalterer et al. Same symbols as (a).

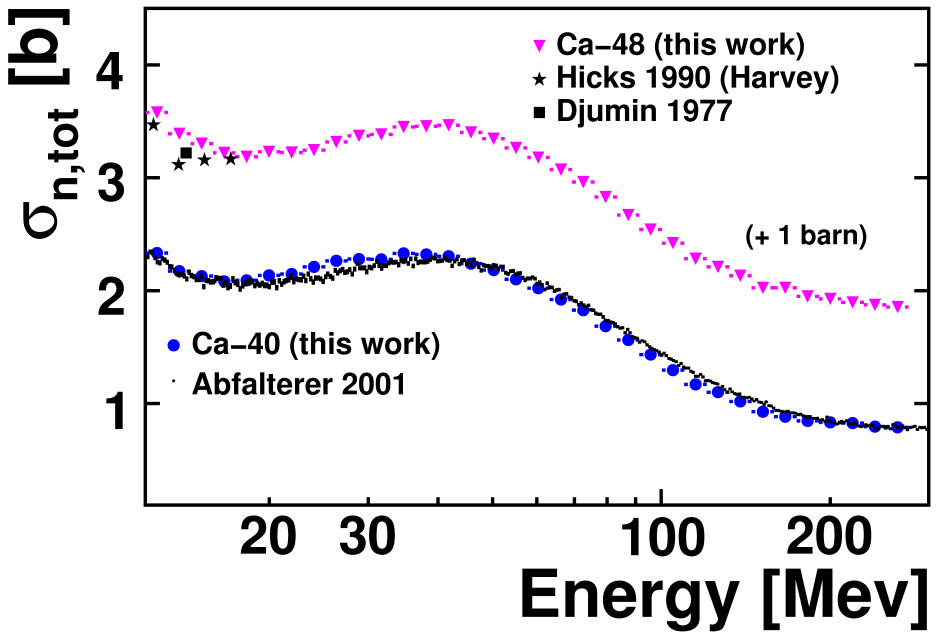

Figure 2.18: Total neutron cross sections ($\sigma_{n,tot}$) for ^{40}Ca and ^{48}Ca. The results of this work are shown by the pink triangles and blue circles. Black symbols are literature data [20, 26, 27]. Statistical errors for this work are smaller than the symbol size. For clarity, data for ^{48}Ca has been shifted up 1 *b*.

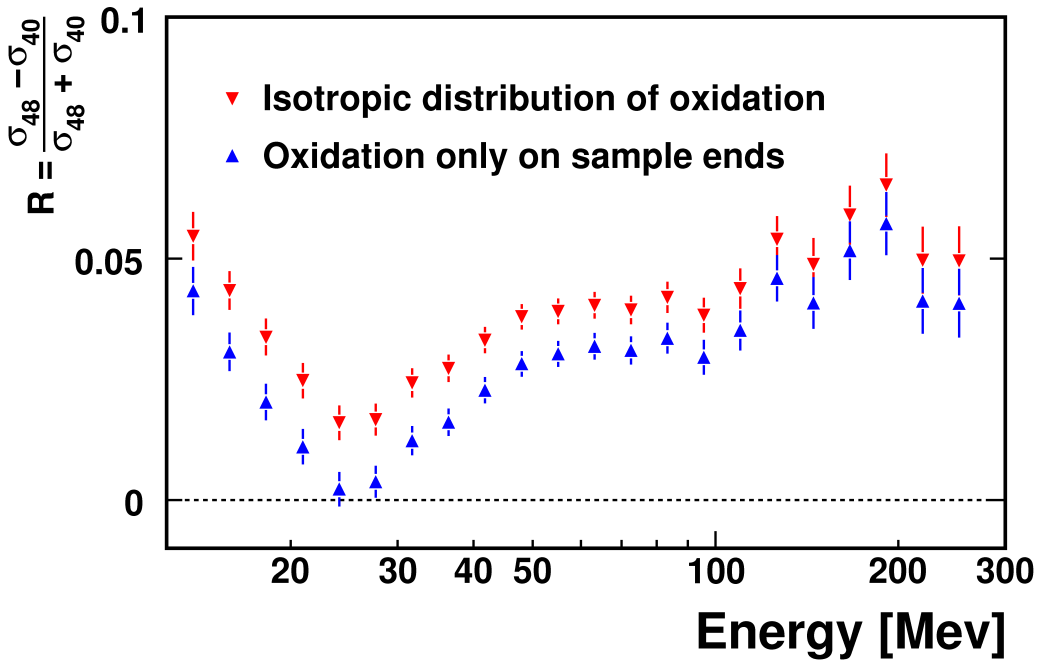

Figure 2.19: The relative total neutron cross-section difference, $R = \frac{\sigma_{48}-\sigma_{40}}{\sigma_{48}+\sigma_{40}}$, for two extreme possibilities of oxide distribution on the ^{48}Ca sample: concentrated on the end caps of the cylindrical sample (blue upward pointing triangles) or isotropically distributed over entire surface (red downward pointing triangles). Since the neutron beam travels through the axis of the cylindrical sample, any oxidation on the sides does not affect the extracted cross-section ratio. The uncertainty in oxide distribution has the effect of shifting the curve vertically, but not changing the shape.

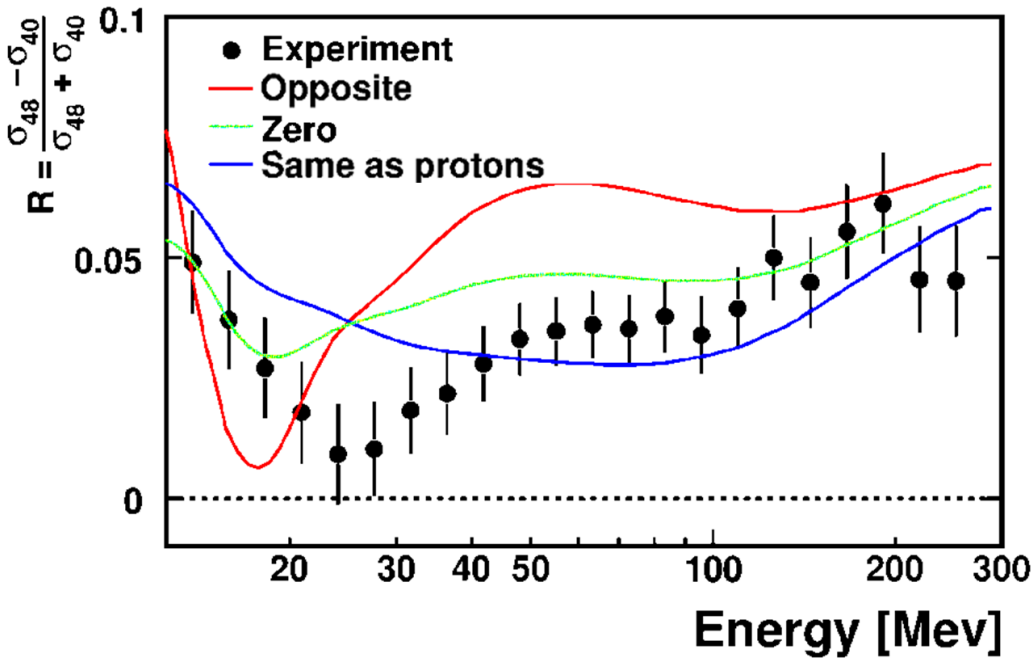

Figure 2.20: The relative total neutron cross-section difference, $R = \frac{\sigma_{48}-\sigma_{40}}{\sigma_{48}+\sigma_{40}}$. Error bars include the systematic uncertainty due to possible oxide distributions. Calculations are shown where the asymmetry dependence of the surface imaginary is the same as protons, is opposite to protons, and is zero (see [12]).

Figure 2.20 shows the relative cross-section difference between the two calcium isotopes, with error bars that include the systematic uncertainty due to oxidation. The three curves show DOM predictions based on three simple forms for the asymmetry dependence of the surface imaginary potential (W^{ur}) for neutrons [12]. The "same as protons" curve includes an asymmetry term in the surface imaginary potential for neutrons that goes as $+\frac{N-Z}{A}$, which is the form originally used for protons. The "opposite" curve includes a term

that goes as $-\frac{N-Z}{A}$, and the "zero" curve has no asymmetry dependence for W^{sur}. While none of these simple forms seems to capture the physics embodied by the experimental data, the true asymmetry dependence seems to lie somewhere between "zero" and "opposite to protons," evidenced particularly by the fact that R increases slightly in going from 30 to $100 MeV$.

A DOM fit to a large number of data sets, including the $\sigma_{tot}(n)$ ratio from this experiment, has been carried out by other members of our group [10], and is discussed in Section 2.5. The fitted curve for R from this analysis is shown in Figure 2.21. This fit does not explicitly constrain the form of the asymmetry dependence of W^{sur}, but instead allows its magnitude to be fit independently for each isotope and reaction. The results of this fit indicate that the magnitude of W^{sur} for neutrons is almost independent of the mass or asymmetry of the nuclide, for nuclei with $N \geq Z$ [10].

2.5 Incorporation of total cross section data into DOM

The measured neutron total cross section for ^{48}Ca was incorporated into an updated DOM analysis by other members of our group. The corresponding report [10] is not yet in print, so I will summarize a few points relevant to this discussion. Global fits were performed in four regions: I) Ca, Ni isotopes, N=28 isotones; II) N = 50 isotones; III) Sn isotopes; and IV) ^{208}Pb. The fits were constrained by elastic scattering measurements ($\sim$ 400 data sets), total and reaction cross sections, (e,e'p) data, and sp energies.

As already mentioned above, an explicit asymmetry term was not included in the optical

potentials, but the asymmetry dependence can be deduced by comparing the fit potentials for pairs of isotopes or isotones. The imaginary potentials obtained from this analysis for pairs of calcium and tin isotopes are shown in Figure 2.22. One can see that for the protons (solid red curves), the magnitude of the surface imaginary potential is larger in the more neutron-rich partner of each pair (i.e. ^{48}Ca and ^{124}Sn). For the neutrons, however, the magnitude of the surface imaginary potentials is practically the same for both isotopes in the pair.

To see what the difference (or lack of) in the surface imaginary potentials implies about spectroscopic strength and nuclear correlations, one can compare the magnitude of the surface imaginary potentials W_{max}^{sur} for tin isotopes (shown in Figure 2.23) to the extracted spectroscopic factors (Figure 2.24). The increase in W_{max}^{sur} for protons results in a slight decrease in the SF, which is interpreted as a slight increase in the strength of correlations for protons. For neutrons there is little change in either W_{max}^{sur} or the SF across the chain of isotopes, implying very little variation in the strength of correlations for neutrons with increasing neutron content in these neutron-rich, but stable, isotopes.

2.6 Comparison to the conventional technique

2.6.1 Summary of conventional (analog) technique

The conventional method of measuring $\sigma_{tot}(n)$ uses standard time-of-flight (TOF) techniques, and is described in Refs. [25] and [20]. Briefly, a logic signal (T_0) from the machine RF (which is of course synchronized with the proton beam itself) defines a looking

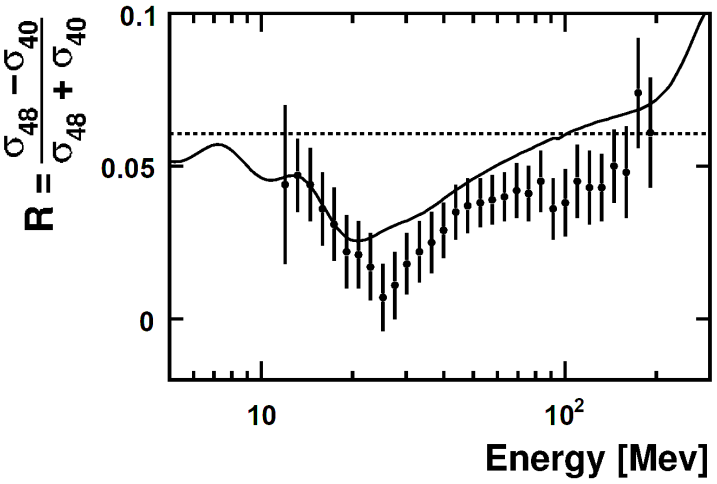

Figure 2.21: The relative total neutron cross-section difference, $R = \frac{\sigma_{48}-\sigma_{40}}{\sigma_{48}+\sigma_{40}}$. Error bars include the systematic uncertainty due to possible oxide distributions. Curve shows DOM fit to the data points as described in [10].

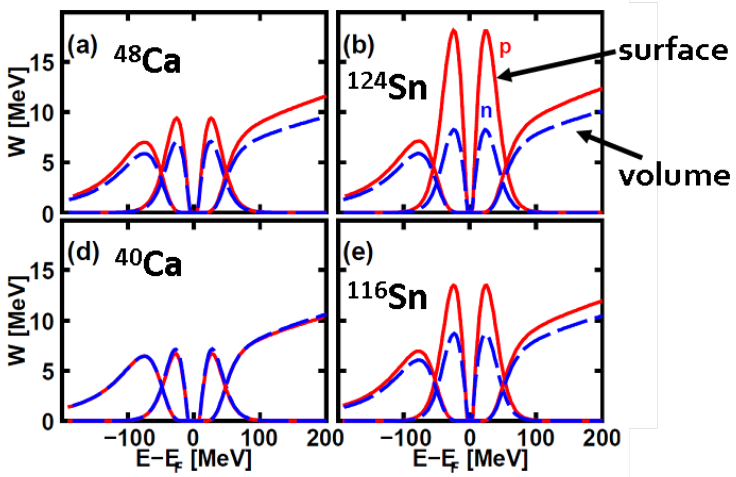

Figure 2.22: Surface and volume imaginary potentials, as a function of the energy difference from the Fermi energy, for pairs of calcium and tin isotopes. Proton potentials are shown as solid red curves, and neutron potentials are dashed blue curves. Taken from Reference [10]

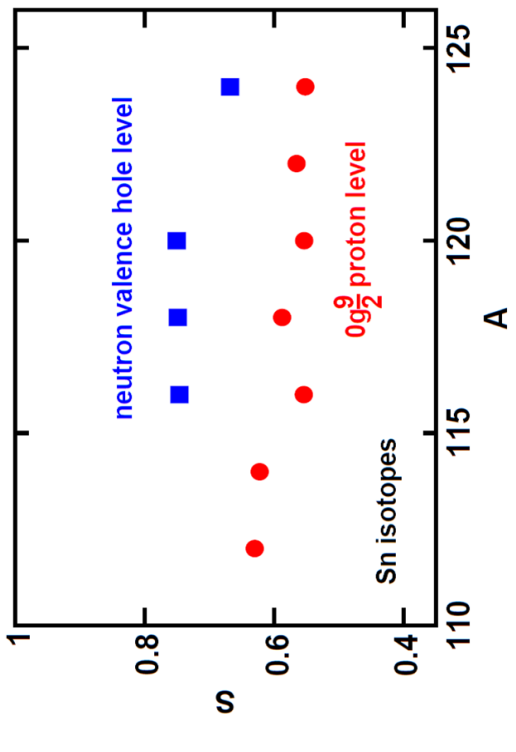

Figure 2.24: Proton (red circles) and neutron (blue squares) spectroscopic factors S for tin isotopes. Taken from Reference [10].

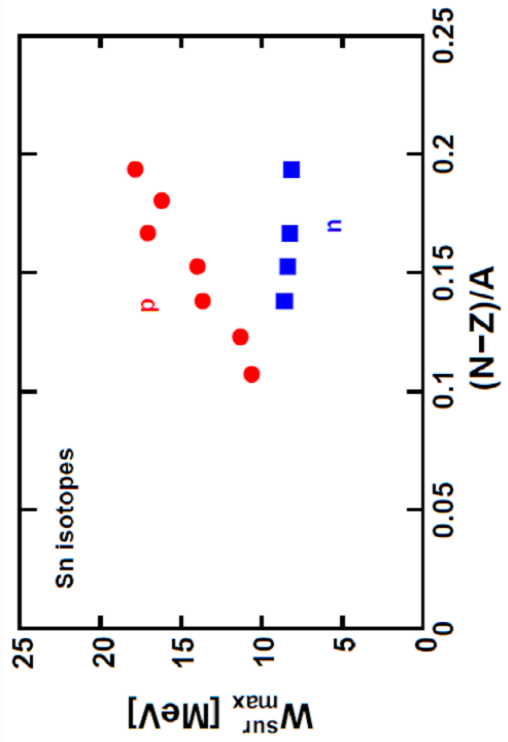

Figure 2.23: Magnitude of the proton (red circles) and neutron (blue squares) surface imaginary potentials for tin isotopes, as a function of asymmetry. Taken from Reference [10].

window for each micropulse. If the acquisition system is not busy at the beginning of this window, it can accept a *start* signal from the downstream neutron detector during the window. The *stop* is then provided by a delayed copy of T_0. Only the first *start* in a given window (micropulse) is taken.

This method suffers from large dead-time losses, which are summarized in the next section. These losses make it necessary to have large samples (which can be expensive for rare isotopes) or to utilize extended beam time (which can be difficult to obtain).

2.6.2 Dead-time contributions

The dead-time corrections can be divided into two types - an analytic correction which takes into account that low-energy neutrons are less likely to be counted, and a live-time correction to account for micropulses that are missed while the acquisition is busy.

2.6.2.1 Analytic correction

The analytic correction [24] arises because only the first *start* in a micropulse is taken, so at most one neutron per micropulse can be measured. The first detected particle in each micropulse effectively blocks any further particles from that micropulse from being counted. This effect is energy dependent - low-energy neutrons are more likely to be missed since they arrive later in the micropulse. If there are two neutrons in the same micropulse, it is always the higher energy one that is counted (because it arrives first), and the lower-energy one that is missed. In contrast, our digital technique can, in principle, record all of the neutron times in a micropulse. In practice this is limited by the ability of the peak-

detection algorithm to distinguish two very closely spaced pulses, as described in Section 2.2.2. However, the fraction missed is far smaller, since even a simple algorithm has the ability to easily distinguish many peaks in a micropulse.

While the corrections arising from missed neutron signals with the digital technique, as described in Section 2.3.4, were fairly substantial (at high energy), they were still smaller in magnitude than those typically needed for the standard event-by-event analog technique [24], which can underestimate the neutron count by up to 80% for sample-out measurements, and 50% for sample-in measurements. In addition, the corrections for our DSP technique would be even smaller if one follows the suggestions discussed below in Section 2.7.

2.6.2.2 Acquisition and computer live time

The second correction accounts for the fact that micropulses will be missed entirely if the data-acquisition system is not ready when the event arrives. This can be corrected for by keeping track of the total number of micropulses (number of T_0's) and the number of events that are taken (number of live T_0's, minus any vetoed). After applying the analytic dead-time correction, the resulting TOF spectra are divided by the fraction of time that the system is live $\left(\frac{N_{T_0}}{N_{T_0,live}-N_{veto}}\right)$ to obtain the true spectra [20].

Conventional data-acquisition systems can require several 10's of μs to transfer data to the computer, meaning that many micropulses would be missed before the system was ready again. Recent studies avoid this proble m by taking advantage of the fact that the samples are cycled through the beam at intervals on the order of 20 seconds. The data

(flight times) for a sample are stored in a histogramming memory module and transferred to the computer while the sample is being changed. With this workaround, the live-time fraction typically varies between 0.55 and 0.91 for the conventional electronics set up [25].

The digital technique goes a step further, and does no processing whatsoever on the waveforms during the macropulse. Instead, they are collected in the digitizer-board buffer and not transferred to the computer to be processed until the macropulse ends. Thus there are no dead-time losses at all associated with transfer and processing - as long as this transfer is completed before the next macropulse arrives.

2.6.3 Sample size

The dead-time considerations discussed above significantly limit the amount of data that can be collected in the conventional way. In order to achieve small statistical errors, one would need to have large samples or long counting times. As an example, the aluminum target used to measure $\sigma_{tot}(n)$ in a previous study [25] needed to be 20 cm long (areal density $nl = 1.2 atoms/b$, which is about $6 mol$ for a cylindrical sample with a diameter of $2 cm$), to get $1-2\%$ statistical errors over the energy range 5-540 MeV with a counting time of a few days. This length could be halved if one required 1% statistical errors only below $100 MeV$, however one still needs a significant fraction of a mole or more of isotopically pure material in order to perform the measurement in a reasonable amount of time.

When measuring $\sigma_{tot}(n)$ on rare isotopes, the problem becomes one of obtaining large enough samples of highly enriched target material. If it is possible to obtain the material, it is likely to be very expensive. In recent studies at LANSCE, sample sizes were typically

in the range $0.5-6\,mol$ [25, 20, 14]. In contrast, the digital technique allowed us to obtain 1% statistical errors in about a day of counting time, using a sample that was only 0.056 of a mole (about 10 times less than would typically be needed for the conventional method). Furthermore, the digital technique is well-suited to even smaller samples, as discussed discussed below in Section 2.7. Table 2.3 shows our highest priority targets for $\sigma_{tot}(n)$ measurements and the estimated cost for a $3/8$" diameter target with the same areal density as the ^{48}Ca used in this experiment.

2.7 Discussion

The total neutron cross section for ^{48}Ca has been measured over a large energy domain, using a digital-signal-processing technique. A compromise strategy was employed that skirts the need for massive front-end computational power working in real time and makes optimal use of the beam-pulse structure at LANSCE. By using a simple algorithm to locate peaks, and storing small regions around each peak (peaklets) plus a tiny fraction of the full waveforms, were able to work within the computer limitations. Although analysis of just the peaklets misses some pulses, the sampling of the full waveform could be used to generate the required correction.

This compromise generates data with high statistical significance and, with correction, reproduced known cross sections with an rms deviation of 2.7% (carbon) and 2.9% (calcium) for energies between 15 and 300 MeV. This deviation is systematic, with our values exceeding the literature values around 30 MeV and being less around 100 MeV. This

Table 2.3: Highest priority Ni, Sn and $N = 28$, 50 targets for $\sigma_{tot}(n)$ measurements. The last column shows the estimated price for a 3/8" diameter sample with the same areal density as the ^{48}Ca sample used in this work (which had $1/nl = 35$), based on quotes from Trace Sciences. If the isotope is not available in elemental form, the type of compound used for the price estimate is also listed.

Target (% abundance)	Enrichment (%)	Form (if not elemental)	Price ($)
^{Nat}Ni	99		<10
^{58}Ni (68.3)	99		1400
^{60}Ni (26.1)	99		3000
^{64}Ni (0.91)	95		42000
^{Nat}Sn	99		<10
^{112}Sn (0.97)	95		22500
^{124}Sn (5.79)	97		5200
^{48}Ca (0.19)	97	oxide	115000
^{50}Ti (5.4)	90	oxide	45000
^{52}Cr (83.8)	99		3500
^{54}Fe (5.9)	99		7100
^{88}Sr (82.6)	99	carbonate	3000
^{92}Mo (14.8)	92		11000

small difference could be empirically corrected for (by using, for example, the C literature cross sections), however we are not sure where the error lies or even which measurement method (ours or the standard analog method) contains the error. Furthermore, this difference cancels in isotopic ratios, and is sufficiently small so that its impact (on optical-model parameters) is negligible. The internal systematic uncertainty of our method is perhaps better measured by the difference in the cross sections between the two lengths of carbon. This rms deviation was only 0.85%.

The dead-time-like correction discussed above is proportional to the raw rate of neutrons. Since the peaklet statistics leads to an insignificant contribution to the error (0.6-1.0%), reducing the neutron flux would lead to a smaller correction with little degradation of the statistical significance of the cross sections. This means that superior results could have been obtained with, for example, a ¼"-diameter collimator. Such a collimator would have allowed our sample size to be reduced by almost a factor of 2 (to $3/8$" diameter) while retaining the areal density of the targets.

In addition, the LANSCE facility will soon be running at 120 Hz (rather than 60 Hz). Although the setup described here can only handle a rate of 60 Hz, if one used two acquisition systems running in parallel (each digitizing and analyzing macropulses at 60 Hz), this would allow twice as much data to be collected with no change in the acquisition logic.

The relative difference between the total neutron cross sections of ^{48}Ca and ^{40}Ca measured in this work has been incorporated into a DOM analysis (described in Section 2.5), and is consistent with a surface imaginary potential for neutrons whose magnitude remains almost constant as the nuclei become more neutron-rich. The technique developed in this

work makes feasible a program for the determination of $\sigma_{tot}(n)$, over a broad intermediate-energy region, for rare stable isotopes throughout the chart of the nuclides.

Chapter 3

Proton and neutron knockout from ^{36}Ca

3.1 Background

While the occupancies of independent single-particle (sp) orbits or the spectroscopic strength of these orbits at discrete energies are not direct experimental observables [28, 29], they are quantities with a clear, almost model-independent, interpretation as long as the strength in question is close to the Fermi surface [1]. Plausible reaction models coupled with structure calculations can provide estimates of nucleon knockout cross sections. If experimental cross sections were to be reproduced, support would then be found for both models. When experimental cross sections are not reproduced, as is found for knockout from deeply-bound states, both the reaction model and structure calculations must be questioned.

For example, when considering electron-induced knockout reactions, i.e. $(e,e'p)$, on beta-stable nuclei, one finds that the distorted wave impulse approximation (DWIA), coupled with a Green's function approach to structure calculations, can accurately reproduce

the experimental cross sections, lending credence to both the reaction model and the structure model [1]. These reactions have shown that for beta-stable nuclei, there is universally a roughly 35% reduction in spectroscopic strength relative to independent-particle model (IPM) values [1].

Similarly, it is thought that eikonal models of hadron-induced nucleon-knockout reactions at intermediate energy can be used to extract spectroscopic strength, and coupled with SM spectroscopic factors to estimate the knockout cross section. Consistency with (e,e'p) results for beta-stable nuclei has encouraged an effort in the last decade to extend this type of knockout analysis to radioactive nuclei in order to understand how spectroscopic strength changes off beta stability [30]. Confidence in the reaction model and the mindset that the SM overestimates the localized spectroscopic strength has lead to the introduction of the reduction factor, $R_s = \frac{S_{deduced}}{S_{SM}}$, which quantifies the difference between the SM spectroscopic factors (S_{SM}) and those deduced from the experimental data with input from the reaction model ($S_{deduced}$).

Studies of hadron-induced knockout reactions have indicated that there is a strong trend in the strength of nuclear correlations with separation energy - stronger correlations are felt by more deeply bound particles (both protons and neutrons), as evidenced by removal cross sections that are much smaller than calculated by theory and lead to very small (i.e. $<< 1$) reduction factors [6]. The reduction in spectroscopic strength deduced for the most deeply bound orbitals is quite significant - reduction factors as low as 0.24 (corresponding to a SF that is only 16% of the IPM value) are obtained [16].

Another way to study these correlations is using the dispersive optical model (DOM)

described in Chapter 1, in which the optical potential is constrained by data from elastic scattering at positive energies and from electron-induced nucleon-removal reactions at negative energies. A DOM analysis of calcium isotopes [12] indicates that the asymmetry dependence of proton correlations is such that stronger correlations are experienced in the neutron-rich nucleus ^{48}Ca than in the symmetric nucleus ^{40}Ca. Since the separation energy is a measure of the neutron-proton asymmetry, this qualitative trend in the strength of correlations is consistent with that seen in the analysis of proton-knockout data, however the magnitude of the trend seen in DOM results is considerably weaker.

The strong trend in the strength of correlations for neutrons has also been called into question. Recent results for neutron transfer to argon isotopes [7], as well as a global analysis of previous neutron-transfer data [31], lead to the conclusion that the strength of correlations felt by neutrons in a neutron-rich nucleus changes little to none with increasing neutron number.

It is clear that there is a contradiction between the conclusions drawn from hadron-induced knockout and those drawn from transfer reactions and the DOM. The goal of this work was to investigate which interpretation of the experimental results is best supported and perhaps shed light on where the other(s) go wrong.

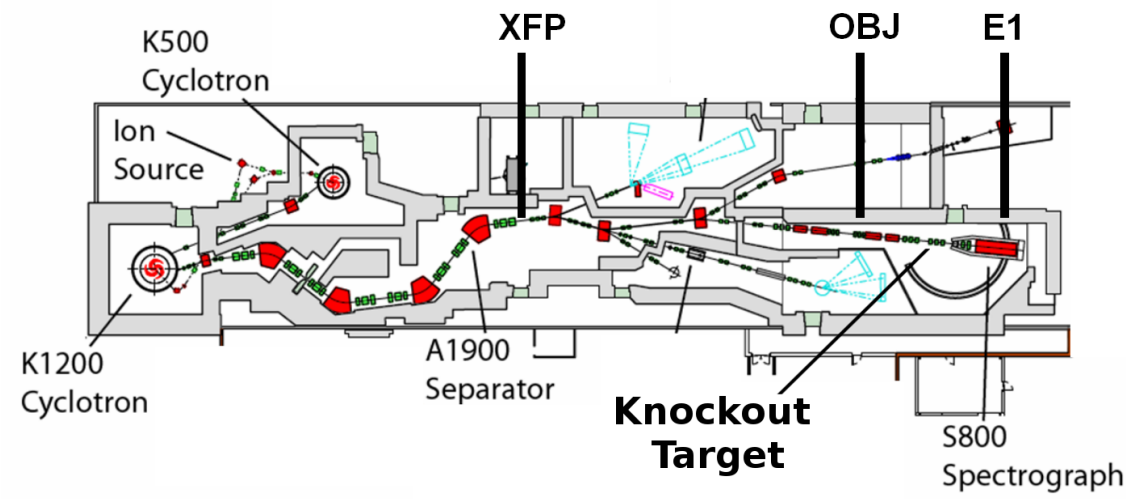

Figure 3.1: Schematic of the NSCL facility. The approximate locations of the knockout target and the timing scintillators in the extended focal plane of the A1900 (XFP), the object plane of the S800 (OBJ) and the focal plane of the S800 (E1) are labeled.

3.2 Experimental details

3.2.1 Beam and detectors

A nucleon-knockout experiment was performed at the National Superconducting Cyclotron Laboratory (NSCL) on the campus of Michigan State University. A schematic of the facility is shown in Figure 3.1.

The proton-rich nucleus ^{36}Ca ($t_{1/2} = 102\,ms$) was produced by fragmenting a primary beam of 140 MeV/nucleon ^{40}Ca on a 658 mg/cm^2 beryllium target, located at the target position of the A1900 fragment separator [32]. The fragmentation products were first filtered to select a single magnetic rigidity $B\rho = \frac{mv}{q}$. The beam then passed through a 300 mg/cm^2

thick energy-degrading aluminum wedge, each particle losing an amount of energy related to its atomic number. A second selection based on the reduced magnetic rigidity after the wedge provided separation, yielding a cocktail beam of $N = 16$ isotones, with energies of about 70 MeV/nucleon. The ^{36}Ca purity was 8%. Other beam constituents included ^{35}K, ^{34}Ar, ^{33}Cl, and ^{32}S. This cocktail was delivered to a 188mg/cm^2 thick ^{9}Be foil which used for the knockout reaction and was located at the target position of the S800 Spectrograph [33].

The gamma-ray spectrometer CAESAR (CAESium iodide ARray) [34], shown in Figure 3.2, was placed around the knockout target position of the S800 to observe the decay of any excited states formed in the knockout reaction. This array consists of 192 CsI(Na) rectangular crystals of two types, laid out as shown in Figure 3.3. There are 144 with dimension 2"x2"x4", and 48 with dimension 3"x3"x3". The intrinsic energy resolution is 8% at 662 keV, and the in-beam resolution is <10% above 1 MeV. The array has a detection efficiency of about 30% at 1 MeV.

Knockout residues were identified and tracked through the S800 on an event-by-event basis. Two position-sensitive Cathode-Readout Drift Chambers (CRDCs) measured the residue position in the S800 focal plane, and an ionization chamber (IC) measured energy loss [35].

3.2.2 Particle identification

Particle identification (PID) is done in two steps: one must first identify the incoming particle, and then one can look at the residues coming from reactions involving that incoming

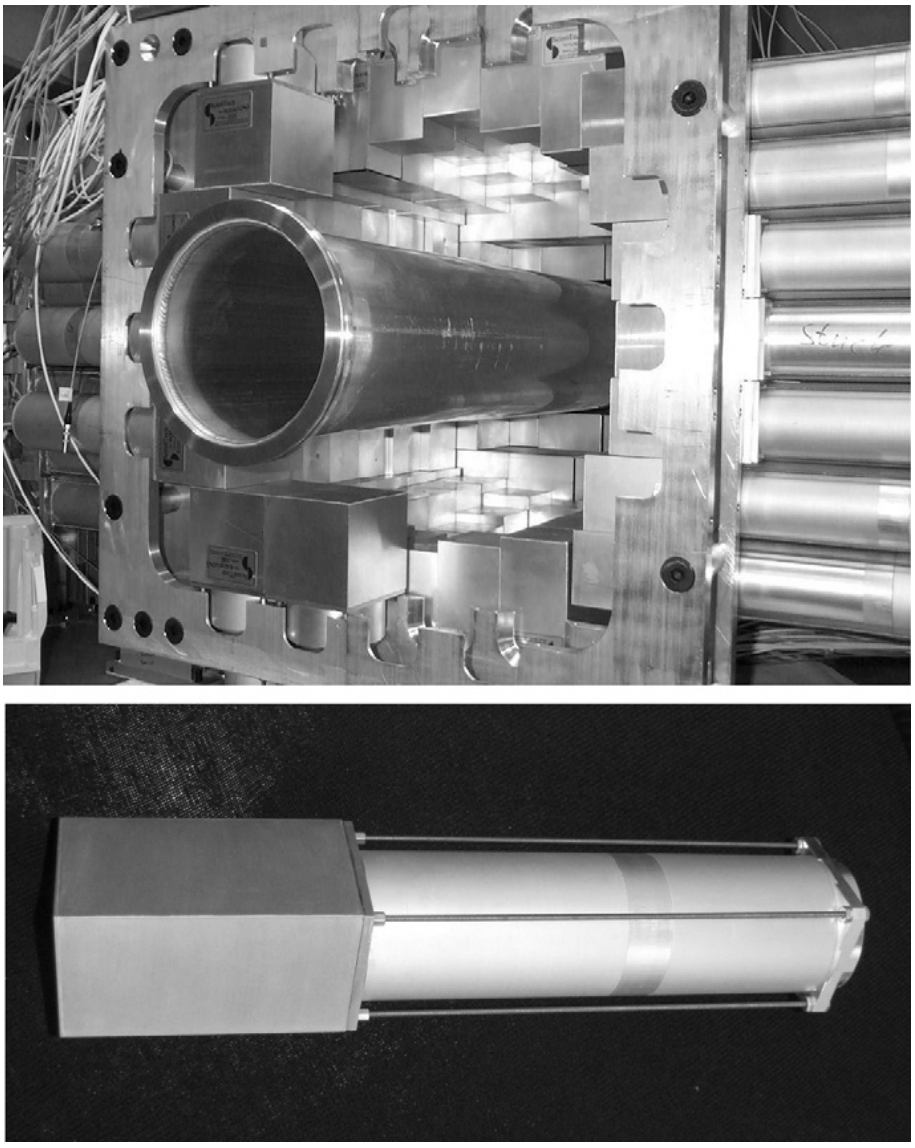

Figure 3.2: (top) Photograph of CAESAR set up in front of the S800, with several upstream detectors removed to allow view inside. (bottom) One of the 2"x2"x4" detectors. Taken from Reference [34].

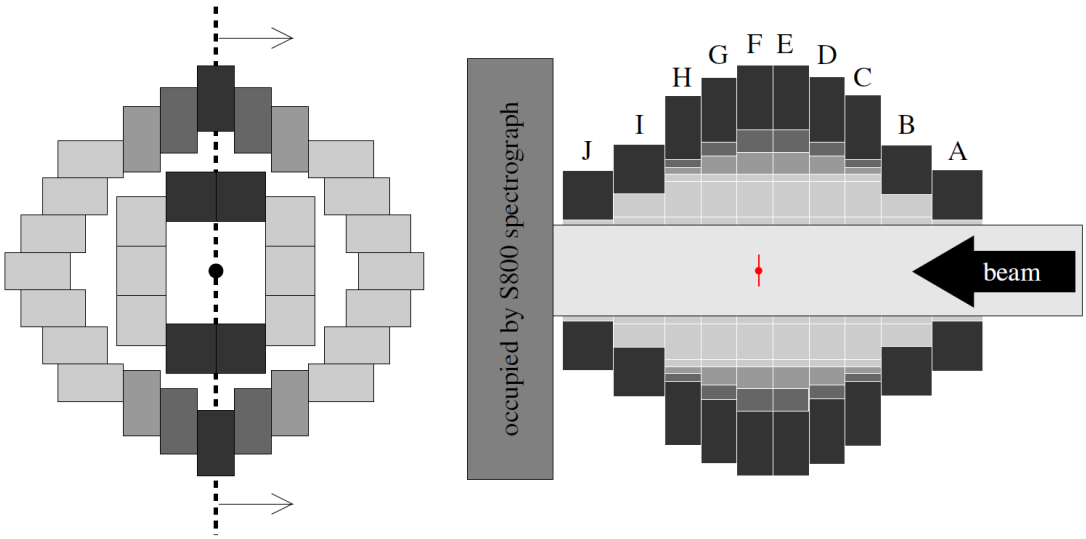

Figure 3.3: Layout of the CAESAR CsI(Na) detectors: (left) cross-sectional view perpendicular to beam axis showing rings J and F and (right) cross-sectional view parallel to beam axis showing all ten rings and target position (dot with vertical line through it). Taken from Reference [34].

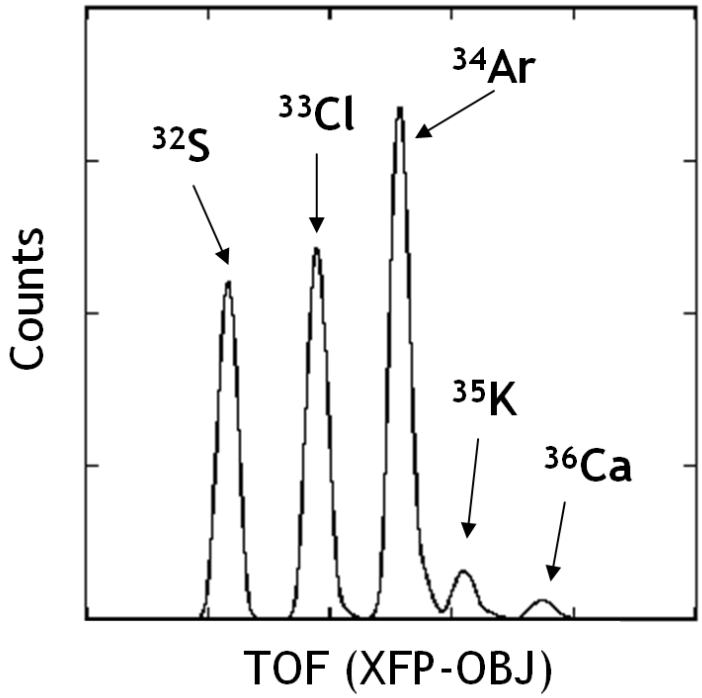

Figure 3.4: Plot of time-of-flight between OBJ and XFP scintillators, showing the separation of isotones. Note that the time scale runs backwards so that time (of flight) increases to the left.

particle.

The physical basis of isotone separation is the differing ion time-of-flight (TOF) between a scintillator in the extended focal plane (XFP) of the A1900 and one in the object plane (OBJ) of the S800. The ions (which are fully stripped of electrons, so that $q = Z$) have fixed rigidity $\frac{mv}{q}$. Thus the velocity increases with increasing Z, and the TOF decreases. The separation of isotones can be seen in the 1-D plot of the XFP-OBJ time shown in Figure 3.4. This time-of-flight XFP-OBJ is actually the difference between two times

measured relative to a common start (the E1 scintillator in the focal plane of the S800). Note that time runs backwards in this and the following plots, so that larger TOF is to the left and bottom of the plots.

Improved isotone separation can be achieved by plotting the two base times (XFP-E1 and OBJ-E1) against one another, as shown in Figure 3.5a. The 1-D difference plot corresponds to projections onto a diagonal of this plot, such as that indicated by the dotted line. In this 2-D map, each isotone is represented by a locus of points stretched perpendicularly to that diagonal. This stretching is due to each isotone having a distribution of flight paths in the S800 (going from OBJ to E1), resulting from different positions at the target and scattering in the target. A gate can be drawn in the 2-D map in Figure 3.5a around one particular incoming nuclide, allowing us to look only at reactions involving that nuclide in the incoming channel.

Outgoing reaction residues are identified in a TOF-dE map, which is a 2-D plot of the TOF between OBJ and E1 scintillators (corrected for different flight paths in the S800) versus the energy loss (dE) in the S800 IC detector. An example of this is shown in Figure 3.5b, which has been gated on incoming ^{36}Ca. Each locus of points in the figure corresponds to a different reaction residue. Lines of isotopes (solid arrow) and isotones (dashed arrow) are indicated in the figure. Identifying just one nucleus (for example the most intense spot, which is the unreacted beam) allows one to identify all the others as well.

The complete reaction identification consists of a gate on the incoming particle in the 2-D OBJ-XFP map (Figure 3.5a), and a gate on the reaction residue in the TOF-dE map (Figure 3.5b). The PID can be confirmed for nuclides with known gamma-ray spectra

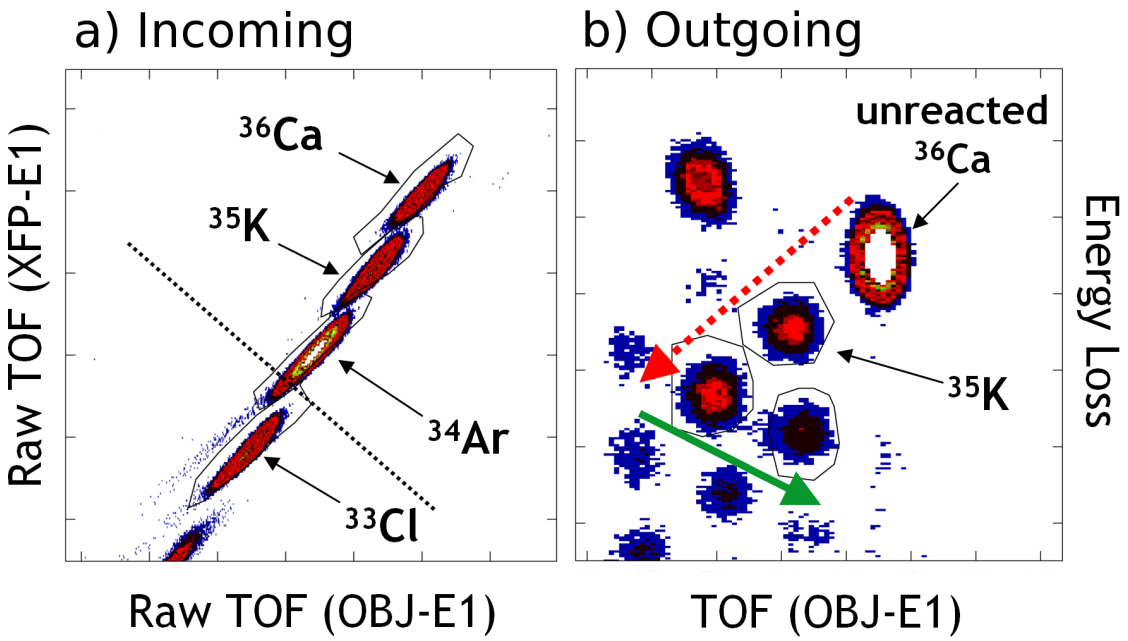

Figure 3.5: Plots used to select a particular reaction channel (incoming-outgoing particles). Note that all time scales run backwards - time (of flight) increases downwards and to the left. (a) Plot of time-of-flight to OBJ scintillator vs. time-of-flight to XFP scintillator (relative to a common start at E1). Separation of isotones is achieved and the plot can be used to identify, and gate on, *incoming* particles. (b) Example plot of time-of-flight versus energy loss used to identify *outgoing* reaction residues. This plot is the result of gating on incoming ^{36}Ca, with beam settings optimized for proton knockout residues. The dashed red arrow indicates a line of isotones (removal of protons), and the solid green arrow indicates isotopes (removal of neutrons).

by using these gates to select CAESAR data for a particular nuclide and comparing the observed spectrum to the expected spectrum for that nucleus.

3.3 Reaction model

The spectroscopic factor (defined in Equation 1.2.1) is not an experimental observable, but is deduced from particle-removal reactions with the help of an appropriate reaction model. To extract a spectroscopic factor (SF) from the experimental cross section to a given physical state, it is necessary to calculate single-particle (sp) cross sections for each contributing sp state. When there is only one contribution (as in the reactions studied here, for which there is only one bound state in the residue), the deduced experimental SF (including the $2j+1$ factor) is simply the ratio of the experimental cross section to the sp cross section, $C^2S_{deduced} = \frac{\sigma_{exp}}{\sigma_{sp}}$. The ratio of this deduced SF to that calculated with the shell-model is the reduction factor R_s.

One set of sp cross sections used in this analysis were calculated using the reaction code of Tostevin, based on the eikonal approach [36]. Variations on this approach were carried out using the reaction code MOMDIS [37]. The results of these variations are shown in Table 3.1, and are further described below. Additional calculations for the neutron knock-out were performed using Bonaccorso's eikonal approach [39] and transfer-to-continuum method [40], and these results are given in Section 3.3.4.

Table 3.1: Single-particle cross sections for neutron removal from ^{36}Ca calculated using MOMDIS (units of *mb*). Calculations should be compared within a section to see the effect of changing a single aspect of the calculation. Top section: density profiles for the core and target (used to calculate core+target S-matrix) were either matter densities or separate density profiles for *n* and *p* (allowing different parameter values for like and unlike nucleon interactions). Middle section: nucleon+target S-matrix was calculated either using the $t-\rho\rho$ approximation or from the integral of the DOM optical potential. Bottom section: potential used to calculate the bound-state wavefunctions (wfn) for the valence nucleon was either a Woods-Saxon potential, a local DOM potential, or a non-local potential. S-matrices used in this final section were calculated with Tostevin's reaction code.

				Density Profile				
	Description	S_c	S_n	Core	Nucleon	Target	Wfn	$\sigma_{sp}(-n)$
MOMDIS	S_c, S_n calculated using MOMDIS reaction code	$t-\rho\rho$	$t-\rho\rho$	HF - matter	Gaussian	Gaussian	WS	15.6
npDens	S_c calculated using separate n/p density profiles	$t-\rho\rho$	$t-\rho\rho$	HF - n/p separated	Gaussian	MC - n/p separated [38]	WS	13.1
MOMDIS	Uses S-matrices calculated using MOMDIS reaction code	$t-\rho\rho$	$t-\rho\rho$	HF - matter	Gaussian	Gaussian	WS	15.6
DOM-potential	S_n calculated from optical potential	$t-\rho\rho$	DOM potential	HF - matter	Gaussian	Gaussian	WS	18.6
Tostevin	Wfn from WS potential, S-matrices from Tostevin	Tostevin	Tostevin	-	-	-	WS	12.9
DOM-local	Wfn from local DOM potential, with non-local correction	Tostevin	Tostevin	-	-	-	Local DOM	13.2
nonlocal	Wfn from non-local potential	Tostevin	Tostevin	-	-	-	Non-local	13.7

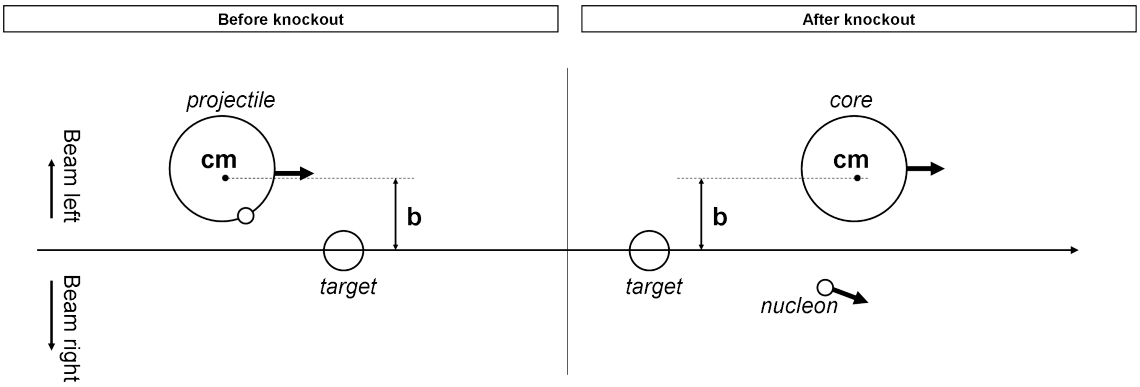

Figure 3.6: Schematic of the knockout reaction. A mass A projectile approaches a light mass target at an impact parameter b. The interaction between the projectile and target results in a nucleon being removed from the projectile, leaving a mass $A-1$ core (or residue).

3.3.1 Eikonal theory

To describe the knockout reactions, we consider a mass A projectile hitting a light mass target. The interaction between the projectile and target results in a nucleon being removed from the projectile, leaving a mass $A-1$ core (or residue). This is depicted schematically in Figure 3.6. The eikonal approximation assumes that the projectile and residue move in straight line trajectories at constant velocity, independent of impact parameter b (rather than paths curved by the Coulomb interaction). This approximation is valid when the beam energy is high, the scattering angle is small, and the reaction is surface localized [6]. In addition, the eikonal approach uses the sudden approximation, which assumes that the removal of the nucleon from the projectile is instantaneous, so that the remaining nucleons in the core are undisturbed. The sudden approximation also requires high beam energies so

that the interaction time is short compared to the time for nucleon motion in the core [41].

The ingredients required to calculate σ_{sp} in the eikonal model are the core-target and nucleon-target S-matrices (S_c and S_n, respectively), and the bound-state wavefunction for the orbital of interest. The wavefunction is calculated using a Woods-Saxon (WS) potential well. The radius r_0 and diffuseness a parameters are constrained by matching the r_{rms} of the wavefunction to HF calculations, and the depth V_0 is adjusted to reproduce the energy of the orbital. There is also a spin-orbit interaction term with a fixed magnitude of 6 MeV and the same values of r_0 and a as the WS potential.

The S-matrix is given by the exponential of the eikonal phase χ, both of which are functions of of the impact parameter b,

$$S(b) = \exp[i\chi(b)]. \tag{3.3.1}$$

The eikonal phase is the sum of a Coulomb part χ_C, and a nuclear part, χ_N. The Coulomb part is given by

$$\chi_C(b) = 2\eta \ln(kb), \tag{3.3.2}$$

where η is the Sommerfeld parameter ($\eta = \frac{Z_p Z_t e^2}{\hbar v}$), v is the relative velocity between the projectile (charge Z_p) and target (charge Z_t), and k is their wavenumber in the center-of-mass system. The nuclear part was calculated in two ways, both of which are described in the next section.

The sp knockout cross section is the sum of contributions from stripping (inelastic breakup) and diffractive (elastic) breakup. There is also an elastic contribution due to Coulomb dissociation, which is small enough for light targets to be neglected in these reac-

tions. The two remaining contributions are calculated from the S-matrices, S_c and S_n, and the wavefunction for the orbital of interest, ϕ_{jm}, by [42]

$$\sigma_{str} = \frac{1}{2j+1}\int d\vec{b}\sum_m \langle \phi_{jm} \mid (1-|S_n|^2)|S_c|^2 \mid \phi_{jm}\rangle \tag{3.3.3}$$

$$\sigma_{dif} = \frac{1}{2j+1}\int d\vec{b}\left[\sum_m \langle \phi_{jm} \mid |1-S_nS_c|^2 \mid \phi_{jm}\rangle - \sum_{m,m'} |\langle \phi_{jm'} \mid (1-S_nS_c) \mid \phi_{jm}\rangle|^2\right]. \tag{3.3.4}$$

Although the form of the diffractive cross section is not intuitive, the stripping cross section has a simple physical interpretation as the product of the probability that the core survives to reach the detector ($|S_c|^2$), and the probability that the nucleon is removed from the projectile via the interaction with the target ($1-|S_n|^2$) [42].

3.3.2 S-matrices

To determine the sensitivity of our results to the details of the S-matrix calculations, they were repeated for the neutron-knockout reaction using several different methods, most notably by using a double folding ($t-\rho\rho$) approximation to calculate χ_N from the NN interaction and the density profiles of the core, nucleon, and target, and by using the dispersive optical model (DOM) to calculate χ_N for the nucleon-target directly from an optical potential which is constrained by extensive scattering and reaction data. These gave values of σ_{sp} that were consistent to within about 20% (see Table 3.1), and are further described below. Figures 3.7 and 3.8 show plots of the eikonal S-matrices for the core-target (S_c) and the nucleon-target (S_n), respectively, corresponding to the calculations described below.

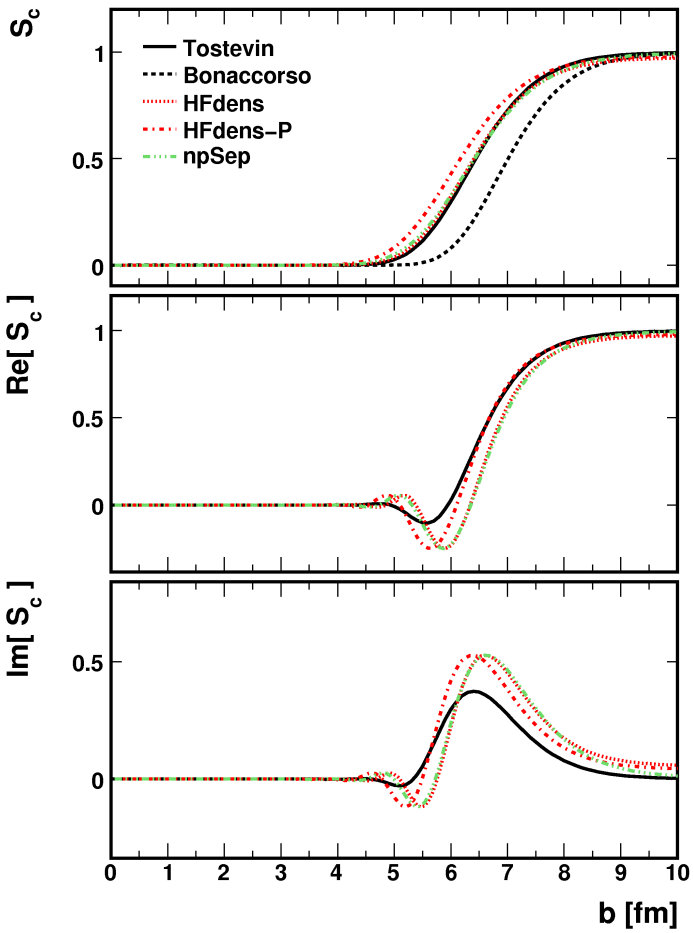

Figure 3.7: Plot of core-target S-matrices as a function of impact parameter b, calculated using different method or input. "Tostevin" and "Bonaccorso" calculations were done with their respective eikonal reaction codes. The remaining calculations were done with MOMDIS [37]. "HFdens" uses core matter density profiles from Hartree-Fock calculations, "HFdens-P" includes the effect of Pauli blocking, and "npSep" uses separate n and p density profiles as described in the text. For $S_c \to 1$ (large b), the core survives, and for $S_n \to 0$ (small b), the core is destroyed.

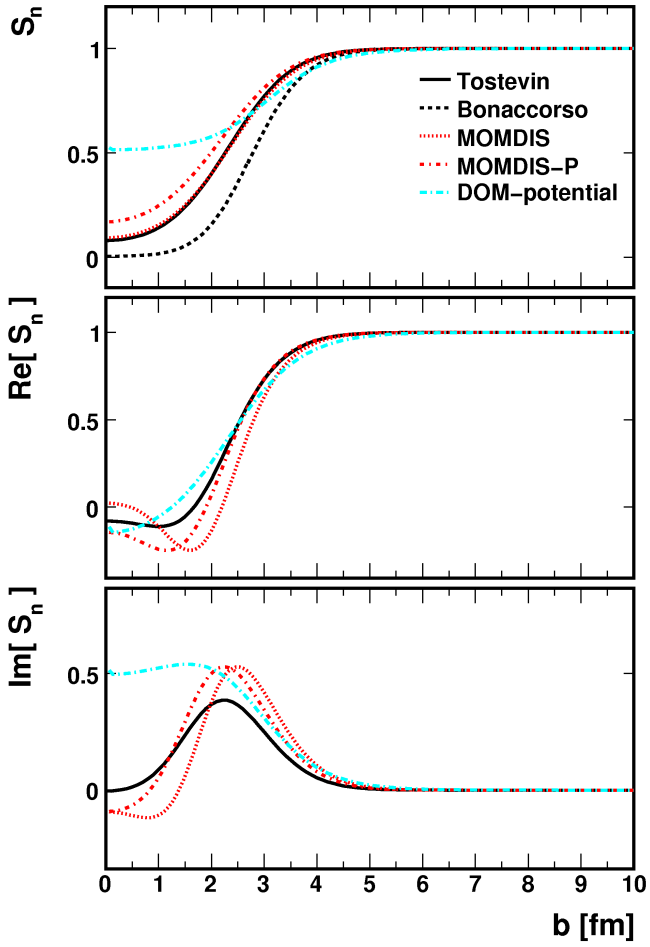

Figure 3.8: Same as 3.7, but for nucleon-target S-matrices. "MOMDIS" uses the $t-\rho\rho$ method to calculate the eikonal phase, while "DOM-potential" calculates it directly from an optical potential obtained from the DOM. "MOMDIS-P" includes the effects of Pauli blocking. For $S_n \to 1$ (large b), the nucleon is not removed from the projectile, and for $S_n \to 0$ (small b), the nucleon is removed from the projectile.

3.3.2.1 Using the $t-\rho\rho$ approximation (double folding)

In this approximation, the eikonal phase is given by [37]

$$\chi_N(b) = \frac{1}{k_{NN}} \int_0^\infty dq\, q \rho_p(q) \rho_t(q) f_{NN}(q) J_0(qb). \tag{3.3.5}$$

This method uses the Fourier transform of the target and core (or nucleon) density profiles (ρ_t and ρ_p respectively) along with the free nucleon-nucleon cross-sections (σ_{NN}) to determine the eikonal phase. The integration is performed over $q = 2k\sin(\theta/2)$, where k is the momentum transferred and θ is the scattering angle. The scattering amplitude $f_{NN}(q)$ is parametrized by [37]

$$f_{NN}(q) = \frac{k_{NN}}{4\pi}(i+\alpha_{NN})\sigma_{NN}\exp(-\beta_{NN}q^2). \tag{3.3.6}$$

The parameters σ_{NN}, α_{NN} (ratio between real and imaginary parts of scattering amplitude), and β_{NN} (non-locality parameter) are determined from scattering data at energies from 30 MeV up to a few GeV [43]. For the energies of interest in this work, $\beta_{NN} = 0$. Using the MOMDIS code to calculate both the core-target and nucleon-target S-matrices in this way, single-particle cross sections of $15.6\,mb$ and $20.8\,mb$ were obtained for neutron and proton knockout, respectively. There is also the effect of Pauli blocking, which modifies the free-NN cross sections. This results in both S_c and S_n being "pushed in" compared to calculations which do not include Pauli blocking (see Figures 3.7 and 3.8) and the net effect is to reduce the knockout cross sections by about 5%.

3.3.2.2 Using the DOM optical potential

The eikonal nuclear phase was also calculated directly from an optical potential U by

$$\chi_N(b) = \int_{-\infty}^{\infty} dz U(z,b). \tag{3.3.7}$$

The optical potentials for nucleon (n or p) + target (^{9}Be) were obtained from DOM fits to scattering and reaction data. The resulting S-matrices differed from those calculated using the $t-\rho\rho$ approximation most strikingly in that they were non-zero as $b \to 0$ (i.e. the DOM includes the experimentally observed finite transmission at small impact parameters), as can be seen in the S-matrix for *neutron*-knockout plotted in Figure 3.8. This difference had only a relatively small effect on the calculated cross sections, however, because in the cross section formulas (see Equations 3.3.3 and 3.3.4), the nucleon S-matrix always appears multiplied by the core survival amplitude, which goes to zero as $b \to 0$. The *neutron*- and *proton*-knockout sp cross sections calculated using the nucleon-target S-matrices from the DOM optical potential were $18.56\,mb$ and $24.49\,mb$, respectively.

3.3.2.3 Density profiles

In the calculations described in Section 3.3.2.1, the matter densities for the target and core were used and the parameters of the interaction were isospin averaged. It is possible instead to calculate S_c using the proton and neutron densities for the target and core, so that one has separate terms for like ($p-p$ or $n-n$) and unlike ($p-n$) nucleon interactions. When separate n and p density distributions were used for only the core, the resulting n-knockout sp cross section was about 2% smaller than when using the matter density. However, when

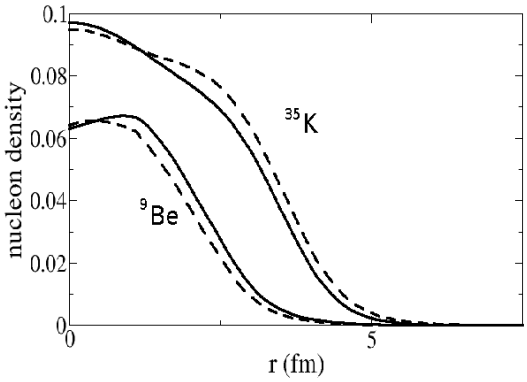

Figure 3.9: Plot of n (solid) and p (dashed) density distributions for ^{35}K and ^{9}Be.

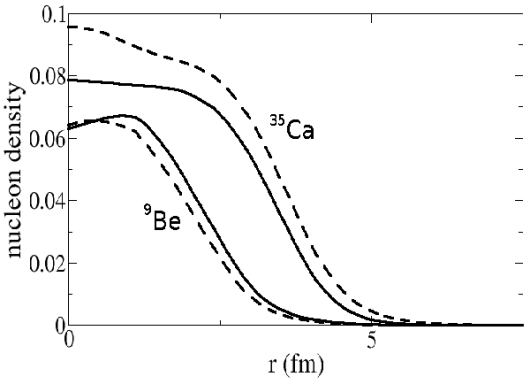

Figure 3.10: Plot of n (solid) and p (dashed) density distributions for ^{35}Ca and ^{9}Be.

separate n and p density profiles were used for both the core and target, the cross section was over 20% smaller, yielding $\sigma_{sp} = 13.1\,mb$ for the knockout of the strongly bound neutron (see Table 3.1). The S-matrix calculated using separate n and p density profiles for both the core and target is shown in Figure 3.7.

The densities for the core were obtained from Hartree-Fock (HF) calculations using B. A. Brown's DENS program. The matter density profile for the ^{9}Be target was assumed to be Gaussian, $\rho_t = e^{-\left(\frac{r}{\alpha}\right)^2}$ with a range $\alpha = 1.93\,fm$, while the separate n and p densities for ^{9}Be were obtained from quantum Monte Carlo (MC) calculations [38]. Figures 3.9 and 3.10 show the separate n (solid) and p (dashed) density distributions for ^{35}K and ^{35}Ca, respectively. Both plots also include the n and p density distributions for the ^{9}Be target.

A more extended density profile results in a smaller knockout cross section due to the decreased core survival probability. One might wonder whether (by using a distribution that

is extended enough) one can obtain calculated cross sections σ_{sp} which imply a spectroscopic factor that is consistent with the results from transfer reactions and DOM analyses. However, as the tail of the distribution is pushed out radially, the density at the center of the nucleus must decrease to maintain a density distribution which integrates to A.

Using an extended density distribution which had a central density of 0.125 fm^{-3} (which is 75% of ρ_0, the saturation density) resulted in a calculated cross section $\sigma_{sp} = 10.7\,mb$. A sp cross section of around $4\,mb$ is required in order for the extracted SF to be in line with DOM and transfer results. To obtain a calculated sp cross section this small, the density distribution would need to be extended so far that the central density would drop to an unreasonably low value. Thus one cannot reconcile the differences between transfer and knockout results by any reasonable adjustment of the density distribution input to the knockout calculations.

3.3.3 Wavefunctions

There was very little sensitivity to the use of any reasonable wavefunction, whether calculated using the WS potential as described above, obtained from the DOM using a local potential (with a non-local correction), or using a non-local potential [44]. These wavefunctions are shown in Figures 3.11b and 3.12b, for the ^{36}Ca valence neutron and proton, respectively. The sp cross sections calculated using these wavefunctions are within about 6% of each other (see final section of Table 3.1).

As described above, the sp cross section is an integral of the S-matrices and wavefunction over the two spatial coordinates $\overrightarrow{b}$ (projectile-target) and $\overrightarrow{r}$ (nucleon-core). In order

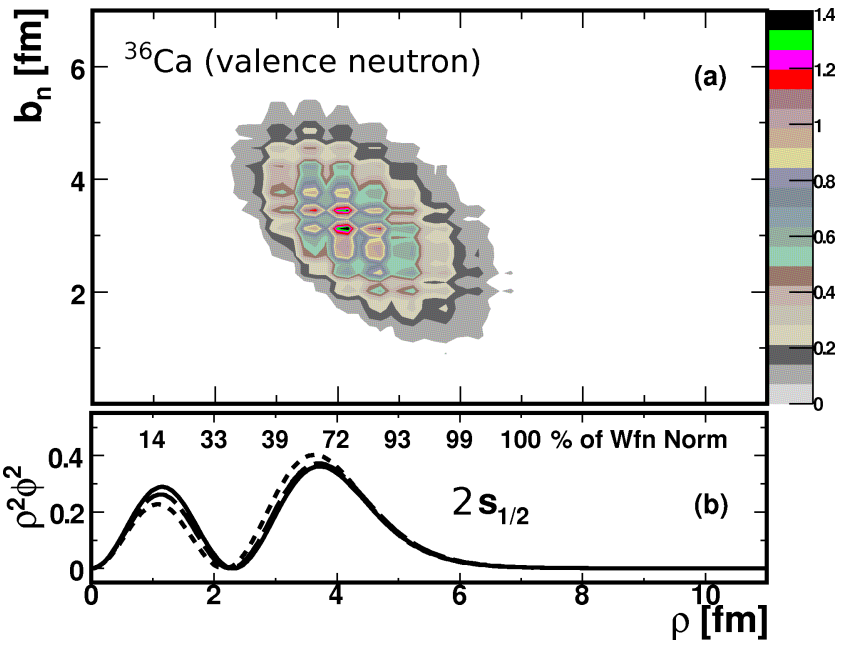

Figure 3.11: (a) Plot of $\frac{d^2\sigma_{str}}{db_n d\rho}$ for *neutron* knockout from ^{36}Ca as a function of nucleon impact paramater b_n (nucleon-target transverse distance) and internal projectile radial coordinate ρ (nucleon-core transverse distance). (b) The square of the $2s_{1/2}$ bound-state wavefunction for the valence neutron in ^{36}Ca, multiplied by ρ^2. The upper scale displays the percentage of the wavefunction (wfn) norm that is within the corresponding radial distance. The three curves are the wavefunction calculated in a WS potential (solid), non-local potential (long dashed), and local DOM potential (short dashed).

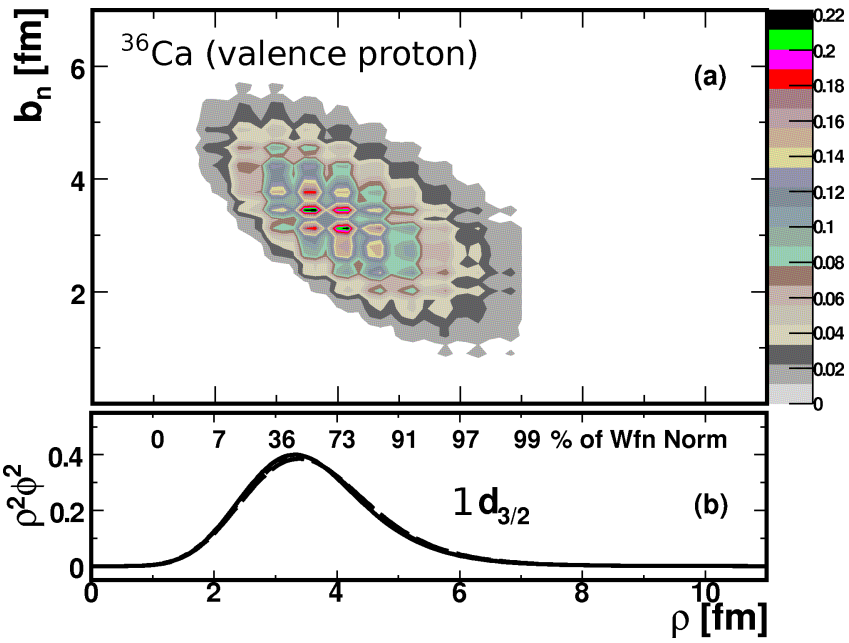

Figure 3.12: (a) Plot of $\frac{d^2\sigma_{str}}{db_n d\rho}$ for *proton* knockout from ^{36}Ca as a function of nucleon impact paramater b_n (nucleon-target transverse distance) and internal projectile radial coordinate ρ (nucleon-core transverse distance). (b) The square of the $1d_{3/2}$ bound-state wavefunction for the valence proton in ^{36}Ca, multiplied by ρ^2. The upper scale displays the percentage of the wavefunction (wfn) norm that is within the corresponding radial distance. The three curves are the wavefunction calculated in a WS potential (solid), non-local potential (long dashed), and local DOM potential (short dashed).

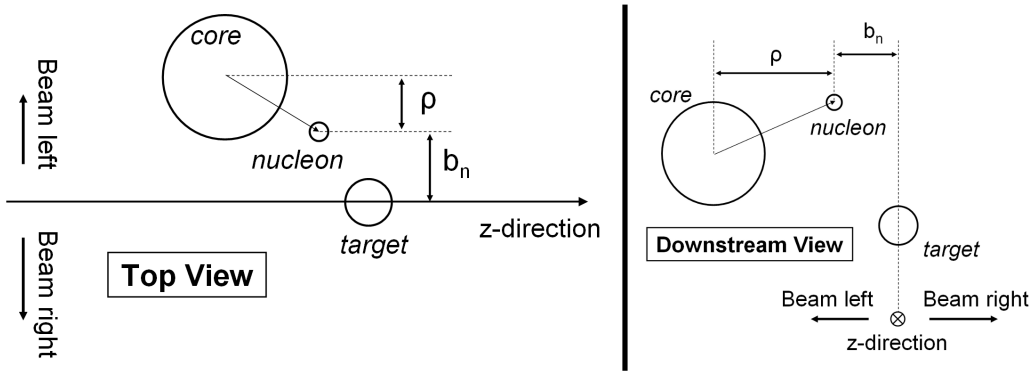

Figure 3.13: Schematic of the coordinates used to describe the knockout process - the nucleon impact parameter b_n (which is the transverse nucleon-target distance, the component of the nucleon-target distance perpendicular to the beam direction) and the internal projectile coordinate ρ (which is the transverse nucleon-core distance).

to gain insight into what part of the wavefunctions are sampled in the knockout reaction, we looked at where, in coordinate space, the calculated cross section comes from. In Figures 3.11a and 3.12a, we plot $\frac{d^2\sigma_{str}}{db_n d\rho}$ for the neutron and proton knockout, respectively, as a function of the nucleon impact parameter b_n (which is the transverse nucleon-target distance, the component of the nucleon-target distance perpendicular to the beam direction) and the internal projectile coordinate ρ (which is the transverse nucleon-core distance). See Figure 3.13 for a schematic defining these coordinates. The corresponding bound-state wavefunctions are plotted in Figures 3.11b and 3.12b, for the WS, non-local, and DOM (local) potentials.

One notices that contributions to the cross section peak around $b_n = 3\,fm$ and $\rho = 4\,fm$, and extend over an oval-shaped spatial region oriented diagonally to the axes, roughly

where $3 < b_n < 5.5\,fm$ and $2 < \rho < 6.5\,fm$. The shape and orientation of this region makes sense in light of the fact that the distance between the projectile and target must be roughly constant - neither too large (or the nucleon is not stripped), nor too small (or the core does not survive). So as b_n gets larger (nucleon-projectile distance increases), ρ must get smaller (nucleon-core distance shrinks) to maintain the projectile center-of-mass distance from the target.

The bound-state wavefunctions for the valence neutron and proton in ^{36}Ca have $r_{rms} \approx 3.4\,fm$ and $r_{rms} \approx 3.8\,fm$, respectively, so we conclude that the although the knockout reaction is strongest near the surface and does not reach the innermost part of the nucleus, it certainly probes more than just the tail of the wavefunctions. However, the amount of the wavefunction probed differs between the neutron and proton, because the neutron is tightly bound while the proton is more loosely bound. About 35% of the neutron wavefunction is within $\rho = 2\,fm$, and is thus not sampled in the neutron-knockout reaction. For the proton, only 10% of the wavefunction is within $\rho = 2\,fm$ and remains unsampled.

3.3.4 Additional calculations

Calculations for the neutron knockout were performed using Bonaccorso's eikonal approach [39] and transfer-to-continuum method [40]. The Bonaccorso calculations are roughly 20% smaller than the results from Tostevin's code. This difference comes from the eikonal S-matrices for the core-target, S_c, (shown in Figure 3.7). In the Bonaccorso calculation, S_c is "pushed out" toward higher impact parameters (i.e. the point at which $S_c = 0.5$ for the Bonaccorso calculation occurs at a higher value of b than the Tostevin

calculation), making the core survival amplitude (and thus the cross section) smaller.

Additionally, an intranuclear cascade calculation (INC) was performed for both the neutron and proton knockout by A. Obertelli. This is a Monte Carlo calculation which considers knockout processes following multiple interactions within the projectile (for number of interactions $N_{int} = 1$, this is equivalent to direct knockout), as well as excitation/evaporation processes. In other highly n/p asymmetric systems, these calculations have been shown to give nucleon removal cross sections which are close to the experimental values (within about 40%) for both weakly and strongly bound valence nucleons[45]. This is in contrast to eikonal models which, as discussed, give removal cross sections for strongly bound nucleons that are much larger than experiment.

For ^{36}Ca, these INC calculations gave neutron- and proton-knockout cross sections of 19.3 and 51.6 *mb*, respectively. Surprisingly, the calculated cross section for removal of the deeply bound neutron is similar to those from eikonal models, and much larger than the experimental cross section. It is not understood why the INC calculations do so poorly for the deeply bound neutron in ^{36}Ca (as compared to the relative success achieved for similarly deeply bound nucleons in other nuclei). The authors would like to obtain experimental results at higher energies to compare the success of this reaction model at different energies.

While the comparison of these INC model calculations to experimental knockout cross sections is of value, one would not expect much insight into nuclear structure to result from such a comparison. At its core, the INC model is classical, i.e. one bag of classical particles hitting another.

3.4 Analysis

3.4.1 Gamma-ray spectra

Knockout residues are not necessarily produced in the ground state. There can also be knockout reactions leading to excited states, which would decay before being detected - either to the ground state, if the populated state is bound, or to a different exit channel if the populated state is unbound. Knockout to any bound state is indistinguishable in the S800 from knockout to the ground state. If left uncorrected, this feeding from excited states would lead to an over-estimation of the ground-state knockout cross section. The CAESAR array provides the data necessary to correct for any such feeding.

In addition to ^{36}Ca *n*- and *p*-knockout residues, many other nuclei were available for study because there were several isotones in the incoming (secondary) beam, and multiple knockout products from each were seen in the S800 spectrometer. Reaction products from the ^{34}Ar,^{35}K, and ^{36}Ca entrance channels are discussed here. The strongest reaction channels observed are listed in Table 3.2, and a summary of observed gammas is given in Table 3.3. All gamma-ray data shown here are from the neutron-knockout runs, on which the bulk of the time was spent. (The cross section for knockout of the strongly-bound neutron was an order of magnitude less than that for the removal of the weakly-bound proton. This difference dictated our allotment of beam time to the study of each (n or p) removal.) In the spectra and level schemes shown in Figures 3.15 and 3.16 small (black) arrows indicate previously known gamma rays and larger (green) arrows indicate newly observed gamma rays.

Table 3.2: Strongest reaction channels.

Residue	Channel(s)	Residue	Channel(s)
^{35}K	^{36}Ca $\rightarrow -p$	^{31}S	^{34}Ar $\rightarrow -2p, -n$
^{35}Ca	^{36}Ca $\rightarrow -n$	^{29}P	^{34}Ar $\rightarrow -3p, -2n$
^{33}Ar	^{36}Ca $\rightarrow -n, -2p$ ^{35}K $\rightarrow -n, -p$ ^{34}Ar $\rightarrow -n$	^{32}Ar	^{36}Ca $\rightarrow -2n, -2p$ ^{35}K $\rightarrow -2n, -p$ ^{34}Ar $\rightarrow -2n$
^{32}Cl	^{36}Ca $\rightarrow -n, -3p$ ^{35}K $\rightarrow -n, -2p$ ^{34}Ar $\rightarrow -n$,-p	^{30}S	^{36}Ca $\rightarrow -2n, -4p$ ^{35}K $\rightarrow -2n, -3p$ ^{34}Ar $\rightarrow -2n, -2p$
		^{29}S	^{36}Ca $\rightarrow -3n, -4p$ ^{35}K $\rightarrow -3n, -3p$ ^{34}Ar $\rightarrow -3n, -2p$

Since the separation energy of ^{35}K is only 78 keV, it is likely that there are no bound excited states, and thus no gamma rays from excited-state decay were expected. For ^{35}Ca, the separation energy has the much larger value of 1.40 MeV. However, since the first excited state in the isobaric analog ^{35}K is at 1.55 MeV, it was again expected that there were no particle-stable excited states. The gamma-ray spectra (shown in Figure 3.14) are consistent with these expectations. This simplifies the analysis considerably, since we can now assume that all observed residues resulted from nucleon knockout from the ground state of the projectile to the ground state of the residue. Thus there is no need to subtract any feeding from excited-state decays.

Gamma decay was observed from several of the other nuclides. Comparing the observed gamma-ray spectra to published data helped to confirm our particle identification. For example, the observed peaks for ^{32}Ar (shown in Figure 3.15a) are all consistent with

Table 3.3: Gamma rays observed in this experiment. Energies are given in *keV*. Where available, an association to previously published literature data is made.

Residue	$E_{\gamma,exp}$	$E_{\gamma,lit}$[a]	E_{level}[b]
^{35}K	-		
^{35}Ca	-		
^{33}Ar	633	639	2439
	1394	1359, 1356	1359, 3154
	1846	1798	1798
	2507	2460	3819
^{32}Cl	457	466	466
	707	702	1168
	1316		(1326)
	1685		(1719)
	2082		(2122)
^{32}Ar	1906	1867	1867
^{31}S	1276	1248	1248
	2189	2235	2235
^{30}S	1212	1192	3402
	1519	1456, 1466	3666, 3676
	1828	1734?	5136
	2254	2211	2211
	2989	2926	5136
^{29}S	1242	1222	1222
	1745	1727	1727
^{29}P	584	570	1954
	1414	1384	1384
	2015	1954	1954

[a]Literature data were obtained from ENSDF [46] except ^{29}S which is from [47]

[b]Values in parenthesis are proposed positions of previously unobserved gammas

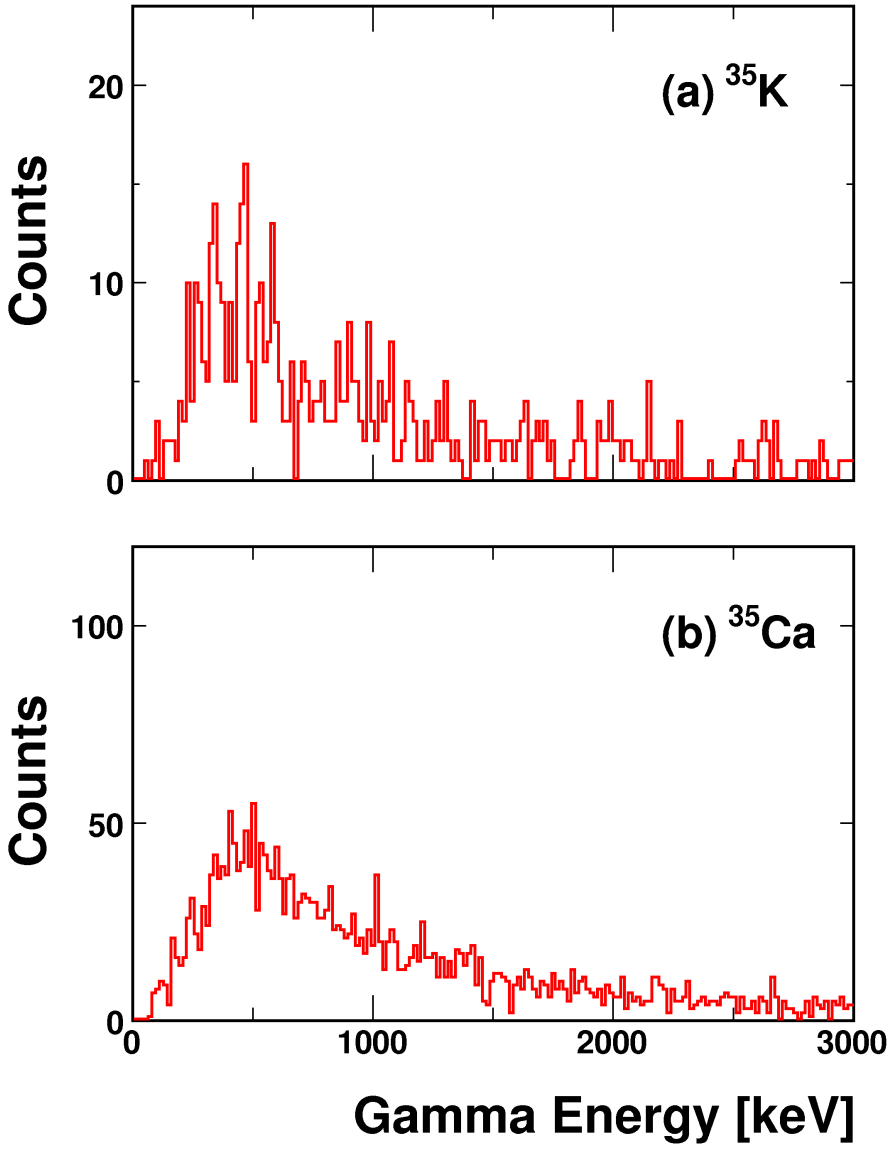

Figure 3.14: Plot showing observed gamma-ray spectra for (a) ^{35}K and (b) ^{35}Ca. No gamma rays from excited-state decay were observed, indicating that these knockout residues were produced in their ground states.

published data for this nucleus. Figure 3.15b shows the measured spectrum for ^{32}Cl, for which several gamma rays were known, but for which none had been observed above 1 MeV. Three previously unreported transitions were observed at 1343 keV, 1691 keV, and 2082 keV. Considering the partial level scheme shown in Figure 3.16, it is reasonable to believe that these transitions occur between known levels, as indicated by the large arrows. These levels were observed in transfer reactions [48] but no gamma spectroscopy had been done.

3.4.2 ^{29}S gamma-ray spectrum

The gamma-ray spectrum in coincidence with ^{29}S is shown in Figure 3.15c. This nucleus was observed as a product of the ^{34}Al, ^{35}K, and ^{36}Ca entrance channels. Two gamma-ray peaks are seen at $1246 \pm 10\,keV$ and $1738 \pm 8\,keV$, with widths (FWHM) of about 150 and 125 keV, respectively. We did not find evidence that these gamma rays are in coincidence, suggesting excited states in ^{29}S at these gamma-ray energies. The presence of excited states at 1398 keV and 1745 keV in the mirror nucleus ^{29}Al lends credence to this scheme, and allows a tentative assignment of spin, based on systematics. A recent experiment [47] studied the spectroscopy of ^{29}S, and their results suggest that our peak at $1246\,keV$ is a doublet. They conclude that the lower-energy gamma ray of this doublet is from a third state at $2887\,keV$ which feeds the second excited state.

The level schemes for ^{29}S and ^{29}Al are shown in Figure 3.17. It is worth noting that the excitation energy of the $1/2+$ level in ^{29}S is smaller than that of the corresponding state in the mirror nucleus by 176 keV, whereas the $7/2+$ level energy differs by only about 27 keV

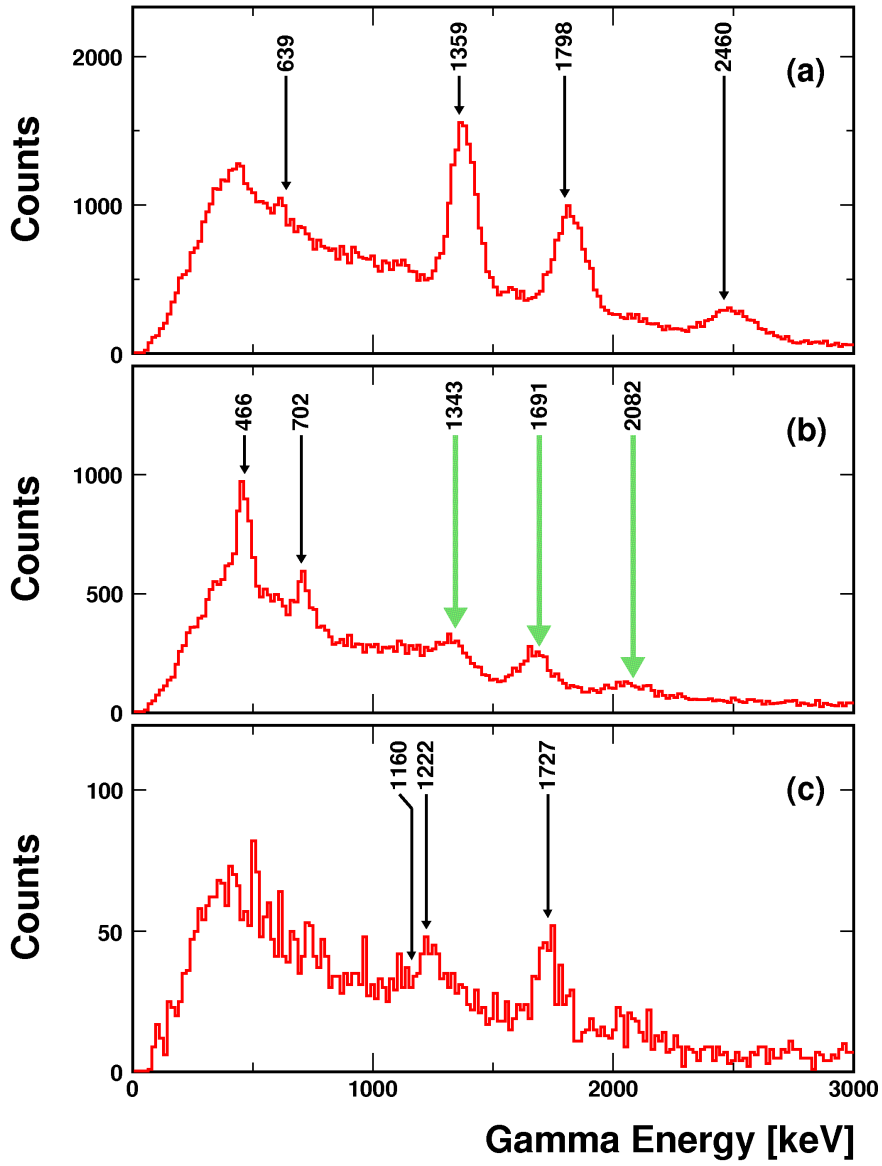

Figure 3.15: Plot showing observed gamma-ray spectra for (a) ^{33}Ar, (b) ^{32}Cl, and (c) ^{29}S. The small black arrows indicate previously reported gamma rays, and the larger green arrows indicate new gamma rays. Peak energies are given in keV.

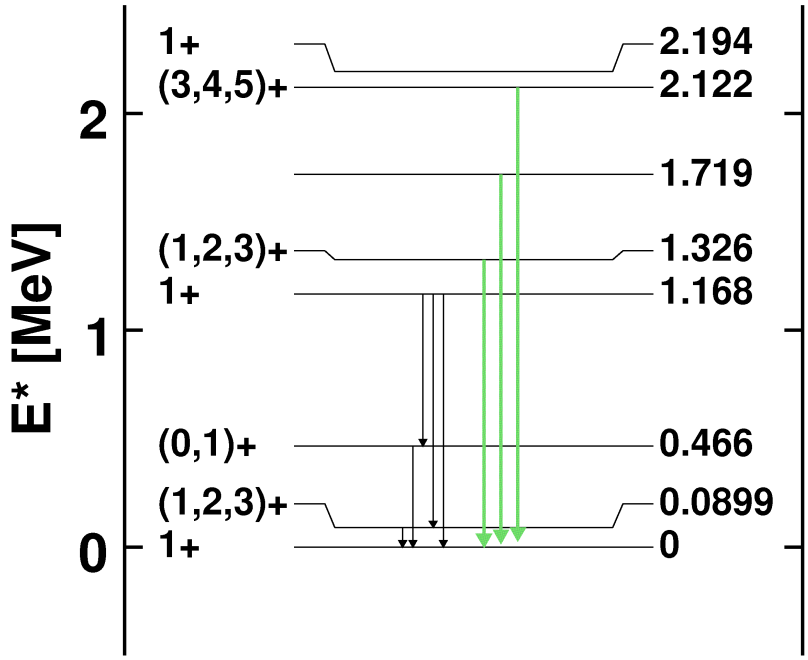

Figure 3.16: Partial level scheme for ^{32}Cl, showing gamma rays observed in this work. Previously reported gamma rays are shown as small black arrows, and the tentative placement of newly observed gamma rays is given by the larger green arrows.

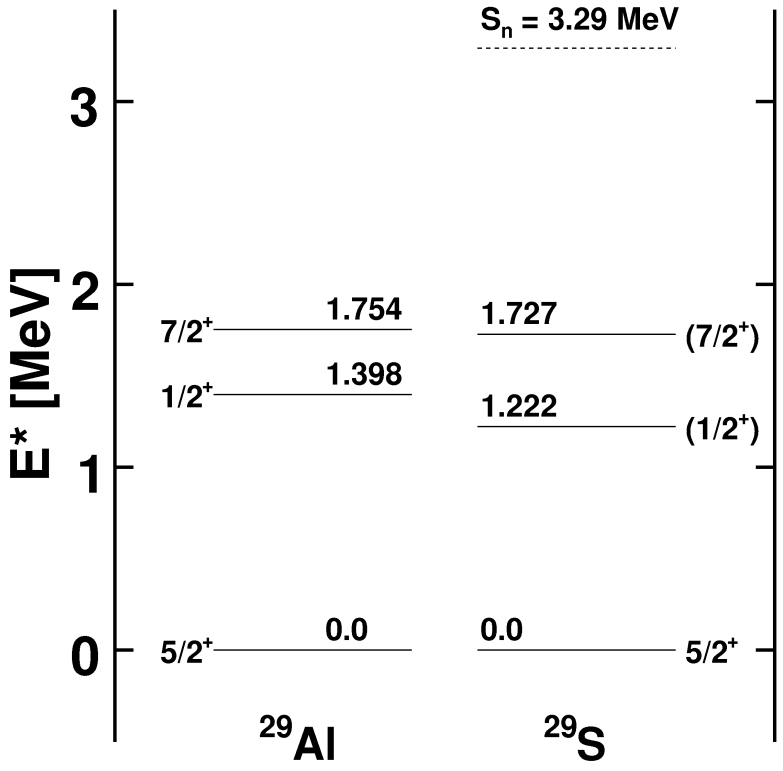

Figure 3.17: Partial level scheme for ^{29}S and its isobaric analog ^{29}Al.

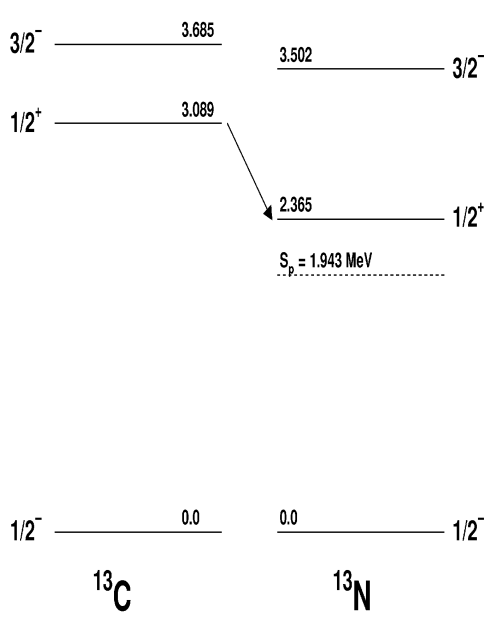

Figure 3.18: Level scheme for mirror pair ^{13}C-^{13}N. Energies are given in MeV.

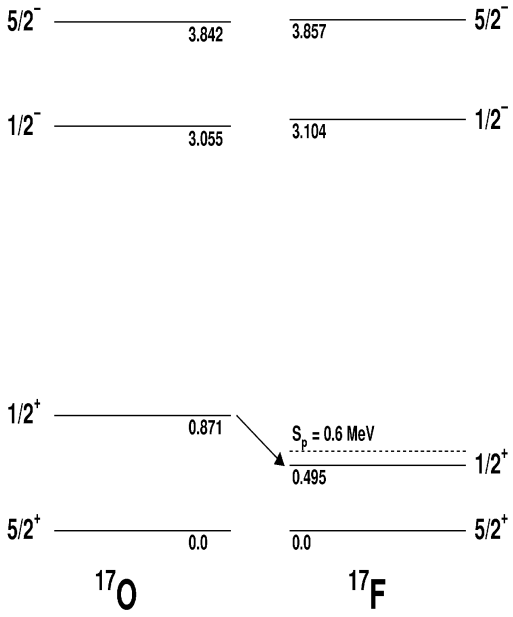

Figure 3.19: Level scheme for mirror pair ^{17}O-^{17}F. Energies are given in MeV.

(using the values from [47]). All of the states in the mirror will exhibit a Coulomb upshift due to the differing number of protons, however this upshift seems to be reduced for the $1/2+$ level. This brings to mind the Thomas-Ehrman (TE) shift, in which orbits without a confining centrifugal barrier (i.e. *s*-states), exhibit a more extended wavefunction, and thus a reduced Coulomb energy shift, when the proximity of the continuum is far closer in one of the mirror nuclei than in the other. The famous cases of this are the pairs ^{13}C-^{13}N and ^{17}O-^{17}F, whose level schemes are shown in Figures 3.18 and 3.19. In both cases, the $1/2+$ level is shifted down (relative to other states in the nucleus) for the mirror partner where the odd nucleon in the *s*-state is a proton.

Table 3.4: (top) Physical states in ^{29}S and mirror nucleus ^{29}Al. Level energies and mirror shifts are given in MeV. Energies for ^{29}S states are from [47]. (bottom) Dominant single-particle components of ^{29}S wavefunctions, calculated by B. A. Brown using the USD interaction. [49]

J^π	E (^{29}Al)	E (^{29}S)	Mirror Shift
5/2+	0.	0.	
1/2+	1.398	1.222	0.176
7/2+	1.754	1.727	0.027

J^π	n $d_{5/2}$	n $s_{1/2}$	p $d_{5/2}$	p $s_{1/2}$	p $d_{3/2}$
5/2+	5	0	6	2	0
1/2+	4	1	6	2	0
7/2+	5	0	6	1	1

Since the present case involves next-to-nearest neighbor mirror nuclei, where the difference is not just the change of a single $n \rightarrow p$, the interpretation is not as simple. However, we can gain some perspective by considering the single-particle configurations that make up these states. While the wavefunctions are complicated, the dominant components are shown in Table 3.4. These configurations can be associated with the physical low-lying states, also shown in Table 3.4. In the $T_z < 0$ partner, the $1/2^+$ configuration has an extra proton in the $1s_{1/2}$ level relative to the $T_z > 0$ partner, meaning there could be a TE-like shift

in the $T_z < 0$ partner for the states with contributions from this configuration. The $1/2^+$ configuration also has an extra proton in this $1s_{1/2}$ level relative to the $7/2^+$ configuration, which could further reduce its Coulomb upshift relative to that configuration. These two observations are consistent with the finding that the physical $1/2^+$ excited state exhibits a downshift in the $T_z < 0$ partner, and that this shift has a greater magnitude than the shift observed between the $7/2^+$ states.

3.4.3 Momentum distributions

The angular momentum of the knocked-out nucleon is determined from the shape of the longitudinal momentum distribution of the residues. The experimentally observed distributions are displayed in Figure 3.20 for both the proton- and neutron-knockout reactions from ^{36}Ca. Also shown are eikonal calculations for $l = 0$ (solid curve) and $l = 2$ (dashed curve). Note that the larger the orbital angular momentum of the sp state, the larger the momentum dispersion of the residue after a nucleon is removed from this orbit. Calculations for the sp levels of ^{36}Ca are shown in Figure 3.21. One would expect the valence neutron to occupy an $s_{1/2}$ orbital, and the proton to occupy a $d_{3/2}$ orbital, so that the knocked-out neutron would have $l = 0$, and the proton would have $l = 2$. A comparison between the experimental and calculated distributions confirms these expectations.

The slight asymmetry of the distribution (tail towards low momenta) has been observed in other knockout-reaction experiments, however the origin of this effect is not well understood [50]. The eikonal reaction theory can give only symmetric distributions, highlighting a shortcoming of this reaction model.

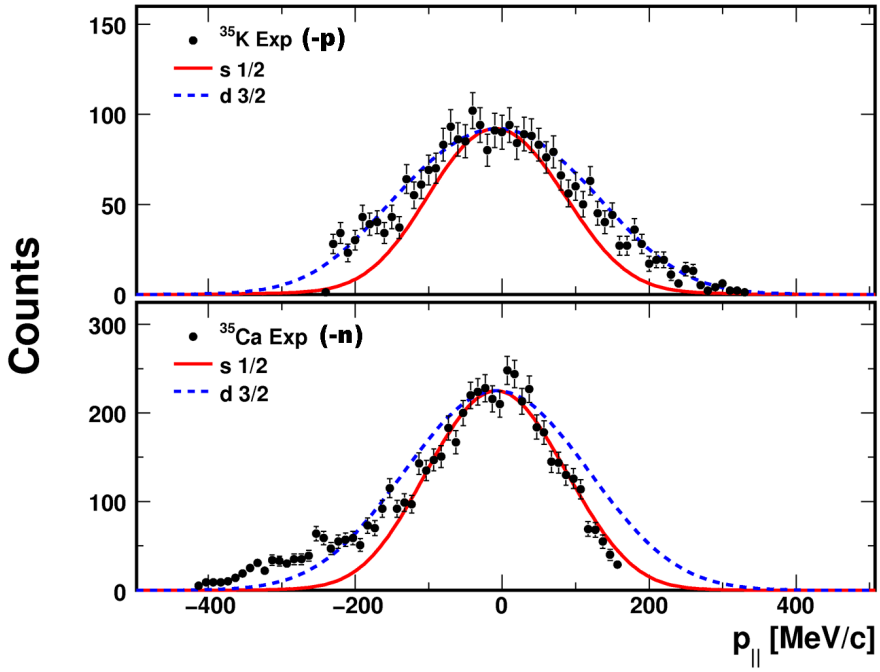

Figure 3.20: Longitudinal momentum distributions for the residues of the following reactions on ^{36}Ca: (a) proton-knockout to ^{35}K and (b) neutron-knockout to ^{35}Ca. Experimental data are given by the points. Eikonal calculations for $l = 0$ (solid curve) and $l = 2$ (dashed curve) are also shown. Comparison of the data to calculations indicate that the valence proton occupies a $d_{3/2}$ orbital, and the valence neutron occupies an $s_{1/2}$ orbital, consistent with calculated sp levels (see Figure 3.21).

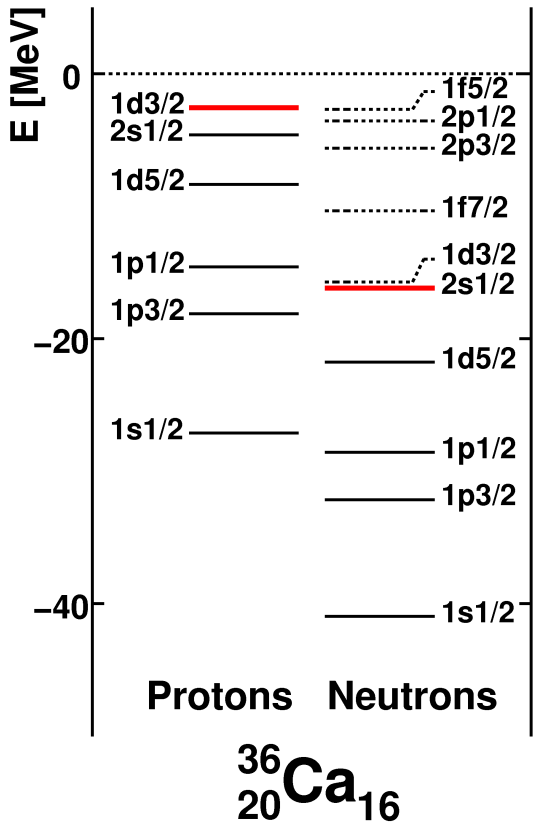

Figure 3.21: Calculated ^{36}Ca single-particle levels. Valence levels are shown as thick red lines, and unoccupied levels are dashed.

3.4.4 Knockout cross sections

The cross-section (σ) relates the number of knockout residues (N) to the number of incoming beam nuclei (N_b) and the areal number density ($\#/cm^s$) of target nuclei (n_{target}), i.e.,

$$N = \sigma\, n_{target} N_b. \tag{3.4.1}$$

The number of knockout residues observed experimentally (N_{obs}) is determined from the number of S800 triggers, gated on the corresponding knockout PID as described in Section 3.2. Since the computer has a dead time associated with each event, this number must be divided by the fraction of time that the acquisition system is live (τ_L) to account for events missed during the computer dead time. It must also be divided by the efficiency (ε_{det}) of the CRDCs (which measure focal-plane position) and scintillators (which measure TOF) to get the actual number of residues from the number detected. Thus, the actual number of knockout residues is given by

$$N \;=\; \left[\frac{N_{obs}^{knock}}{\varepsilon_{det}^{knock}\tau_L^{knock}}\right]. \tag{3.4.2}$$

The number of nuclei in the beam is determined in the same way, using data from runs in which only the unreacted beam was allowed to reach the focal plane. For each knockout run, this number is normalized by multiplying by the ratio of scalar counts during the knockout run to scalar counts during the unreacted beam run. The scalar counts (N_s) provide a measure of incoming beam intensity, and are obtained from either the XFP or OBJ scintillator. These two methods of normalizing gave cross-sections that were consistent to within a few percent, and the reported results use the average of these methods.

$$N_b(normalized) = \left\{ \frac{N_{obs}^{unreact}}{\varepsilon_{det}^{unreact}\tau_L^{unreact}} \frac{N_s^{knock}}{N_s^{unreact}} \right\}. \quad (3.4.3)$$

Thus, the cross section is calculated from the observed data by

$$\sigma = \frac{1}{n_{target}} \left[\frac{N_{obs}^{knock}}{\varepsilon_{det}^{knock}\tau_L^{knock}} \right]^{-1} \left\{ \frac{N_{obs}^{unreact}}{\varepsilon_{det}^{unreact}\tau_L^{unreact}} \frac{N_s^{knock}}{N_s^{unreact}} \right\}. \quad (3.4.4)$$

Since the live-time of the computer is rate dependent, it varied between S800 settings. It was between 50% and 85% for the four unreacted beam runs, and about 80% for the proton knockout runs. For the first part of the neutron knockout, we had significant amounts of unreacted beam reaching the focal plane, so the live time was only around 55%. After changing the arrangement to block more of the unreacted beam, the rate was drastically reduced, and the live time was over 90%. The detector efficiencies were also calculated separately for each run, but remained nearly constant around 99%.

A timeline of the experimental runs is given in Table 3.5. Four runs were taken with the unreacted beam - before either of the knockout runs, between the proton and neutron knockout runs, during the neutron knockout set of runs, and a final run following a fire alarm (which necessitated shutting down the cyclotron). Cross-section calculations were carried out using each of these runs as the "incoming beam" reference (since no *p*-knockout data were collected after the alarm, the post-alarm run was used only with the *n*-knockout data). The first three runs gave results which agreed to well within the statistical error bars. The post-alarm incoming beam reference run gave a neutron-knockout cross-section that was lower by more than twice the statistical error bars for the aggregate knockout data, but

Table 3.5: Timeline of experimental runs. The "Residue Setting" column indicates what nucleus the S800 was optimized for. A fire-alarm during Run 75 necessitated shutting down the RF, and subsequent runs are labeled "Post-alarm."

Runs(s)	Residue Setting	Comment
20	Unreacted ^{36}Ca	
25-33	^{35}K	
37	Unreacted ^{36}Ca	
43-57	^{35}Ca	
58	Unreacted ^{36}Ca	
61-74	^{35}Ca	A fire alarm during Run 75 necessitated shutting down the RF
80	Unreacted ^{36}Ca	
83-110	^{35}Ca	There was a 2nd fire alarm during run 98, but RF was not shut off

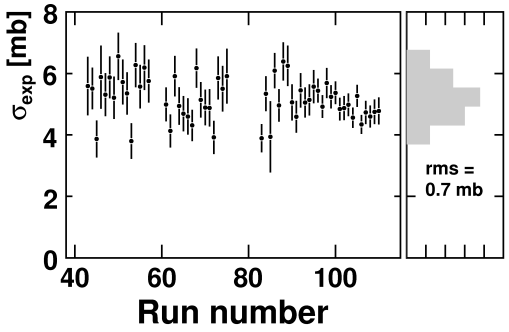

Figure 3.22: Run-by-run cross sections for *n*-knockout. On the far right is a plot of the distribution of cross sections, which had an rms deviation of 0.7 mb (14%) from the average.

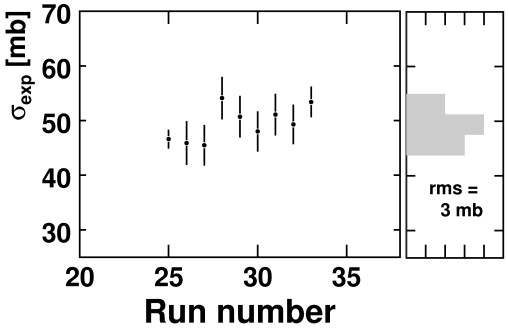

Figure 3.23: Run-by-run cross sections for *p*-knockout. On the far right is a plot of the distribution of cross sections, which had an rms deviation of 3 mb (6%) from the average.

amounted to no more than 7%. In addition, the post-alarm runs for the knockout data gave an average cross-section that was about 2% lower than that obtained from pre-alarm data.

Cross-sections were determined on a run-by-run basis initially, in order to check for inconsistencies. Results from the individual runs (shown in Figures 3.22 and 3.23 for neutrons and protons, respectively) agreed fairly well - e.g. for the neutron knockout, the rms deviation from the average cross section was 0.7 *mb* (14%) and is comparable to the statistical uncertainty of each run, which was around 0.6 *mb* (11%). The data were then aggregated to improve the statistics. The resulting cross sections are given in Table 3.6. The quoted uncertainties include a contribution from the target thickness uncertainty (2%). For

Table 3.6: Experimental cross sections for single nucleon knockout from ^{36}Ca to the ground state of the given residue. For each residue, the separation energy and the shell-model single-particle orbital of the particle is given. Also shown are the single-particle cross sections used to extract the spectroscopic factors from the experimental cross-sections. For the neutron, the sp cross sections were calculated using two eikonal methods (Tostevin and Bonaccorso) as well as the transfer-to-continuum method of Bonaccorso. The quoted σ_{sp} for the proton knockout is the Tostevin value. The last two columns contain the shell-model spectroscopic factors (average of USD, USDA, and USDB interactions, which are all very similar) and the deduced reduction factor (R_s).

Residue	s.p. orbital	Separation energy	σ_{exp} $[mb]$	$\sigma_{sp}[mb]$	$S_{deduced}$	$C^2S_{deduced}$	C^2S_{SM}	R_s
^{35}K	$d_{3/2}$	$S_p = 78keV$	51.1 ± 2.6				3.62	
			Eik, Tostevin	16.2	0.75	2.99		0.83
^{35}Ca	$s_{1/2}$	$S_n = 1400keV$	5.03 ± 0.46				1.80	
			Eik, Tostevin	11.1	0.21	0.43		0.24
			Eik, Bonaccorso	8.9	0.27	0.54		0.30
			TC, Bonaccorso	8.8	0.27	0.54		0.30

the n-knockout, there is also included a systematic uncertainty of 4% due to the discrepancy between pre- and post-alarm runs.

3.4.5 Spectroscopic and reduction factors

3.4.5.1 Experimentally deduced spectroscopic factor

Using the calculated sp cross sections given in Table 3.6, the experimental SF was deduced from

$$S_{deduced} = \frac{C^2 S_{deduced}}{2j+1} = \left(\frac{A-1}{A}\right)^2 \frac{\sigma_{exp}/\sigma_{sp}}{2j+1}, \tag{3.4.5}$$

where the factor $\left(\frac{A-1}{A}\right)^2$ is a center-of-mass (CM) correction appropriate for the *sd* shell. The resulting experimental SF are also given in Table 3.6. Multiple values are given for the neutron, corresponding to the various methods used to calculate σ_{sp}. As an example, the SF deduced for the valence nucleons in ^{36}Ca using the Tostevin eikonal values were $S_{deduced}(n, d_{3/2}) = 0.75$ and $S_{deduced}(p, s_{1/2}) = 0.21$. The standard interpretation of these values is that the spectroscopic strength of a single fragment of the correct quantum numbers is only 0.75 and 0.21 (for n and p respectively). These values are reduced relative to SM values by factors of 0.83 and 0.24 respectively. This is discussed further below.

3.4.5.2 Shell-model spectroscopic factor

The theoretical shell-model SF quantifies the contribution of each sp cross section to the theoretical knockout cross section, i.e.

$$\sigma_{thy} = \left(\frac{A}{A-1}\right)^2 \Sigma C^2 S_{SM} \sigma_{sp}, \tag{3.4.6}$$

where the sum is over all l and j values contributing to the orbital, and the factor $\left(\frac{A}{A-1}\right)^2$ is once again the CM correction to S_{SM}. To calculate σ_{thy}, one needs to multiply the sp cross-section by the theoretical SF. These were obtained from B. A. Brown's shell-model calculations (using the OXBASH code). The knocked-out neutron was in an $s_{1/2}$ orbital, with $C^2S_{SM} = 1.80$, and the knocked-out proton was in a $d_{3/2}$ orbital, with $C^2S_{SM} = 3.62$. (For reference, the extreme sp limit of C^2S would be $2j+1$, or 2 and 4 for the neutron and proton orbits, respectively.)

3.4.5.3 Calculation of reduction factor

The reduction factor, R_s, is defined as the ratio of the experimentally deduced SF, $C^2S_{deduced}$, to a theoretical shell-model SF, C^2S_{SM},

$$R_s = \frac{C^2S_{deduced}}{C^2S_{SM}}. \tag{3.4.7}$$

Neglecting the CM factors (which will cancel out), the experimental SF is given by the ratio of the experimental cross-section to the single-particle (sp) cross-section, $C^2S_{deduced} = \frac{\sigma_{exp}}{\sigma_{sp}}$, and the theoretical SF satisfies the relation $\sigma_{thy} = \Sigma C^2S_{SM}\sigma_{sp}$, where the sum is over all l and j values contributing to the orbital. When there is only one contribution (as in the reactions studied here), R_s can be written as

$$R_s = \frac{C^2S_{deduced}}{\sigma_{thy}/\sigma_{sp}} = \frac{\sigma_{exp}}{\sigma_{thy}}. \tag{3.4.8}$$

The calculated reduction factors are given in the last column of Table 3.6. The reduction factor for the weakly-bound valence proton is consistent with expectations that the SM

captures most of the relevant physics, with only 20% additional correlations beyond those captured in its model space.

3.4.6 Missing spectroscopic strength

A very small spectroscopic factor ($R_s \ll 1$) was deduced for the valence neutron in the ground state of ^{36}Ca. To make sense of this, we asked the question, "Where is the rest of the spectroscopic strength?" Since we didn't seem to find it in the knockout to the ground state of ^{35}Ca, the next logical place to look would be in the low-lying excited states, since the missing *s*-wave strength is more likely to be near the Fermi surface.

As expected (due to the small separation energy), and confirmed in the experiment (by the lack of observed gamma-ray peaks in the CAESAR spectrum), the excited states of ^{35}Ca populated in the experiment are unbound. Figure 3.24 shows the excitation function for both ^{35}Ca and ^{35}K particle evaporation, calculated with the decay code GEMINI++ [51]. From this figure we see that the neutron decay channels for excited states in these very proton-rich nuclei are negligible up to 20 MeV of excitation energy, and small (a few percent) beyond that. So excited states in ^{35}Ca will proton decay to ^{34}K, which is also unbound and proton decays to ^{33}Ar. The proton- and neutron-separation energies of ^{33}Ar are $S_p = 3.3\,MeV$ and $S_n = 15.3\,MeV$, respectively. Thus it is possible that this nuclide is produced in a bound state, which would be observed in our detectors.

Therefore, to find the missing spectroscopic strength, one reasonable approach is to look at the ^{33}Ar residues observed in coincidence with incoming ^{36}Ca. To make sense of the small spectroscopic factor for the valence neutron in the ground state of ^{36}Ca, one

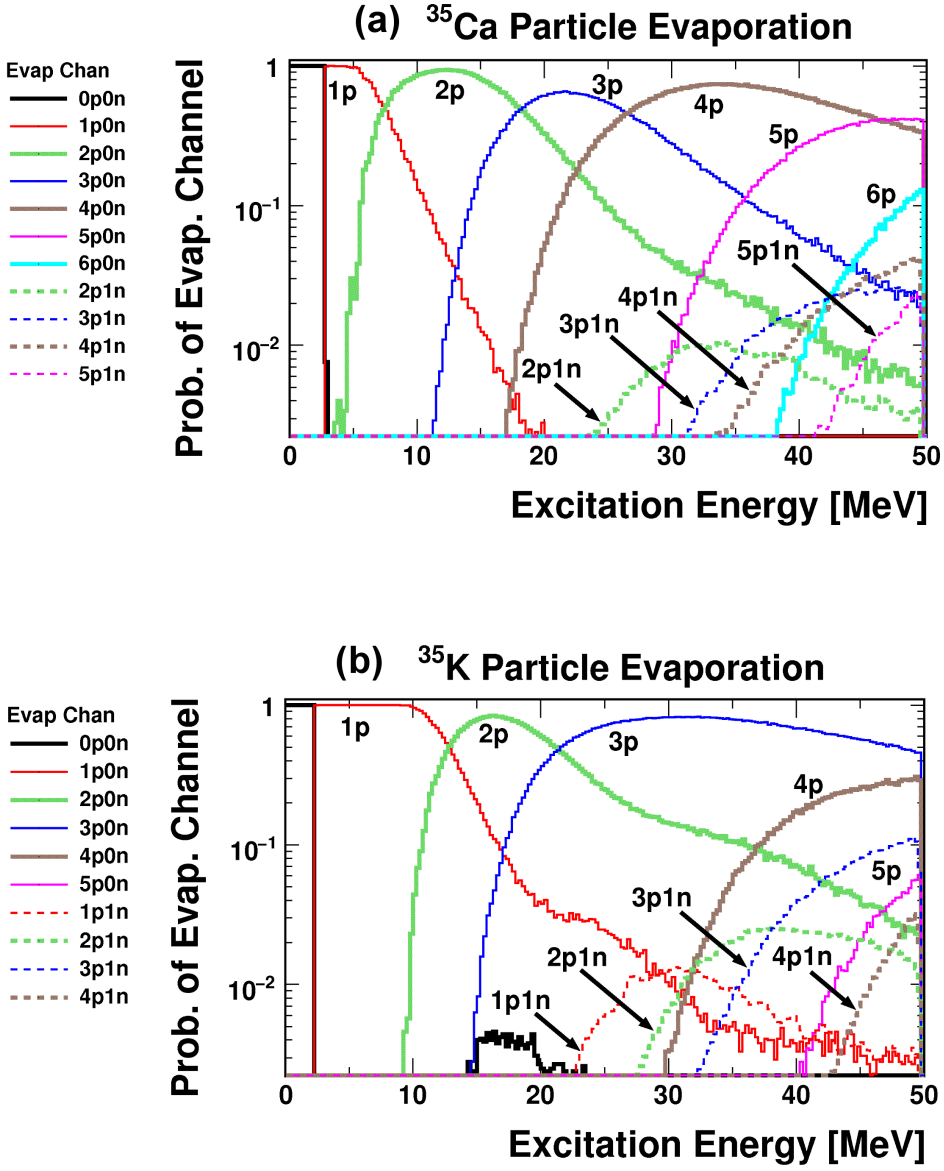

Figure 3.24: Probabilities for various evaporation channels in (a) ^{35}Ca and (b) ^{35}K as a function of excitation energy of the nucleus. Calculated with the decay code GEMINI++ [51].

would need to find not only an excess of cross section to this residue (beyond what is expected for other processes, such as direct $-n,-2p$ knockout), but also a cross section that is large compared to that observed to the (bound) ground state of ^{35}Ca. On the other hand, a small cross section would mean either that the spectroscopic strength is far from the Fermi surface or that the extracted spectroscopic factor is incorrect.

The experimental cross section for ^{9}Be(^{36}Ca,^{33}Ar)X was $28.6 \pm 1.5\,mb$. This is 5-6 times larger than the n-knockout cross section. If the spectroscopic factor extracted from the knockout analysis is accurate (i.e. if the $5\,mb$ cross-section to ^{35}Ca corresponds to 21% of the spectroscopic strength), then (depending on the cross sections for other processes) this could, in fact, account for a large portion (if not all) of the missing s-wave strength. For example, even if only half of this cross section is from decay of excited states in ^{35}Ca, this would represent an additional 60% of the spectroscopic strength, bringing the spectroscopic strength up to 80% of IPM strength. But to truly make a statement about the missing spectroscopic strength, one would need to disentangle the contributions to the ^{9}Be(^{36}Ca,^{33}Ar)X cross section from processes other than neutron knockout to continuum states in ^{35}Ca followed by evaporation of 2 protons. One must, however, consider this process to be far more likely than the direct knockout of three valence nucleons.

3.5 Discussion

The cross section for knockout of the deeply-bound neutron in ^{36}Ca is much smaller than the sp cross sections calculated with either the eikonal theory or the transfer-to-continuum

theory. The deduced spectroscopic factor is therefore very small, but it is consistent with the systematics inferred from previous knockout analyses. A search was made for the missing spectroscopic strength in the excited states of ^{35}Ca, but from our experiment we can not determine how much of the cross section observed to ^{33}Ar came from *s*-wave strength in ^{35}Ca.

If the knockout analysis does underestimate spectroscopic strength, a natural place to look for the source of the discrepancy with DOM and transfer results is the reaction theory used to describe the knockout process and obtain single-particle cross-sections. One possibility is that the beam energies used are not high enough for the requisite approximations to be valid, so it may prove useful to attempt these reactions at higher beam energies, for example at the RIKEN facility, where beam energies of 200-300 MeV/A can be achieved.

Another possibility is that the interaction between the residue+nucleon and the target nucleus is not accurately modeled due to the complexity of using a hadronic target. In this case, switching to a simpler probe may allow greater confidence in the theoretical description of the interaction. Instead of ^{9}Be, one could use a hydrogen target, where the reaction theory is on more stable footing and the interaction is better understood. There is such a target planned at the NSCL, however, it will be very thick, so a higher beam energy would likely be needed.

There is also the possibility that the $-n,-2p$ strength does belong to *s*-wave n removal, followed by evaporation. If this were true, it would suggest that the SM and DOM calculations miss strength that is near the ground state, but in the continuum. It would be difficult to investigate this possibility using the knockout reaction studied here, since the

^{35}Ca residue proton decays to a nuclide which itself proton decays before reaching our detectors. It would be advantageous to instead study the knockout of a deeply bound neutron from a nucleus in which the $-n,-p$ residue is bound to proton emission. Then one could detect both the proton and the $-n,-p$ residue, and reconstruct not only the cross section but also the l-wave character of the strength in the continuum excited states of the neutron-knockout residue.

Chapter 4

Summary

This work has presented two experiments which were undertaken to investigate how nuclear correlations change with n/p asymmetry - the measurement of neutron total cross section of ^{48}Ca from 15 to 300 MeV, and the hadron-induced single-nucleon knockout cross sections for ^{36}Ca. Since it is difficult to get large amounts of the rare isotope ^{48}Ca, a digital-signal-processing method was developed to measure the neutron total cross section. This technique resulted in data with high statistical accuracy using samples that were an order of magnitude smaller than those used with conventional (non-digital) techniques.

When incorporated into the updated DOM analysis described in Section 2.5, the relative difference between the measured neutron total cross sections of ^{48}Ca and ^{40}Ca is consistant with a surface imaginary potential for neutrons whose magnitude does not change much as the nuclei become more neutron-rich. Recall that it has been concluded from prior DOM analyses that the asymmetry dependence of this potential for protons leads to a modest dependence of the proton correlations (and thus spectroscopic factors) on asymmetry, which

is consistent with trends deduced from transfer reactions.

In contrast, for the hadron-induced knockout in ^{36}Ca, the small experimental knockout cross section measured for the deeply-bound valence neutron (as compared to an eikonal reaction theory) implies a very small spectroscopic factor and supports a strong trend in correlations with asymmetry. If the cross section for $-n-2p$ is s-wave, this would give confidence to the extracted SF for the deeply bound neutron, and would suggest that the SM calculations may be missing low-lying correlations (because they are in the continuum). This is the conclusion reached in recent work by P. Fallon [52].

Enhanced correlations for very asymmetric systems can be understood on the basis of proximity to the continuum. As the valence level of the weakly-bound nucleon approaches the continuum, it can mix strongly with continuum states due to the very small energy difference. The deeply-bound valence nucleon can couple to a particle-hole excitation of the weakly-bound nucleon, shifting spectroscopic strength to lower energies. Because the continuum is so close to the valence level, the spectroscopic strength remains close to the sp-level energy - close enough that the DOM may not be able to resolve the peak at the sp level from the nearby continuum strength. Standard SM calculations do not include continuum states and would miss correlations due to mixing with nearby continuum states.

Recent coupled-cluster calculations for protons in neutron-rich oxygen isotopes provide an indication that mixing with continuum states does indeed lead to a greater suppression of SFs [53]. For example, the SF for ^{28}O is around $S = 0.5$ when continuum states are considered, compared to $S = 0.7$ when they are not. For larger systems, the effect may be enhanced due to the higher density of states. Mixing with continuum states may be

suppressed, however, for cases in which the weakly-bound nucleon is a proton (due to the Coulomb barrier) or is not in an s state (due to the centrifugal barrier). Although the effect of continuum states does not fully explain the suppression of SF seen in hadron-induced knockout analyses, it is the only calculation which comes close to agreement with these experiments. These calculations do not tell the whole story, but they may be pointing the way to a solution to this puzzle.

On the other hand, if the observed $-n, -2p$ neutron strength (to ^{33}Ar) is not s-wave, then it would lead one to question the extracted SF for the deeply-bound neutron. Reasonable adjustments to the eikonal calculation inputs (bound-state wavefunctions, nuclear density profiles, etc.) did not have a significant effect on the magnitude of the cross sections. Thus, if the source of the discrepancy with DOM and transfer results is to be found in the knockout analysis, it is likely either a fundamental problem with the theoretical description of the deeply-bound nucleons or a problem with the applicability of the eikonal reaction model to hadron-induced knockout reactions at the energies of the present study (i.e. the intermediate energies available at the NSCL). For the latter possibility, the reaction model for knockout of strongly-bound nucleons needs to be tested by showing that the results are invariant with increasing beam energy and changing the target to a pure nucleon (i.e. H_2 target). Both of these experiments can be contemplated in the coming years at facilities currently being constructed.

Bibliography

[1] W. Dickhoff and D. Van Neck, *Many-body theory exposed!* (World Scientific New Jersey, 2005).

[2] C. Barbieri, AIP Conference Proceedings **791**, 57 (2005).

[3] C. Barbieri, Phys. Rev. Lett. **103**, 202502 (2009).

[4] R. Subedi, R. Shneor, P. Monaghan, B. Anderson, K. Aniol, J. Annand, J. Arrington, H. Benaoum, F. Benmokhtar, W. Boeglin, et al., Science **320**, 1476 (2008).

[5] H. Baghdasaryan, L. Weinstein, J. Laget, K. Adhikari, M. Aghasyan, M. Amarian, M. Anghinolfi, H. Avakian, J. Ball, M. Battaglieri, et al., Phys. Rev. Lett. **105**, 222501 (2010).

[6] A. Gade, P. Adrich, D. Bazin, M. Bowen, B. Brown, C. Campbell, J. Cook, T. Glasmacher, P. Hansen, K. Hosier, et al., Phys. Rev. C **77**, 44306 (2008).

[7] J. Lee, M. Tsang, D. Bazin, D. Coupland, V. Henzl, D. Henzlova, M. Kilburn, W. Lynch, A. Rogers, A. Sanetullaev, et al., Phys. Rev. Lett. **104**, 112701 (2010).

[8] F. Nunes, A. Deltuva, and J. Hong, Physical Review C **83**, 034610 (2011).

[9] C. Mahaux and R. Sartor, Adv. in Nucl. Phys. **20**, 1 (1991).

[10] J. Mueller, R. Charity, R. Shane, L. Sobotka, S. Waldecker, W. Dickhoff, A. Crowell, J. Esterline, B. Fallin, C. Howell, et al., in press, Phys. Rev. C.

[11] W. Varner, T. McAbee, E. Ludwig, and T. Clegg, Phys. Rep. **201**, 57 (1991).

[12] R. Charity, J. Mueller, L. Sobotka, and W. Dickhoff, Phys. Rev. C **76**, 44314 (2007).

[13] B. Buck, R. Maddison, and P. Hodgson, Philosophical Magazine **5**, 1181 (1960).

[14] F. Dietrich, J. Anderson, R. Bauer, S. Grimes, R. Finlay, W. Abfalterer, F. Bateman, R. Haight, G. Morgan, E. Bauge, et al., Phys. Rev. C **67**, 44606 (2003).

[15] R. Shane, R. Charity, J. Elson, L. Sobotka, M. Devlin, N. Fotiades, and J. O'Donnell, Nucl. Instr. and Meth. A **614**, 468 (2010).

[16] A. Gade, D. Bazin, B. Brown, C. Campbell, J. Church, D. Dinca, J. Enders, T. Glasmacher, P. Hansen, Z. Hu, et al., Phys. Rev. Lett. **93**, 42501 (2004).

[17] R. Charity, L. Sobotka, and W. Dickhoff, Phys. Rev. Lett. **97**, 162503 (2006).

[18] S. Grimes, J. Anderson, R. Bauer, and V. Madsen, Nucl. Sci. and Eng. **130**, 340 (1998).

[19] S. Grimes, J. Anderson, R. Bauer, and V. Madsen, Nucl. Sci. and Eng. **134**, 77 (2000).

[20] W. Abfalterer, F. Bateman, F. Dietrich, R. Finlay, R. Haight, and G. Morgan, Phys. Rev. C **63**, 44608 (2001).

[21] P. Lisowski, C. Bowman, G. Russell, and S. Wender, Nucl. Sci. and Eng **106**, 208 (1990).

[22] P. Lisowski and K. Schoenberg, Nucl. Instr. and Meth. A **562**, 910 (2006).

[23] *Acqiris Digitizers*, Agilent Technologies (http://agilent.com), brochure can be found at: http://cp.literature.agilent.com/litweb/pdf/5989-7470EN.pdf.

[24] M. Moore, Nucl. Instr. and Meth. **169**, 245 (1980).

[25] R. Finlay, W. Abfalterer, G. Fink, E. Montei, T. Adami, P. Lisowski, G. Morgan, and R. Haight, Phys. Rev. C **47**, 237 (1993).

[26] *Nuclear Radii for Some Isotopes Derived from Total Neutron Cross-Sections*, vol. 2 of *Proceedings of 4th All Union Conf. on Neutron Phys.* (1977).

[27] S. F. Hicks, S. E. Hicks, G. R. Shen, and M. T. McEllistrem, Phys. Rev. C **41**, 2560 (1990).

[28] R. Furnstahl and A. Schwenk, J. Phys. G **37**, 064005 (2010).

[29] A. M. Mukhamedzhanov and A. S. Kadyrov, Phys. Rev. C **82**, 051601 (2010).

[30] B. A. Brown, P. G. Hansen, B. M. Sherrill, and J. A. Tostevin, Phys. Rev. C **65**, 061601 (2002).

[31] J. Lee, M. Tsang, and W. Lynch, Phys. Rev. C **75**, 64320 (2007).

[32] D. Morrissey, B. Sherrill, M. Steiner, A. Stolz, and I. Wiedenhoever, Nucl. Instr. and Meth. B **204**, 90 (2003).

[33] D. Bazin, J. Caggiano, B. Sherrill, J. Yurkon, and A. Zeller, Nucl. Instr. and Meth. B **204**, 629 (2003).

[34] D. Weisshaar, A. Gade, T. Glasmacher, G. Grinyer, D. Bazin, P. Adrich, T. Baugher, J. Cook, C. Diget, S. McDaniel, et al., Nucl. Instr. and Meth. A **624**, 615 (2010).

[35] J. Yurkon, D. Bazin, W. Benenson, D. Morrissey, B. Sherrill, D. Swan, and R. Swanson, Nucl. Instr. and Meth. A **422**, 291 (1999).

[36] J. Tostevin, Nucl. Phys. A **682**, 320 (2001).

[37] C. Bertulani and A. Gade, Comp. Phys. Comm. **175**, 372 (2006).

[38] S. C. Pieper, K. Varga, and R. B. Wiringa, Phys. Rev. C **66**, 044310 (2002).

[39] A. Bonaccorso and G. F. Bertsch, Phys. Rev. C **63**, 044604 (2001).

[40] A. Bonaccorso and D. M. Brink, Phys. Rev. C **38**, 1776 (1988).

[41] F. Carstoiu, E. Sauvan, N. Orr, and A. Bonaccorso, Phys. Rev. C **70**, 54602 (2004).

[42] P. Hansen and J. Tostevin, Ann. Rev. of Nucl. and Part. Sci. **53**, 219 (2003).

[43] C. A. Bertulani and P. Danielewicz, *Introduction to Nuclear Reactions*, Graduate Student Series in Physics (IOP Publishing, 2004).

[44] W. H. Dickhoff, D. Van Neck, S. J. Waldecker, R. J. Charity, and L. G. Sobotka, Phys. Rev. C **82**, 054306 (2010).

[45] C. Louchart, A. Obertelli, A. Boudard, and F. Flavigny, Phys. Rev. C **83**, 011601 (2011).

[46] *Evaluated nuclear structure data file*, URL `http://www.nndc.bnl.gov/ensdf/`.

[47] R. Reynolds, P. Cottle, A. Gade, D. Bazin, C. Campbell, J. Cook, T. Glasmacher, P. Hansen, T. Hoagland, K. Kemper, et al., Phys. Rev. C **81**, 67303 (2010).

[48] C. Jeanperrin, L. Rosier, B. Ramstein, and E. Obiajunwa, Nucl. Phys. A **503**, 77 (1989).

[49] B. Brown and W. Richter, in *Journal of Physics: Conference Series* (IOP Publishing, 2005), vol. 20, p. 145.

[50] A. Gade, D. Bazin, B. Brown, C. Campbell, J. Church, D. Dinca, J. Enders, T. Glasmacher, P. Hansen, Z. Hu, et al., Phys. Rev. C **69**, 34311 (2004).

[51] R. J. Charity, Phys. Rev. C **82**, 014610 (2010).

[52] P. Fallon, E. Rodriguez-Vieitez, A. Macchiavelli, A. Gade, J. Tostevin, P. Adrich, D. Bazin, M. Bowen, C. Campbell, R. Clark, et al., Phys. Rev. C **81**, 041302 (2010).

[53] Ø. Jensen, G. Hagen, M. Hjorth-Jensen, B. Brown, and A. Gade, Arxiv preprint arXiv:1104.1552 (2011).